COUPLING IMPEDANCE AND SINGLE BEAM COLLECTIVE EFFECTS FOR THE FUTURE CIRCULAR COLLIDER (LEPTON OPTION)

Eleonora Belli

SAPIENZA
UNIVERSITÀ DI ROMA

Dipartimento di Fisica
Ph.D. School on Accelerator Physics, Cicle XXXI
Supervisor: Prof. Mauro Migliorati

CERN

European Organization for Nuclear Research, Geneva, Switzerland
Beams Department, Accelerators and Beam Physics Group
Supervisor: Dr. Giovanni Rumolo

This project was supported in part by the European Commission Horizon 2020 Research and Innovation programme under Grant Agreement No. 730871.

Ai miei genitori e ai miei nonni

CONTENTS

1 INTRODUCTION 19

2 THE FUTURE CIRCULAR LEPTON COLLIDER 23
- 2.1 Accelerator physics and design 24
- 2.2 Machine layout and beam parameters 26

3 COLLECTIVE EFFECTS IN PARTICLE ACCELERATORS 31
- 3.1 Wakefields and impedances 32
  - 3.1.1 Wake functions and coupling impedances 33
  - 3.1.2 Wake potentials and loss factors 36
  - 3.1.3 Wakefield and impedance of a resonator 39
- 3.2 Electron cloud 41
  - 3.2.1 Primary electron production 42
  - 3.2.2 Secondary electron emission 44
  - 3.2.3 Electron cloud build up regimes 46

4 ELECTRON CLOUD STUDIES 47
- 4.1 The PyECLOUD code 47
- 4.2 PyPIC: the multigrid solver 49
  - 4.2.1 Dualgrid implementation 49
  - 4.2.2 Multigrid implementation 53
- 4.3 Simulation studies for the FCC-ee arc components 59
- 4.4 Photoemission due to synchrotron radiation 69
- 4.5 Simulation studies for the FCC-ee IR components 69
- 4.6 Electron density threshold for transverse instability 72

5 RESISTIVE WALL WAKEFIELDS AND IMPEDANCES 75
- 5.1 The importance of the resistive wall impedance in FCC-ee . . 77
- 5.2 Resistive wall impedance with coating 80
- 5.3 Single bunch dynamics 84
  - 5.3.1 Longitudinal dynamics 87

5.3.2 Transverse dynamics 93
5.4 Multi bunch dynamics 95
5.4.1 Transverse dynamics 95
5.4.2 Longitudinal dynamics 97

6 ACTIVATION OF NEG THIN FILMS AND SEY MEASUREMENTS 99
6.1 Non-evaporable getters 100
6.2 Sample preparation 100
6.3 Sample characterization 106
6.3.1 XPS analysis 106
6.3.2 Depth profile 110
6.3.3 SEY measurements 111
6.4 Impact of SEY measurements on EC build up simulations . . 114

7 THE FCC-EE LONGITUDINAL IMPEDANCE MODEL 117
7.1 Other impedance sources 117
7.1.1 RF cavities and tapers 117
7.1.2 Synchrotron radiation absorbers 120
7.1.3 Collimators 122
7.1.4 Beam Position Monitors 123
7.1.5 RF shielding 125
7.2 Longitudinal impedance budget 126

8 IMPEDANCE STUDIES IN THE INTERACTION REGION 131
8.1 IP resistive wall impedance 132
8.2 SR masks 133
8.3 An unavoidable trapped mode 134
8.3.1 Wave excitation in the IR 135
8.3.2 Structure of the unavoidable trapped mode in the IR . 137
8.3.3 HOM analysis 137
8.3.4 HOM absorber concept 140

9 CONCLUSIONS 143

Bibliography 147

Acknowledgements 161

LIST OF FIGURES

Figure 2.1 Schematic view of the FCC tunnel in the Geneva area. 24

Figure 2.2 Expected baseline luminosities of the current worldwide lepton colliders as a function of the centre-of-mass energy. The variable s on x-axis is the Mandelstam variable and $\sqrt{s}$ represents the total centre-of-mass energy during collision. 25

Figure 2.3 Preliminary schedule of the FCC-ee operation. 26

Figure 2.4 The FCC-hh (left side) and FCC-ee (right side) layouts. 26

Figure 2.5 Schematic layout of the pre-injector chain (left side) and the injector complex (right side). 27

Figure 3.1 Reference system with a source particle q_1 (in red) and a test particle q_2 (in green). 32

Figure 3.2 Example of longitudinal (top) and transverse (bottom) wake functions for ultrarelativistic particles ($\beta = 1$). 35

Figure 3.3 Convolution integral to compute the energy loss of a slice due to the entire bunch. 36

Figure 3.4 Scheme of a parallel RLC circuit representing a resonant mode. 39

Figure 3.5 Sketch of the formation of an electron cloud in a section of the machine. 42

Figure 3.6 SEY curve as a function of the primary electrons energy. 44

Figure 3.7 SEY curve: elastic component δ_{elas}, true secondary component δ_{true} and total δ_E. 45

Figure 3.8 Time evolution of the total number of electrons in the chamber of the FCC-ee arc dipoles for δ_{max} = 1.6. 46

Figure 4.1 PyECLOUD main loop for EC build up simulations. 48

Figure 4.2 Dualgrid implementation. On the left side: an internal grid (in red) is placed around the beam (in green), in addition to the main grid (in blue) defined over the entire chamber. On the right side: the resolution of the new grid is finer compared to the main grid. . 50
Figure 4.3 Distances and grid nodes used in the scatter routine for the computation of the space charge field. 50
Figure 4.4 Horizontal component of the electric field computed at probe r = 7 mm (yellow line on the left plot) which crosses the edges of the internal grid. The artifact can be minimized by discarding the most external cells of the internal grid during interpolation. 52
Figure 4.5 Horizontal (left) and vertical (right) components of the electric field computed at a probe r = 20 mm by using analytical, singlegrid and dualgrid methods. . . 53
Figure 4.6 Horizontal (left) and vertical (right) components of the electric field computed at a probe r = 2 mm by using analytical, singlegrid and dualgrid methods. . 53
Figure 4.7 Multiple nested grid configuration implemented in the multigrid solver. 54
Figure 4.8 Multigrid configuration (top), horizontal and vertical components of the electric field (bottom) computed at a probe 1σ by using analytical Bassetti-Erskine formula, singlegrid and multigrid methods. 56
Figure 4.9 RMS error w.r.t. the analytical Bassetti-Erskine formula on the computation of the electric field as a function of the distance from the bunch center. 56
Figure 4.10 Scattering time and solving time required in simulation by using singlegrid and multigrid methods. . . . 57
Figure 4.11 Multigrid configuration (top), electric field components (centre) and RMS error of all internal grids with different resolutions compared with the analytic one obtained by using the Bassetti-Erskine formula. . . . 58
Figure 4.12 Beta functions and dispersion functions along the cells of the FCC-ee arc FODO lattice. 59

Figure 4.13 Transverse profile of the FCC-ee vacuum chamber. . . 60
Figure 4.14 Heat load in the FCC-ee arc dipoles as a function of the SEY parameter. 61
Figure 4.15 Evolution of the total number of electrons in the beam chamber of the FCC-ee arc dipoles as a function of time, for 2.5 ns (a), 5 ns (b) and 15 ns (c) bunch spacings. 62
Figure 4.16 Energy spectrum of the electrons impacting the wall in a FCC-ee arc dipole magnet. 63
Figure 4.17 Different snapshots of the electron distribution in the FCC-ee arc dipoles during the passage of two consecutive bunches, at saturation level. The simulation is performed at low energy, with 15 ns bunch spacing, for SEY = 1.3. 64
Figure 4.18 Heat load in the FCC-ee arc quadrupoles (left side) and drifts (right side) as a function of the SEY parameter. 65
Figure 4.19 Evolution of the total number of electrons in the beam chamber of the FCC-ee arc quadrupoles (top) and drifts (bottom) as a function of time, for 15 ns bunch spacing. 65
Figure 4.20 Different snapshots of the electron distribution in the FCC-ee arc quadrupoles during the passage of two consecutive bunches, at saturation level. The simulation is performed at low energy, with 15 ns bunch spacing, for SEY = 1.3. 67
Figure 4.21 Different snapshots of the electron distribution in the FCC-ee arc drifts during the passage of two consecutive bunches, at saturation level. The simulation is performed at low energy, with 15 ns bunch spacing, for SEY = 1.3. 68
Figure 4.22 Heat load as a function of SEY for arc dipoles, quadrupoles and drifts in case of no photoelectrons and different values of photoelectrons and reflectivity, for a bunch spacing of 15 ns. 70

Figure 4.23 Beta functions and dispersion functions around the IP. 71

Figure 4.24 Heat load in the FCC-ee IR quadrupoles as a function of the SEY parameter for 2.5 ns (a), 5 ns (b) and 15 ns (c) bunch spacings. 72

Figure 4.25 Schematic of the EC induced single bunch instability. 73

Figure 5.1 Skin depth as a function of frequency for copper. . . . 75

Figure 5.2 Yokoya form factors as a function of the major (a) and minor (b) semi-axes. 79

Figure 5.3 Ratio between the analytic impedances given by Eqs. 82 and 83 and the corresponding impedances obtained from ImpedanceWake2D, in the longitudinal (left side) and transverse (right side) planes. The red and blue curves represent the real part and the imaginary part of the impedance, respectively. 82

Figure 5.4 Ratio between the impedances of a two-layer beam pipe with a coating of 100 nm thickness and conductivities 10^6 S/m and 10^4 S/m, as given by ImpedanceWake2D, in the longitudinal (left side) and transverse (right side) planes. The red and blue curves represent the real part and the imaginary part of the impedance, respectively. 84

Figure 5.5 Model of the vacuum chamber used for simulations. 85

Figure 5.6 Real and imaginary part of transverse (top) and longitudinal (bottom) RW impedances as a function of the frequency for a copper pipe with 35 mm radius in the case of no coating and with NEG coating at different thicknesses. 86

Figure 5.7 Comparison of the analytic longitudinal wake potentials of a 3.5 mm Gaussian bunch with the wake potentials obtained from PyHEADTAIL as convolution between the longitudinal bunch distribution and the wake potential of a 0.35 mm Gaussian bunch in the case of no coating, with a copper pipe of 35 mm radius, and with NEG coating at different thicknesses. 88

Figure 5.8 RMS energy spread as a function of the bunch population given by numerical simulations considering only the RW impedance in the case of no coating, with a copper pipe of 35 mm radius, and with NEG films at different thicknesses. The dashed black line correspond to the nominal bunch population. 88

Figure 5.9 Microwave instability threshold as a function of the coating conductivity for all the thicknesses under study. The black dashed line corresponds to the nominal bunch intensity. 89

Figure 5.10 RMS bunch length as a function of the bunch population given by numerical simulations considering only the RW impedance in the case of no coating, with a copper pipe of 35 mm radius, and with NEG films at different thicknesses. The dashed black line correspond to the nominal bunch population. 90

Figure 5.11 Longitudinal bunch distribution obtained from Haissinski equation at nominal intensity in the case of no coating, with a copper pipe of 35 mm radius, and with NEG films at different thicknesses. The dashed black line represents the Gaussian equilibrium shape. 91

Figure 5.12 Loss factor as a function of the bunch length obtained from numerical simulations in the case of 100 nm thick films with different conductivities. 92

Figure 5.13 Incoherent synchrotron tune distribution at nominal intensity, produced by the RW impedance with a coating of 100 nm thickness. The results are obtained with PyHEADTAIL by using the machine parameters of Table 1 at Z resonance. 93

Figure 5.14 Real part of the tune shift of the first coherent oscillation modes as a function of the bunch population for 100 nm (top) and 1000 nm (bottom) thicknesses of NEG coating. The curves are obtained with DELPHI code by using the machine parameters of Table 1 at Z resonance and the bunch length given by PyHEADTAIL at different intensities. The dashed lines represent the nominal bunch population. 94
Figure 5.15 Vertical coupled bunch spectrum obtained by using the machine parameters of Table 1 at Z resonance and real part of the resistive wall impedance for a copper beam pipe of 35 mm without coating, as a function of frequency around f = 0. 96
Figure 5.16 Growth rate of the coupled bunch modes with azimuthal mode number $m = 0$. 97
Figure 5.17 Maximum shunt impedance of a HOM as a function of its resonance frequency, producing a growth rate which is compensated by the natural radiation damping. 98
Figure 6.1 NEG activation: the dissolution process of the oxide into the bulk is obtained by heating in vacuum. 100
Figure 6.2 Magnetron sputtering system. 101
Figure 6.3 Magnetron sputtering working principle. 101
Figure 6.4 The blue light is produced by the plasma when sputtering TiZrV cathode. 102
Figure 6.5 SEM analysis system (left side) and edge effect (right side). 103
Figure 6.6 SEM images of NEG thin films on copper substrate. 104
Figure 6.7 Morphology of NEG thin films analyzed by SEM. . . 105
Figure 6.8 Schematic view of a XPS system, consisting of a X-ray source, an electron energy analyzer and a ultra high vacuum environment. 106
Figure 6.9 Activation performance: reduction of the area of the oxygen peak from the XPS spectrum after the fourth activation cycle. 107

Figure 6.10 C1s peak area as a function of the activation temperature after the fourth activation cycle. 108

Figure 6.11 Ti2p (top), Zr3d (centre) and V2p (bottom) photopeaks obtained by XPS analysis for all the thicknesses under study. 2p and 3d refer to subshells of electronic configuration. 109

Figure 6.12 Profile of C, O, Ti, V, Zr and Cu as a function of depth for all the samples. 110

Figure 6.13 Experimental setup for SEY measurements. 111

Figure 6.14 SEY as a function of the primary electron energy for all the samples under study after the fourth activation cycle of 4 hours up to a temperature of 250°C. . . 113

Figure 6.15 Oxygen reduction and maximum SEY as a function of the coating thickness for all the samples under study after the fourth activation cycle of 4 hours up to a temperature of 250°C. 113

Figure 6.16 SEY as a function of the primary electron energy for the thin films after the fourth activation cycle of 24 hours up to a temperature of 250°C. 114

Figure 6.17 Oxygen reduction and maximum SEY as a function of the coating thickness for the thin films after the fourth activation cycle of 24 hours up to a temperature of 250°C. 114

Figure 6.18 Analytic curve for δ_{max} = 1.16 and LHC chamber parameters (blue), measured curve of the 87 nm film with δ_{max} = 1.16 and fit curve obtained by modified free parameters. 115

Figure 6.19 Heat load at SEY = 1.16 for all the machine components compared with previous results, in the case of 15 ns beam. 115

Figure 7.1 400 MHz single cell cavity used in ABCI. 117

Figure 7.2 Left side: wake potential of a cavity for σ_z=3.5 mm given by the ABCI code and by Eq. 93. Right side: total wake potential due to RF cavities compared to the RW wake potential of 100 nm NEG coating for σ_z=3.5 mm. 118
Figure 7.3 Sketch, not in scale, of a group of 4 cells with tapers. 119
Figure 7.4 Longitudinal loss factor as a function of the taper length obtained from ABCI code (green dots) and analytically (red dots). 119
Figure 7.5 Tapers used in ABCI. 120
Figure 7.6 Wake potential of a double taper for σ_z=3.5 mm given by the ABCI code (left side) and total wake potential due to tapers compared to the RW wake potential of 100 nm NEG coating for σ_z=3.5 mm (right side). . . . 120
Figure 7.7 Elliptic vacuum chamber with one absorber insertion. 121
Figure 7.8 Longitudinal wake potential of a 4 mm Gaussian bunch produced by 9228 absorbers with elliptic chamber and 10000 absorbers with the new design. 121
Figure 7.9 3D model of the FCC-ee chamber and a SR absorber with pumping slots used for CST simulations. 122
Figure 7.10 CST perspective view of the vertical collimator (left side) and top view of the horizontal one (right side). . 123
Figure 7.11 Wake potential of horizontal and vertical collimators given by CST (left side) and total wake potential due to collimators compared to the RW wake potential of 100 nm NEG coating (right side), for σ_z=3.5 mm. . . 123
Figure 7.12 CST perspective view of the four-button BPM (left side) and CST model of the winglet-to-circular taper for BPM installation(right side). 124
Figure 7.13 Wake potential of a BPM obtained from the CST code (left side) and total wake potential due to BPMs compared to the RW contribution of 100 nm NEG coating (right side), for σ_z=3.5 mm. 124

Figure 7.14 Longitudinal wake potential due to 4000 special tapers compared to the RW wake potential of 100 nm NEG coating (right side), for σ_z=3.5 mm. 125

Figure 7.15 Conventional finger-type RF shielding (left side) and inside view of the new comb-type bellows with small fingers between the teeth (right side). 125

Figure 7.16 Wake potential of conventional finger-type RF shielding (in red) and new comb-type bellows (in orange) compared to the RW one (in blue) for 3.5 mm RMS bunch length obtained from the CST code. 126

Figure 7.17 Longitudinal wake potentials for a Gaussian bunch with nominal bunch length $\sigma_z = 3.5mm$ due to the main FCC-ee components compared with the RW contribution (blue line). 127

Figure 7.18 Comparison of the longitudinal wake potentials of a 3.5 mm Gaussian bunch obtained from Impedance-Wake2D, ABCI and CST codes with the wake potentials obtained from PyHEADTAIL as convolution between the longitudinal bunch distribution and the wake potential of a 0.35 mm Gaussian bunch for each component. 128

Figure 7.19 RMS bunch length as a function of the bunch population with (orange curve) and without (blue curve) beamstrahlung, given by numerical simulations by considering the impedance contribution of all the machine components. 129

Figure 7.20 RMS energy spread as a function of the bunch population with (orange curve) and without (blue curve) beamstrahlung, given by numerical simulations by considering the impedance contribution of all the machine components. 129

Figure 8.1 Layout of the IR (expanded horizontal scale). 131

Figure 8.2 Longitudinal RW impedance for copper and beryllium. 132

Figure 8.3 SR masks in QC1 quadrupole (left side) and QC2 quadrupole (right side) used for ABCI simulations. . 133
Figure 8.4 Wake potential of a $\sigma_z = 3.5$ mm bunch given by SR masks obtained from the ABCI code. 134
Figure 8.5 Electric force field line distribution at the time when a relatively short bunch has just passed a pipe connection. The red line shows the bunch line charge density distribution and the bunch trajectory. 136
Figure 8.6 Electromagnetic field line distribution at the time when a short bunch has passed the outgoing pipe connection. Green and blue lines represent force lines with opposite directions. The red line shows the bunch line charge density distribution and the bunch trajectory. 136
Figure 8.7 Electric field line distribution of the trapped mode. The red arrows show the direction of the colliding beams. 137
Figure 8.8 Geometry of the IR model 1. 138
Figure 8.9 Wake potential of a 2.5 mm bunch and spectrum of the excited field in the IR model 1. 138
Figure 8.10 Electric field line distribution for the trapped mode in Model 1. 139
Figure 8.11 Geometry of the IR Model 2 and spectrum of the excited fields. 139
Figure 8.12 Inside and outside view of the transition in the IR model 3. 140
Figure 8.13 Wake potential of a 2.5 mm bunch and spectrum of the excited field in the IR model 3. 140
Figure 8.14 Electric field line distribution for the trapped mode in Model 3. 141
Figure 8.15 IR smooth geometry with HOM absorbers. 141

LIST OF TABLES

Table 1 Machine parameters of FCC-ee for different energies, where SR and BS stand for synchrotron radiation and beamstrahlung. 29
Table 2 Arc magnet parameters used for build up simulations at 45.6 GeV. 60
Table 3 Threshold SEY for multipacting for all the arc components. 66
Table 4 IR Magnet parameters used for build up simulations at 45.6 GeV. 71
Table 5 Threshold SEY for multipacting for all the IR components. 72
Table 6 Metallic surface composition in at.% determined in the as received state at the first and fourth activation cycles. 108
Table 7 Power loss contribution of the main FCC-ee components at nominal intensity and bunch length, in the lowest energy case of 45.6 GeV. 127

1

INTRODUCTION

The figure of merit of the performance of a particle collider is the luminosity, which is proportional to the number of events per second generated in the collisions. When studying rare events as in the Large Hadron Collider (LHC) at CERN, the higher the luminosity, the more likely rare processes can occur and be observed. The High-Luminosity LHC (HL-LHC) project, an upgrade of LHC delivering proton-proton collisions at centre-of-mass energy of 14 TeV, aims to increase the luminosity by a factor of 10 beyond the LHC design value. This machine will allow finding answers to the several open questions about the Standard Model theory. While HL-LHC is expected to run for the next 20 years, CERN launched the Future Circular Collider (FCC) study for the design of different circular colliders for the post-LHC era. This study is investigating a high energy proton-proton machine (FCC-hh) to reach a centre-of-mass energy of 100 TeV and a high luminosity electron-positron collider (FCC-ee) as a potential first step to cover a beam energy range from 45.6 GeV to 182.5 GeV, thus allowing to study the properties of the Higgs, W and Z bosons and top quark pair production thresholds with unprecedented precision.

The configuration and beam parameters of the lepton collider will be presented in detail in Chapter 2. Chapter 3 describes the theoretical framework needed to understand the core of this research activity, dedicated to the study of the main limitations of FCC-ee on the Z resonance. At high beam intensity, necessary to reach the high luminosity foreseen for FCC-ee, electron cloud (EC) and collective effects due to the electromagnetic fields generated by the interaction of the beam with the vacuum chamber represent a serious issue by producing instabilities that can limit the machine operation and performance.

The first part of this thesis is focused on EC studies. Despite the fact that FCC-ee does not operate at cryogenic temperatures, a critical aspect for the operation at nominal current is the heating of the pipe walls caused by the interaction of the EC with the vacuum chamber. Besides this local effect, the EC can also interact with the beam, inducing transverse instabilities that can lead to emittance blow-up, tune shift and spread and beam losses. Additional tools have been developed in the PyECLOUD code to extend its validity range and to make it suitable for FCC-ee. A multigrid solver have been implemented in the PyPIC library of PyECLOUD to refine the resolution around the beam location, thus improving the accuracy and the computational time of the simulation code. This new implementation allowed the estimation of the multipacting thresholds for the EC build up and an evaluation of the heat load in the main components of the positron ring. All these studies, presented in Chapter 4, revealed the necessity of minimizing the Secondary Electron Yield (SEY) of the pipe walls by applying a TiZrV Non-Evaporable Getter (NEG) coating in the entire ring. The presence of this coating affects the resistive wall (RW) impedance, representing the major source of wakefields in the machine due to its large circumference. Nowadays, modern accelerators as the LHC use NEG layers of about 1 μm thickness to ensure the required pressure and low background and to mitigate the EC multipacting. However, beam dynamics studies for FCC-ee at 45.6 GeV pointed out that this standard thickness makes the contribution of the RW to the machine impedance budget very critical. The studies presented in Chapter 5 will show that minimising the thickness of the coating is mandatory to reduce the RW contribution, thus increasing the single bunch instability thresholds at low energy.

However, reducing the thickness of NEG coatings can affect the performance of the material itself and therefore the maximum SEY and related electron cloud mitigation. In fact, every time vacuum chambers are exposed to air, NEG coatings need to be activated to act as pumps, i.e. heated in vacuum so that the oxide layer grown on the surface can be diffused into the bulk. Considering that the quantity of oxygen that can be dissolved in the film is limited, thinner films could not activate properly. For this reason, an extensive measurement campaign was performed at CERN to characterize TiZrV thin films with thicknesses below 250 nm. Chapter 6 presents the coating process, the activation performance investigated by surface analysis as well as the SEY of the thin NEG coatings. The final goal of this experimental activity was to find the minimum effective thickness satisfying impedance, vacuum and electron cloud requirements.

Besides the RW, other impedance sources have been analyzed and opti-

mized in terms of electromagnetic impact. The impedance model thus obtained has been used to study single bunch instabilities, to predict their effects on beam dynamics and to identify possible mitigation techniques. The contributions of all these components to the total impedance budget and their effects on the stability of the beam are presented in Chapter 7.
Chapter 8 presents the impedance studies in the interaction region (IR) of FCC-ee. In order to find an optimal IR geometry, three different beam pipe models were proposed and CST simulations in time domain were performed for each model to find the resonances in the spectrum of the wake potential. These studies led to the identification of a trapped mode that seems to be unavoidable even in a very smooth geometry. By analyzing the structure of this mode, whose presence has been confirmed with CST simulations in the frequency domain, longitudinal slots and a water-cooled absorber were designed and included in the IR model to reduce the power loss and to prevent vacuum degradation. Geometrical and resistive wall impedances generated by the synchrotron radiation (SR) masks and the coatings of the pipe walls, respectively, were also analyzed in the IR, giving an estimation of the corresponding power losses.

2

THE FUTURE CIRCULAR LEPTON COLLIDER

On 4th July 2012, the two Large Hadron Collider (LHC) [1] experiments ATLAS and CMS announced the observation of a new particle in the centre-of-mass energy near 125 GeV [2, 3] consistent with the Higgs boson predicted by the Standard Model. Although this discovery validated experimentally the Standard Model, the theory is still incomplete with several open questions concerning dark matter, neutrino masses, weakness of gravity, etc.

The High Luminosity LHC (HL-LHC) project [4, 5], an upgrade of LHC delivering proton-proton collisions at centre-of-mass energy of 14 TeV, aims to increase the total number of collisions by a factor of 10 compared to the LHC baseline programme. It is expected to run for the next 20 years and will help to find some new answers. However, it might not be enough.

For this reason, in 2013 the European Strategy for Particle Physics requested CERN to *"undertake design studies for accelerator projects in a global context with emphasis on proton-proton and electron-positron high-energy frontier machines ... [which] should be coupled to a vigorous accelerator R&D programme, including high-field magnets and high-gradient accelerating structures, in collaboration with national institutes, laboratories and universities worldwide"* in order to *"propose an ambitious post-LHC accelerator project ... by the time of the next Strategy update"* around 2019.

On the basis of this request, CERN launched in 2014 the Future Circular Collider (FCC) Study [6, 7] aiming to design different particle accelerators to ensure a worldwide particle physics programme after LHC. Nowadays, more than 120 institutes are part of this international collaboration whose ultimate goal is a hadron collider (FCC-hh) with a centre-of-mass energy of 100 TeV, an order of magnitude above the LHC. This machine will define a new 100 km infrastructure for the FCC accelerator complex in the Geneva area (see Fig. 2.1 [8]) and will be based on 16 T magnets with a peak luminosity of $5 \cdot 10^{34}\, cm^{-2} s^{-1}$. Possible first steps towards this high

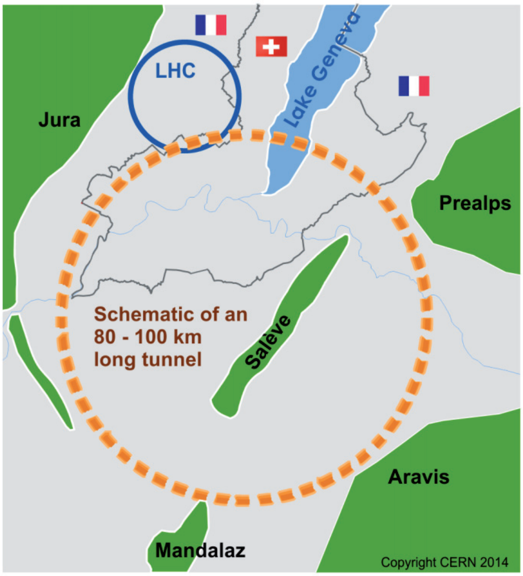

Figure 2.1: Schematic view of the FCC tunnel in the Geneva area.

energy hadron collider are the high luminosity electron-positron collider FCC-ee (formerly TLEP) that will allow very precise measurements of the Standard Model and the 27 TeV proton-proton collider High Energy LHC (HE-LHC) which is an upgrade of LHC with the FCC-hh technology in the same LHC tunnel. An electron-proton machine (FCC-he) is also considered as a possible scenario.
All the basic requirements for these colliders have been summarised in the Conceptual Design Report [9] that has been published at the end of 2018. The studies presented in this thesis focus on the lepton collider FCC-ee whose configuration and beam parameters will be described in this chapter.

2.1 ACCELERATOR PHYSICS AND DESIGN

The possibility to explore a 120 GeV lepton collider in the LHC tunnel was already considered before the discovery of the Higgs boson, to perform precise measurements of this elementary particle [10]. This option evolved then in the high luminosity electron-positron circular collider FCC-ee, following the requirements of the 2013 European Strategy statement: *"There*

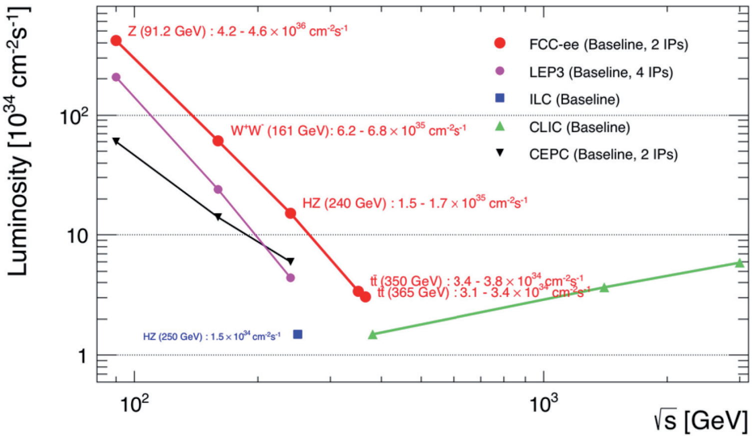

Figure 2.2: Expected baseline luminosities of the current worldwide lepton colliders as a function of the centre-of-mass energy. The variable s on x-axis is the Mandelstam variable and $\sqrt{s}$ represents the total centre-of-mass energy during collision.

is a strong scientific case for an electron-positron collider, complementary to the LHC, that can study the properties of the Higgs boson and other particles, with unprecedented precision and whose energy can be upgraded."

Within the FCC studies, FCC-ee is considered as a potential first step towards the 100 TeV hadron collider FCC-hh in the same 97.75 km tunnel. The lepton collider is being designed to cover a beam energy range from 45.6 GeV to 182.5 GeV, thus allowing to study the properties of the Higgs, W and Z bosons and top quark pair production thresholds with unprecedented precision. Nowadays, other e^+e^- colliders as ILC [11, 12], CLIC [13, 14], LEP3 [15] and CEPC [16] are considered to study the properties of the Higgs boson and the other particles. Among all these proposed machines, FCC-ee is expected to deliver the highest luminosity at each centre-of-mass energy, as shown in Fig. 2.2, thus allowing very precise measurements of all known heavy particles. Figure 2.3 shows the FCC-ee operation model, for a total duration of 14 years. The phase 1 lasts 8 years and covers Z, W and H measurements. The Z pole will operate at half design luminosity over the first two years. A one year shutdown will follow the phase 1, for RF installations, and finally there will be 5 years of tt running.

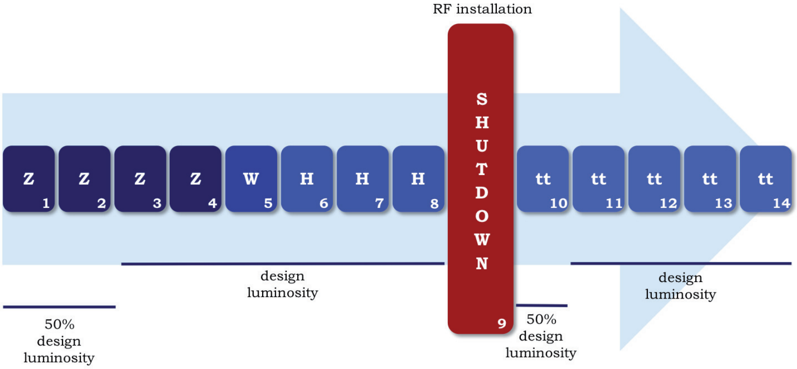
RF installation
SHUTDOWN
Z 1
Z 2
Z 3
Z 4
W 5
H 6
H 7
H 8
9
tt 10
tt 11
tt 12
tt 13
tt 14
50% design luminosity
design luminosity
50% design luminosity
design luminosity

Figure 2.3: Preliminary schedule of the FCC-ee operation.

2.2 MACHINE LAYOUT AND BEAM PARAMETERS

The layout of the machine is described in [17] and shown in Fig. 2.4. It follows the one of the hadron collider, with two interaction points (IPs) located at the straight sections A (close to CERN) and G (on the opposite side). The very high luminosity at each energy is due to some key features in the design of the machine. First of all, the maximum acceptable SR power per beam is fixed to be 50 MW at all energies and this value defines the total beam current of each experiment. Since the SR power is proportional to $E^4 I$, where E is the beam energy and I is the beam current, at low

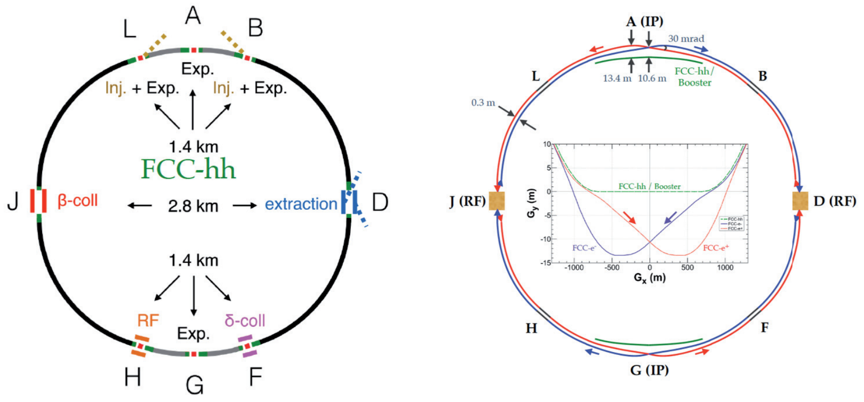
A
B
L
Exp.
Inj. + Exp.
Inj. + Exp.
1.4 km
FCC-hh
J
β-coll
2.8 km
extraction
D
1.4 km
RF
δ-coll
Exp.
H
G
F
A (IP)
30 mrad
13.4 m
10.6 m
FCC-hh/ Booster
L
B
0.3 m
J (RF)
D (RF)
G_y (m)
G_x (m)
FCC-hh / Booster
FCC-e⁻
FCC-e⁺
FCC-hh
FCC-e-
FCC-e+
10
5
0
-5
-10
-15
-1000
-500
0
500
1000
H
F
G (IP)

Figure 2.4: The FCC-hh (left side) and FCC-ee (right side) layouts.

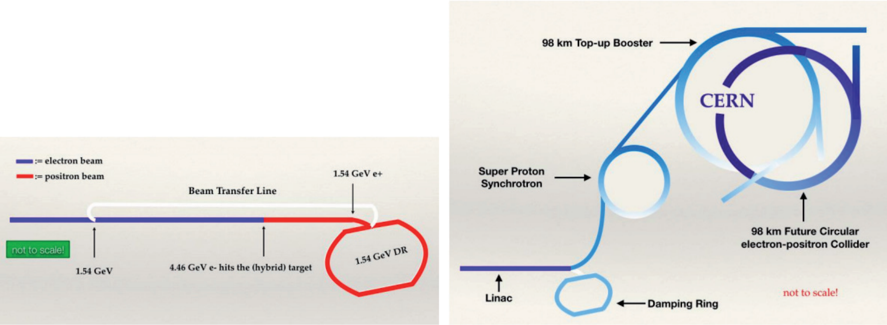
:= electron beam
:= positron beam
Beam Transfer Line
1.54 GeV e+
not to scale!
1.54 GeV
4.46 GeV e- hits the (hybrid) target
1.54 GeV DR
98 km Top-up Booster
CERN
Super Proton Synchrotron
98 km Future Circular electron-positron Collider
Linac
Damping Ring
not to scale!

Figure 2.5: Schematic layout of the pre-injector chain (left side) and the injector complex (right side).

energy a higher current can be injected, thus maximising the luminosity. The two separate beam pipes for the two counter-rotating electron and positron beams are important for two main aspects: at low energy they allow avoiding parasitic collisions and therefore an operation with a large number of bunches, while at the highest energy the double ring allows the tapering of the magnets to compensate the energy sawtooth effect [17]. A crab-waist scheme [18] with a large horizontal crossing angle of 30 mrad is foreseen at IP to optimize the colliding area and to further maximise the luminosity. Moreover, considering that beamstrahlung (BS) is one of the main luminosity limitations in the machine, a larger energy acceptance has been defined to hold all those particles that are losing energy due to BS and are falling outside the momentum acceptance. As illustrated in the next chapters, the effect of BS of increasing the equilibrium energy spread and bunch length will help to overcome single bunch instabilities at low energy. In order to mantain the stored beam current and the highest luminosity, the initial FCC-ee injection scheme was based on CLIC concepts [19]. However, for the final design a SuperKEKB approach using short bunches with high current has been preferred. The injector baseline is described in [20] and the injector complex is shown in Fig. 2.5. It consists of:

- a 320 m long e^+e^- linac accelerating 1 or 2 bunches up to 6 GeV with repetition rate of 100-200 Hz, a target in the same linac for positron production at 4.46 GeV and a 242 m circumference damping ring at 1.54 GeV for both positron and electron beams [21]

- a pre-booster ring, probably in the Super Proton Synchrotron (SPS) tunnel, to accelerate $e^{\pm}$ from 6 to 20 GeV [22]
- a top-up booster ring to accelerate from 20 GeV to the FCC-ee ultimate collision energies [23]

Table 1 summarises the baseline beam parameters for all the physics programmes. These parameters were optimized by introducing a crab-waist collision scheme and by taking into account the lifetime limitation due to BS, the 3D flip-flop instability and the coherent X-Z instability [24].
The beam dynamics and electron cloud studies presented in this thesis will be focused on the Z resonance at 45.6 GeV, which represents the most challenging scenario from the beam stability point of view.

	Z	**W**	**H**	**tt**	
Circumference C [km]	97.75				
Bending radius ρ [km]	10.938				
Free length to IP l^* [m]	2.2				
Solenoid field at IP [T]	2.0				
Full crossing angle at IP [mrad]	30				
SR power/beam [MW]	50				
Beam energy E_0 [GeV]	45.6	80	120	175	182.5
Beam current [mA]	1390	147	29	6.4	5.4
Number of bunches/beam N_b	16640	2000	328	59	48
Bunch population N_p [10^{11}]	1.7	1.5	1.8	2.2	2.3
Momentum compaction α_c [10^{-5}]	1.48	1.48	0.73	0.73	0.73
Bunch length					
- $\sigma_{z,SR}$ [mm]	3.5	3.0	3.15	2.75	1.97
- $\sigma_{z,BS}$ [mm]	12.1	6.0	5.3	3.82	2.54
Energy spread					
- $\sigma_{dp,SR}$ [%]	0.038	0.066	0.099	0.144	0.150
- $\sigma_{dp,BS}$ [%]	0.132	0.131	0.165	0.196	0.192
Horizontal tune Q_x	269.139	269.124	389.129	389.104	
Vertical tune Q_y	269.219	269.199	389.199	389.175	
Synchrotron tune Q_s	0.025	0.0506	0.0358	0.0818	0.0872
Horizontal emittance ε_x [nm]	0.27	0.84	0.63	1.34	1.46
Vertical emittance ε_y [pm]	1.0	1.7	1.3	2.7	2.9
Longitudinal damping time [turns]	1273	236	70.3	23.1	20.4
SR energy loss/turn U_0 [GeV]	0.036	0.34	1.72	7.8	9.2
RF frequency [MHz]	400			400/800	
RF voltage V_{RF}[GV]	0.10	0.75	2.0	4.0/5.4	4.0/6.9
Horizontal β_x^* [m]	0.15	0.2	0.3	1.0	
Vertical β_y^* [mm]	0.8	1.0	1.0	1.6	
Horizontal size at IP σ_x^* [μm]	6.4	13.0	13.7	36.7	38.2
Vertical size at IP σ_y^* [nm]	28	41	36	66	68
Luminosity/IP [$10^{34}/cm^2s$]	230	28	8.5	1.8	1.55

Table 1: Machine parameters of FCC-ee for different energies, where SR and BS stand for synchrotron radiation and beamstrahlung.

3

COLLECTIVE EFFECTS IN PARTICLE ACCELERATORS

When a beam of charged particles propagates in an accelerator, it undergoes the Lorentz force produced by external electromagnetic fields provided by bending and focusing magnets (dipoles and quadrupoles, respectively) and RF cavities. However, the beam particles can also interact with themselves and with the surrounding environment, generating electromagnetic fields that can act back on the beam and perturb its motion. These additional fields must be included in the equations of motion of the beam particles, by considering in the Lorentz force the total electromagnetic fields given by the sum of the external and perturbation fields:

$$\vec{F} = q[(\vec{E}_{ext} + \vec{E}_{wake}) + \vec{v} \times (\vec{B}_{ext} + \vec{B}_{wake})] \tag{1}$$

The term *collective effects* refers to the class of phenomena in which the evolution of the beam depends on the combination of external fields and interaction between beam particles. Depending on the type of interaction, different categories of collective effects can be defined:

- space charge effects due to the interaction of beam particles with themselves and with a perfectly conducting vacuum chamber
- beam-beam effects due to interaction of the beam with the counter-rotating beam in a collider
- wakefield (in time domain) or impedance (in frequency domain) effects generated by the interaction of the beam with the vacuum chamber
- electron cloud effects due to the interaction between beam and electrons produced in the accelerator

All these perturbations can produce instabilities, in both longitudinal and transverse directions, thus representing one of the main limitations to the machine operation and performance. Studying these instabilities and their underlying mechanisms is an essential part in the design phase of any accelerator, since it allows identifying possible mitigation techniques and ensuring beam stability during operation. This chapter (and in general the research activity presented in this thesis) focuses on the study of the last two types of collective effects. Section 3.1 reviews the theory of wakefields and impedances in particle accelerators while electron cloud concepts will be described in Section 3.2.

3.1 WAKEFIELDS AND IMPEDANCES

In order to introduce wakefields and beam coupling impedances, let us consider the reference system of Fig. 3.1 where a source particle $q_1(z_1, \boldsymbol{r_1})$ and a test particle $q_2(z_2, \boldsymbol{r_2})$ are travelling with constant velocity $v \simeq c$, where c is the speed of light. The two particles are ultrarelativistic, therefore causality imposes that the test particle cannot affect the source. If the two particles move inside a perfectly conducting and smooth chamber the test particle does not feel any force. However, if the chamber presents some geometry variation or the pipe walls have a finite conductivity, the electromagnetic fields produced behind the source (and for this reason named *wake* fields) can act on the test particle and perturb its motion.

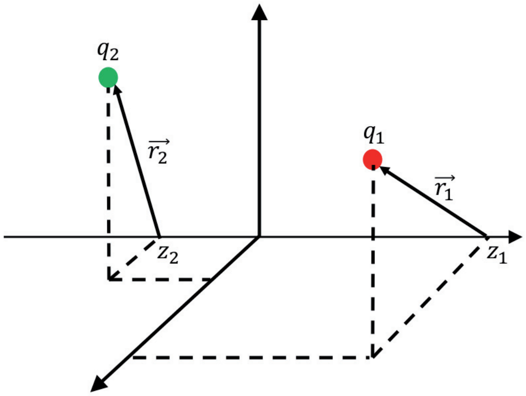

Figure 3.1: Reference system with a source particle q_1 (in red) and a test particle q_2 (in green).

3.1.1 *Wake functions and coupling impedances*

The Lorentz force generated by the source particle q_1 and acting on the test particle q_2 is given by

$$\boldsymbol{F} = q_2[E_z\hat{z} + (E_x - cB_y)\hat{x} + (E_y + cB_x)\hat{y}] = \boldsymbol{F}_{\|} + \boldsymbol{F}_{\perp} \tag{2}$$

where $\boldsymbol{E}$ and $\boldsymbol{B}$ are the electric and magnetic fields generated by q_1 inside the structure. This force is given by the sum of two components which have different effects on the test charge:

- a longitudinal force which changes its energy
- a transverse force which deflects its trajectory.

Considering a device of length L and assuming that the two particles are separated by a distance z which does not change during the passage through the structure (rigid beam approximation), the energy variation is defined as the integrated longitudinal force acting on the test particle along the length L of the object:

$$U(\boldsymbol{r_2}, \boldsymbol{r_1}, z) = \int_0^L F_{\|} ds \simeq U(z) \tag{3}$$

where $\boldsymbol{r_2}, \boldsymbol{r_1}$ are the transverse positions of the test and source charges, respectively.

The transverse deflecting kicks are distinguished in a dipolar kick defined as the integrated transverse force from an offset source acting on a on-axis test particle along the length L of the object:

$$\boldsymbol{M}^{dip}(\boldsymbol{r_2}, \boldsymbol{r_1}, z) = \int_0^L \boldsymbol{F}_{\perp}\Big|_{\boldsymbol{r_2}=\boldsymbol{0}} ds \simeq r_1 \boldsymbol{M}^{dip}(z) \tag{4}$$

and a quadrupolar kick defined as the integrated transverse force from an on-axis source acting on an offset test particle along the length L of the object:

$$\boldsymbol{M}^{quad}(\boldsymbol{r_2}, \boldsymbol{r_1}, z) = \int_0^L \boldsymbol{F}_{\perp}\Big|_{\boldsymbol{r_1}=\boldsymbol{0}} ds \simeq r_2 \boldsymbol{M}^{quad}(z) \tag{5}$$

The longitudinal wake function is defined as the energy change normalized by the two charges:

$$w_{\parallel}(z) = -\frac{U(z)}{q_1 q_2} \tag{6}$$

while the transverse dipolar and quadrupolar wake functions are given by the corresponding transverse kick normalized by the two charges and by the offset of the source and test particle, respectively:

$$\boldsymbol{w}_{\perp}{}^{dip}(z) = \frac{\boldsymbol{M}^{dip}(z)}{q_1 q_2} \tag{7}$$

$$\boldsymbol{w}_{\perp}{}^{quad}(z) = \frac{\boldsymbol{M}^{quad}(z)}{q_1 q_2} \tag{8}$$

One can observe that the longitudinal wake function given by Eq. 6 does not depend on the transverse positions $\boldsymbol{r_1}, \boldsymbol{r_2}$. In general, most of the structures in the beam pipe have a symmetric shape. In the particular case of cylindrical symmetry and ultrarelativistic charges, the wake function can be expanded in multipolar terms. In the longitudinal case, the first monopole term is dominant and the wake function depends only on z [25]. The minus sign in Eq. 6 means that for a positive wake the test particle is losing energy while a positive transverse wake correponds to a defocusing transverse force.

The longitudinal and transverse (dipolar and quadrupolar) beam coupling impedances are defined as the Fourier transforms of the wake functions in the frequency domain:

$$Z_{\parallel}(\omega) = \frac{1}{c}\int_{-\infty}^{+\infty} w_{\parallel}(z) e^{j\frac{\omega z}{c}} dz \tag{9}$$

$$\boldsymbol{Z}_{\perp}{}^{dip}(\omega) = -\frac{j}{c}\int_{-\infty}^{+\infty} \boldsymbol{w}_{\perp}{}^{dip}(z) e^{j\frac{\omega z}{c}} dz \tag{10}$$

$$\boldsymbol{Z}_{\perp}{}^{quad}(\omega) = -\frac{j}{c}\int_{-\infty}^{+\infty} \boldsymbol{w}_{\perp}{}^{quad}(z) e^{j\frac{\omega z}{c}} dz \tag{11}$$

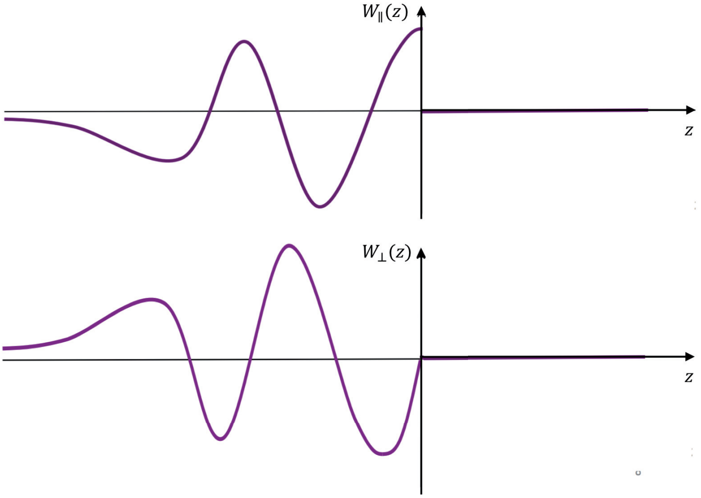

Figure 3.2: Example of longitudinal (top) and transverse (bottom) wake functions for ultrarelativistic particles ($\beta = 1$).

Another useful definition to introduce is the loss factor, i.e. the normalized energy lost by the source particle in the creation of the wake:

$$k = -\frac{U(z=0)}{q_1^2} = w_{\parallel}(z=0) \tag{12}$$

It is important to note that Eq. 12 is valid only for non ultrarelativistic particles while for charges travelling at the speed of light causality requires that the longitudinal wakefield is discontinuous at $z = 0$ with $w_{\parallel}(0^-) = 2 \cdot w_{\parallel}(0)$ and Eq. 12 is given by the beam loading theorem [26]:

$$k = \frac{w_{\parallel}(z \to 0^-)}{2} \tag{13}$$

This theorem states that an ultrarelativistic particle can only see half of its own wake and the wake exists only in the region $z < 0$, as shown in Fig. 3.2.

Also in the transverse case, the wake vanishes for $z > 0$ because of the ultrarelativistic approximation. For $z = 0$ it is equal to zero because source and test particles have the same longitudinal position and move in parallel and they can only interact through space charge, which is not discussed in this framework.

Examples of wakefields and impedances will be given in Chapter 5 (resistive wall impedance) and Chapter 7 (impedance generated by other machine devices as collimators, RF cavities, tapers, beam position monitors and bellows).

3.1.2 *Wake potentials and loss factors*

The wake functions generated by point charges and defined by Eqs. 6 - 8 are Green functions describing the response of the structure to an impulsive source. These quantities can be used to calculate the longitudinal and transverse wakefields produced by any bunch distribution.
Let us consider for example the longitudinal plane and a bunch with longitudinal distribution $\lambda(z)$. According to Fig. 3.3, the energy $dU(z)$ lost or gained by a test slice $e\lambda(z)dz$ at position z in the bunch can be obtained as the integral of the contributions from the wakefields generated by all the preceding slices $e\lambda(z')dz'$ at position z'. The energy loss of a bunch is then obtained by integrating $dU(z)$ over the full bunch extension:

$$U(z) = \int_{-\infty}^{+\infty} dU(z)dz = -e^2 \int_{-\infty}^{+\infty} \lambda(z)dz \int_{z}^{+\infty} \lambda(z')w_{\parallel}(z'-z)dz' \quad (14)$$

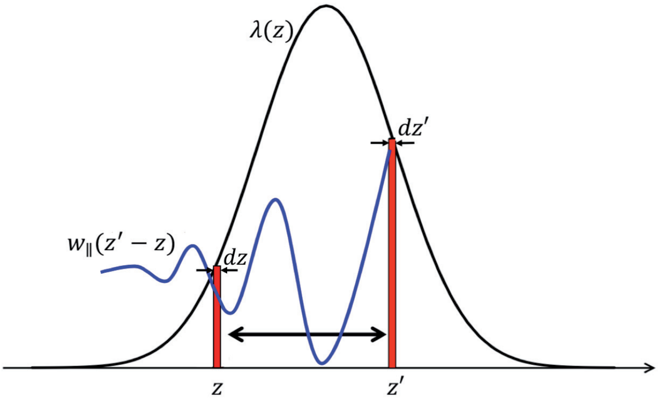

Figure 3.3: Convolution integral to compute the energy loss of a slice due to the entire bunch.

or in terms of Fourier transforms [27]:

$$U = -\frac{e^2}{2\pi}\int_{-\infty}^{\infty}|\Lambda(\omega)|^2 Re[Z_{\|}(\omega)]d\omega \tag{15}$$

where $\Lambda(\omega)$ is the bunch spectrum and $Re[Z_{\|}(\omega)]$ is the real part of the longitudinal beam coupling impedance.
The longitudinal wake potential of the distribution is given by the convolution between the longitudinal wake function $w_{\|}(z)$ and the bunch distribution $\lambda(z)$:

$$W_{\|}(z) = \int_{-\infty}^{z} w_{\|}(z'-z)\lambda(z')dz' \tag{16}$$

while the longitudinal loss factor is obtained by integrating the product of the wake potential and the bunch distribution:

$$k_{\|} = \int_{-\infty}^{+\infty} W_{\|}(z)\lambda(z)dz \tag{17}$$

By substituting Eqs. 16 and 17 in Eq. 14, the energy loss of a bunch can be written in terms of loss factor as

$$U(z) = -e^2 k_{\|} \tag{18}$$

It is important to note that Eqs. 14 and 15 are valid for a bunch passing through the impedance once. By considering also the wakes generated during the previous turns, Eqs. 14 and 15 can be generalized respectively as [27]:

$$U(z) = -e^2\int_{-\infty}^{+\infty}\lambda(z)dz\int_{-\infty}^{+\infty}\lambda(z')\sum_{k=-\infty}^{+\infty} w_{\|}(kC+z'-z)dz' \tag{19}$$

$$U = -\frac{e^2\omega_0}{2\pi}\sum_{p=-\infty}^{\infty}|\Lambda(p\omega_0)|^2 Re[Z_{\|}(p\omega_0)] \tag{20}$$

where C is the accelerator circumference, k sums over turns and $\omega_0 = \frac{2\pi c}{C}$ is the revolution frequency.

The total energy lost by a bunch particle has to be compensated by the RF system every turn with a synchronous phase shift:

$$U = -\Delta\phi e V_{RF} cos(\phi_s) \tag{21}$$

where $\Delta\phi$ is the phase shift for a given bunch intensity, ϕ_s is the synchronous phase and V_{RF} is the RF voltage. From Eqs. 18 and 21, one can obtain the following formula for the longitudinal loss factor:

$$k_{\|} = \frac{\Delta\phi V_{RF} cos(\phi_s)}{eN_p} \tag{22}$$

In the particular case of a uniformly filled machine, i.e. a train of N_b equally spaced bunches covering the full ring circumference with bunch spacing $\tau_b = \frac{2\pi}{h\omega_0}$ where $h = N_b$ is the harmonic number, the total energy loss of the beam is given by:

$$U = -\frac{e^2 N_b^2 N_p^2 \omega_0}{2\pi} \sum_{p=-\infty}^{\infty} |\Lambda(pN_b\omega_0)|^2 Re[Z_{\|}(pN_b\omega_0)] \tag{23}$$

where N_p is the bunch population, and the total power loss is equal to

$$P_{loss} = \frac{U}{t_0} = I^2 \sum_{p=-\infty}^{+\infty} |\Lambda(pN_b\omega_0)|^2 Re[Z_{\|}(pN_b\omega_0)] \tag{24}$$

where $I = \frac{N_b N_p e}{t_0}$ is the average beam current with t_0 the revolution period of the machine.

The energy loss of a beam is very important. The fraction of the energy lost on the pipe walls or on other devices installed in the machine can be very dangerous, because it causes extra heating of the equipment with eventual damage.

Similar definitions can be applied in the transverse plane for the transverse wake potential:

$$W_{\perp}(z) = \int_{-\infty}^{z} w_{\perp}(z' - z)\lambda(z')dz' \tag{25}$$

and the transverse loss factor, also called kick factor, since it represents the deflection or kick exerted by the electromagnetic fields on the beam:

$$k_{\perp} = \int_{-\infty}^{+\infty} W_{\perp}(z)\lambda(z)dz \tag{26}$$

3.1.3 *Wakefield and impedance of a resonator*

When a charge propagates through accelerator devices like cavities, collimators, etc., it excites resonant modes that can be described as parallel RLC circuits loaded by a point charge impulsive current $I(t) = q\delta(t)$, as shown in Fig. 3.4. This system is characterized by a shunt impedance R, an inductance L, a capacity C, a resonant frequency $\omega_r = \frac{1}{\sqrt{LC}}$ and a quality factor $Q = R\sqrt{\frac{C}{L}} = \frac{R}{L\omega_r} = RC\omega_r$.
In this circuit, the voltages across each component are given by

$$\begin{aligned} V_R &= RI_R \\ V_C &= \frac{1}{C}\int I_C dt \\ V_L &= L\frac{dI_L}{dt} \end{aligned} \tag{27}$$

and the following relations hold:

$$\begin{aligned} V_R = V_C = V_L &= V \\ I_R + I_C + I_L &= I \end{aligned} \tag{28}$$

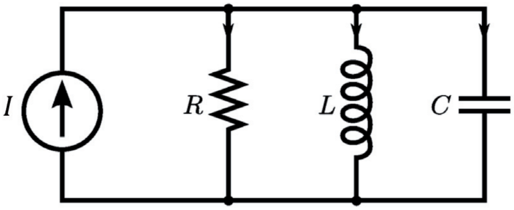

Figure 3.4: Scheme of a parallel RLC circuit representing a resonant mode.

Differentiating Eq. 28 and dividing by C, one can obtain the following differential equation:

$$\ddot{V} + \frac{\dot{V}}{RC} + \frac{V}{LC} = \frac{1}{C}\dot{I} \tag{29}$$

Using $C = \frac{Q}{R\omega_r}$ and $L = \frac{R}{Q\omega_r}$, Eq. 29 can be written as

$$\ddot{V} + \frac{\omega_r}{Q}\dot{V} + \omega_r^2 V = \frac{R\omega_r}{Q}\dot{I} \tag{30}$$

The solution of the homogeneus equation is a damped oscillation in the form

$$V(t) = e^{-\alpha t}\left[A\cos\left(\omega_r\sqrt{1-\frac{1}{4Q^2}}t\right) + B\sin\left(\omega_r\sqrt{1-\frac{1}{4Q^2}}t\right)\right] \tag{31}$$

where $\alpha = \frac{\omega_r}{2Q}$ is the damping rate and A, B determine the amplitude of the oscillations that depend on the initial conditions

$$V(0^+) = \frac{q}{C} = \frac{R\omega_r}{Q}q \tag{32}$$

$$\dot{V}(0^+) = -\frac{\dot{q}}{C} = -\frac{I(0^+)}{C} = \frac{V(0^+)}{RC} = \frac{R\omega_r^2}{Q^2}q \tag{33}$$

By solving Eqs. 32 and 33, the voltage induced by the source charge q passing through the cavity becomes [28]

$$V(t) = q\frac{R\omega_r}{Q}e^{-\alpha t}\left[\cos\left(\omega_r\sqrt{1-\frac{1}{4Q^2}}t\right) - \frac{\sin\left(\omega_r\sqrt{1-\frac{1}{4Q^2}}t\right)}{2Q\sqrt{1-\frac{1}{4Q^2}}}\right] \tag{34}$$

The energy gained or lost by a test particle q' will be then given by

$$U = q'V(T) \tag{35}$$

According to Eq. 6, this quantity divided by the two charges gives the longitudinal wake function:

$$\omega(t) = 2ke^{-\alpha t}\left[\cos\left(\omega_r\sqrt{1-\frac{1}{4Q^2}}t\right) - \frac{\sin\left(\omega_r\sqrt{1-\frac{1}{4Q^2}}t\right)}{2Q\sqrt{1-\frac{1}{4Q^2}}}\right] \tag{36}$$

where

$$k = \frac{R\omega_r}{2Q} \tag{37}$$

is the loss factor. The Fourier transform of Eq. 36 gives the longitudinal coupling impedance of a resonant mode:

$$Z_{\parallel}(\omega) = \frac{R}{1 + jQ\left(\frac{\omega_r}{\omega} - \frac{\omega}{\omega_r}\right)} \tag{38}$$

Broadband impedances have quality factor $Q \simeq 1$ and correspond to short-range wakefields which act over the bunch length, thus affecting the single bunch dynamics: in this case particles experience the wakefields produced by the other preceding particles of the same bunch. Narrowband impedances, given for example by resonant HOMs in a cavity, have $Q \gg 1$ and correspond instead to long range wakefields which act over the length of bunch trains or several machine turns, thus affecting the multi bunch dynamics.

The effects of wakefields on both single bunch and multibunch dynamics will be presented in Chapters 5 and 7.

Another broadband impedance model was proposed by S. Heifets and K. Bane [29–31] and it describes the longitudinal impedance by expansion over $\sqrt{\omega}$:

$$Z(\omega) = j\omega L + R + (1 + jsign(\omega))\sqrt{|\omega|}B + \frac{1 - jsign(\omega)}{\sqrt{|\omega|}}\tilde{Z}_c + ... \tag{39}$$

where the coefficients $L, R, B, \tilde{Z}_c, ...$ are real.

The terms of this expansion represent the impedances of particular devices and will be used in Chapter 7 to characterize the wake potentials of different components of the lepton collider FCC-ee.

3.2 ELECTRON CLOUD

Electron cloud (EC) has been recognized as one of the main limitations in the performance of both lepton and hadron machines [32–35]. Figure 3.5 shows a sketch of the formation of an electron cloud. When a beam with positively charged particles passes through a section of an accelerator,

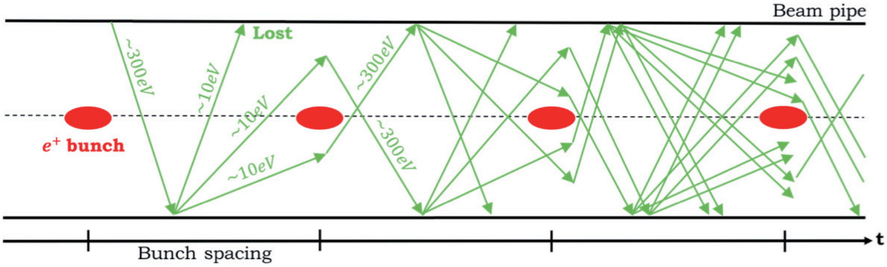

Figure 3.5: Sketch of the formation of an electron cloud in a section of the machine.

primary electrons can be produced in the beam chamber by different mechanisms like ionization of the residual gas or photoemission due to SR (and in this case one refers to photoelectrons). These primaries are attracted and accelerated by the beam up to energies of several hundreds of eV. When the electrons strike the chamber walls with these energies, they produce secondary electrons that in turn, depending on their energy, can be absorbed, reflected or accelerated again by the following bunch, thus producing an avalanche of electron multiplication (the so called multipacting effect). This accumulation of electrons can interact with the pipe walls, causing the heating of the vacuum chamber and degradation of vacuum and diagnostics elements, or with the beam itself, inducing transverse instabilities, emittance growth, tune shift and spread and beam losses. The following sections will introduce the two mechanisms involved in the formation of an EC, the different regimes during the build up and the secondary emission model used for all the studies presented in this thesis.

3.2.1 *Primary electron production*

Electrons can be produced in the beam chamber through two main mechanisms (or their combination).

- **Residual gas ionization**
  This mechanism is always present and in machines with very intense and bright beams it may become the dominant process of primary electron production. Residual gas in the vacuum chamber can be ionized by the

beam producing free electron-ion pairs with a production rate per unit volume given by

$$\frac{dn_{ion}}{dt} = \sigma_{ion} n_{gas} \phi_p \tag{40}$$

where σ_{ion} is the ionization cross section of the residual gas [36], n_{gas} is the gas density and ϕ_p is the beam particle flux per unit area.

- **Photoemission due to SR**
  In the case of leptons and in general of high energy particle beams as protons in the LHC that emit a significant amount of SR, electrons generated by photoemission from the chamber's wall are the main source of primary electrons. When charged particles are subject to a transverse acceleration, they emit photons that can have enough energy to extract electrons from the walls when hitting the pipe (photoelectric effect). These electrons are called photoelectrons and in the case of FCC-ee they represent the main source of primaries in the EC build up.
  The number of photons per unit length emitted by a particle having relativistic factor γ and following a circular trajectory with bending radius ρ is equal to [37]

  $$N_\gamma = \frac{5\alpha}{2\sqrt{3}} \frac{\gamma}{\rho} \tag{41}$$

  where α is the fine-structure constant, while the critical energy of the radiation is given by

  $$E_c = \frac{3\hbar c \gamma^3}{2\rho} \tag{42}$$

  where $\hbar$ is the reduced Planck constant. These photons are radiated within a very narrow cone characterized by an opening angle inversely proportional to γ.
  The total number of photoelectrons per particle per unit length is given by

  $$N_{pe} = N_\gamma Y \tag{43}$$

  where Y is the photoelectron yield or quantum efficiency, i.e. the probability of electron emission per impinging photon. Only a fraction of these photoelectrons are generated by photons coming directly from the beam.

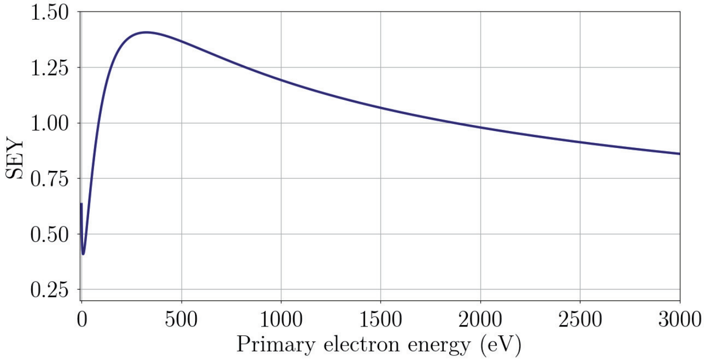

Figure 3.6: SEY curve as a function of the primary electrons energy.

Another fraction of photoelectrons is produced by scattered photons and is associated to the photon reflectivity R:

$$N_{pe,r} = N_{pe}R \tag{44}$$

3.2.2 *Secondary electron emission*

The secondary electron emission process is described through the so called Secondary Electron Yield (SEY) which is a property of the surface material defined ad the ratio between the electron current impinging the wall and the corresponding emitted current:

$$\delta(E,\theta) = \frac{I_{emit}}{I_{imp}(E,\theta)} \tag{45}$$

This quantity strongly depends on the impacting energy E of primary electrons, the angle of incidence θ and the material. Figure 3.6 shows a typical SEY curve as a function of the energy of primary electrons.
All the EC build up simulations presented in this thesis are based on the secondary emission model described in [38, 39]. In this model, the SEY is given by the sum of two terms (see Fig. 3.7):

$$\delta(E) = \delta_{elas}(E) + \delta_{true}(E) \tag{46}$$

The first component corresponds to electrons which are elastically reflected

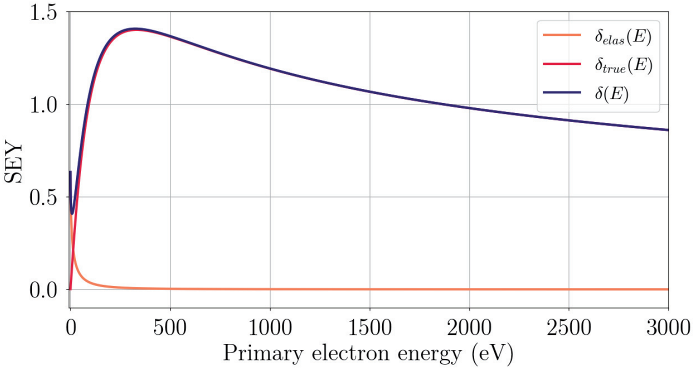

Figure 3.7: SEY curve: elastic component δ_{elas}, true secondary component δ_{true} and total δ_E.

by the surface and is given by

$$\delta_{elas}(E) = R_0 \left(\frac{\sqrt{E} - \sqrt{E + E_0}}{\sqrt{E} + \sqrt{E + E_0}} \right)^2 \tag{47}$$

where the two parameters R_0 and E_0 are obtained from measured data and set to 0.7 and 150 eV for a copper surface as the LHC beam screen [38].
The second component corresponds to the so called "true secondaries" and is equal to

$$\delta_{true}(E) = \delta_{max} \frac{s \frac{E}{E_{max}}}{s - 1 + \left(\frac{E}{E_{max}} \right)^s} \tag{48}$$

where

$$\delta_{max} = \delta(E_{max}) \simeq \delta_{true}(E_{max}) \tag{49}$$

represents the maximum value of the SEY curve and the parameters s and E_{max} have been determined experimentally for the copper surface of the LHC beam screens and found to be 1.35 and 332 eV, respectively [38].
As already mentioned, the SEY also depends on the angle of incidence θ defined with respect to the normal to the surface, according to the following equations [38]:

$$E_{max}(\theta) = E_{max}(\theta = 0)[1 - 0.7(1 - \cos\theta)] \tag{50}$$

$$\delta_{max}(\theta) = \delta_{max}(\theta = 0)e^{\frac{1-\cos\theta}{2}} \tag{51}$$

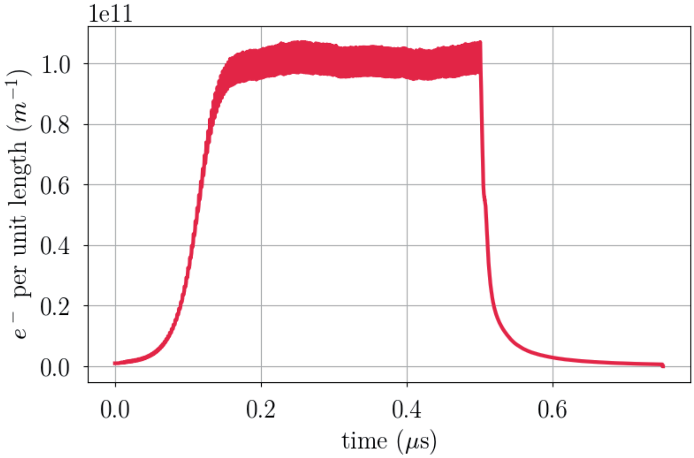

Figure 3.8: Time evolution of the total number of electrons in the chamber of the FCC-ee arc dipoles for δ_{max} = 1.6.

3.2.3 *Electron cloud build up regimes*

The SEY curve can be divided in two main regions: one region with $\delta(E,\theta) < 1$ where the pipe walls act as electron absorbers and another region with $\delta(E,\theta) > 1$ where the material behaves like an electron emitter. In the first case, the number of primary electrons produced in the chamber is balanced by the number of electrons absorbed by the surface and an equilibrium condition is reached (**seed accumulation regime**). When $\delta(E,\theta) > 1$ the electron density grows exponentially in the vacuum chamber and the build up is in **multipacting regime**.

Figure 3.8 shows the total number of electrons in the FCC-ee dipole chamber during the passage of a train of 200 positron bunches followed by 100 empty bunches in the case of δ_{max}=1.6 and 2.5 ns bunch spacing. One can observe that after a certain amount of time the evolution of electrons reaches a saturation level due to the space charge in the cloud of electrons and then it decays after the passage of the train.

4

ELECTRON CLOUD STUDIES

In the case of FCC-ee, the EC build up in the positron ring can be very dangerous for the machine operation and for that reason it has to be analyzed with particular care. This chapter presents EC studies for the lepton collider at 45.6 GeV. Numerical simulations have been performed with the PyECLOUD code that will be briefly described in Section 4.1. In this thesis work, additional tools have been developed in PyECLOUD to extend its validity range and to make it suitable for the lepton collider. This new implementation will be described in Section 4.2, while Sections 4.3- 4.5 will present the main results of EC build up simulations in the drift spaces and in all the magnets of the machine (dipoles and quadrupoles in the arcs and final focusing quadrupoles in the IR). Section 4.6 will discuss the single bunch head tail instability driven by EC.

4.1 THE PYECLOUD CODE

PyECLOUD [38,40] is a 2D macroparticle (MP) code written in Python and developed at CERN to simulate the EC build up in particle accelerators. This code uses most of the physics models of the ECLOUD code [41], but it was improved in terms of computational time, accuracy and flexibility, thanks to its modular structure and the more powerful programming language. In PyECLOUD, electrons are grouped in MPs and the EC build up is simulated by following the loop shown in Fig. 4.1 [38]:

- At each time step Δt, primary electrons are generated in the vacuum chamber by residual gas ionization or photoemission due to SR.
- The electric field of the beam is computed first at the nodes of a rectangular grid defined over the entire chamber and then at each MP location by a linear interpolation.
- The electric field due to space charge forces within the EC is computed by a Particle In Cell (PIC) algorithm that will be described later in this chapter.

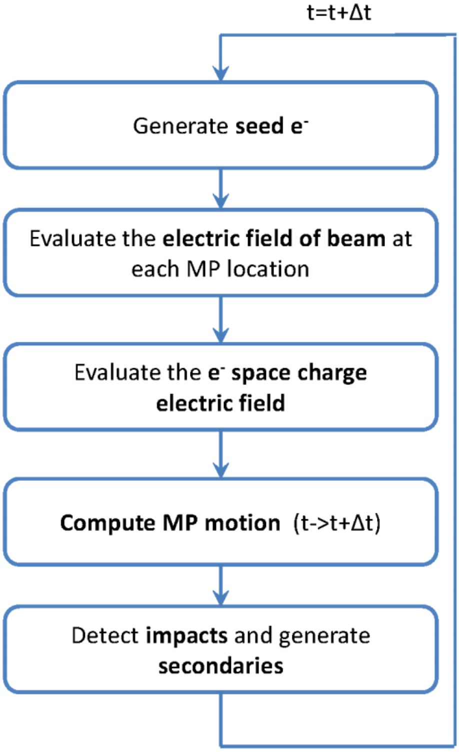
t=t+Δt
Generate **seed e⁻**
Evaluate the **electric field of beam** at each MP location
Evaluate the **e⁻ space charge electric field**
Compute MP motion (t->t+Δt)
Detect **impacts** and generate **secondaries**

Figure 4.1: PyECLOUD main loop for EC build up simulations.

- Given the total electric field at each MP location, a tracking algorithm allows updating the position and velocity of each MP, also taking into account eventual externally applied magnetic fields.
- For the electrons hitting the pipe walls, the most important impact parameters are computed (kinetic energy, velocity, impact angle, etc.) and a secondary emission module (based on the secondary emission model described in Section 3.2.2) is applied to generate secondary electrons.

One of the main improvements of PyECLOUD with respect to ECLOUD is the MP size management described in [38] to dinamically adapt the number and size of MPs during a simulation. This method allowed reducing the simulation time and had a significant impact on convergence properties [42]. Recently, another important feature has been implemented in PyECLOUD, namely a multigrid PIC solver that will be described in the next section.

4.2 PYPIC: THE MULTIGRID SOLVER

The multigrid algorithm [43] was implemented in the PyPIC solver of PyECLOUD to cope with the very small beam sizes of FCC-ee and LHC at top energy. When using the PIC algorithm to compute the e^- space charge electric field, a grid with $N_x \times N_y$ nodes and grid size Δh is defined over the entire chamber. In order to obtain reliable simulation results, the grid size and the beam size should be of the same order of magnitude and at least 2-3 meshes should be considered inside the beam. Depending on the beam pipe dimensions, this could require a very large number of nodes, thus making the simulation very time consuming. An important feature of the multigrid solver is that the PIC resolution is not uniform over the simulation domain: the use of multiple nested grids with different resolution allows refining the accuracy of the algorithm only around the beam where it is needed. This new implementation is based on the mesh refinement method described in [44].

4.2.1 *Dualgrid implementation*

The first step has been the implementation of the simplest dualgrid method, consisting of two grids: the main grid defined over the full chamber and an internal new grid with finer resolution placed around the beam location, as shown in Fig. 4.2. The space charge field of the EC is then computed as follows:

- **Scatter**
  The scatter routine is the same described in [38] and is performed for both main and internal grids. The charge n_{MP} of each MP at location (x_{MP}, y_{MP}) is scattered to the four neighbouring nodes of the grid (see Fig. 4.3) and the charge density is computed as:

$$\begin{aligned} \rho_{i,j} &= \rho_{i,j} + \frac{q\,n_{MP}}{\Delta h}\left(1-\frac{d_x}{\Delta h}\right)\left(1-\frac{d_y}{\Delta h}\right) \\ \rho_{i+1,j} &= \rho_{i+1,j} + \frac{q\,n_{MP}}{\Delta h}\left(\frac{d_x}{\Delta h}\right)\left(1-\frac{d_y}{\Delta h}\right) \\ \rho_{i,j+1} &= \rho_{i,j+1} + \frac{q\,n_{MP}}{\Delta h}\left(1-\frac{d_x}{\Delta h}\right)\left(\frac{d_y}{\Delta h}\right) \\ \rho_{i+1,j+1} &= \rho_{i+1,j+1} + \frac{q\,n_{MP}}{\Delta h}\left(\frac{d_x}{\Delta h}\right)\left(\frac{d_y}{\Delta h}\right) \end{aligned} \tag{52}$$

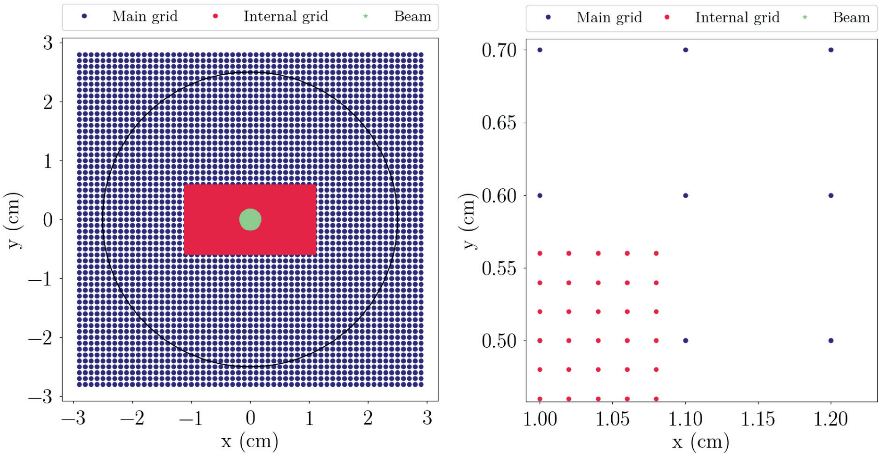

Figure 4.2: Dualgrid implementation. On the left side: an internal grid (in red) is placed around the beam (in green), in addition to the main grid (in blue) defined over the entire chamber. On the right side: the resolution of the new grid is finer compared to the main grid.

where

$$i = \left(\frac{x_{MP} - x_0}{\Delta h}\right), \quad j = \left(\frac{y_{MP} - y_0}{\Delta h}\right) \tag{53}$$

are the indexes of the neighbouring grid nodes, with x_0, y_0 the bottom left corner of the grid and Δh the size of the grid, and

$$d_x = x_{MP} - x_0 - i\Delta h, \quad d_y = y_{MP} - y_0 - j\Delta h \tag{54}$$

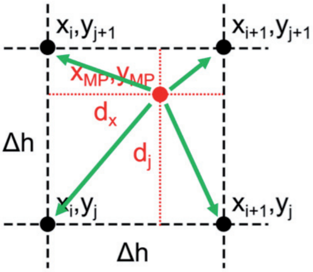

Figure 4.3: Distances and grid nodes used in the scatter routine for the computation of the space charge field.

- **Solve**
  The electrostatic potential is computed at the internal nodes of each grid by solving the Poisson equation with the Finite Difference (FD) method:

$$\frac{\phi_{i-1,j} + \phi_{i,j-1} - 4\phi_{i,j} + \phi_{i+1,j} + \phi_{i,j+1}}{\Delta h^2} = -\frac{\rho_{i,j}}{\epsilon_0} \tag{55}$$

  with different boundary conditions for the two grids:

  - the electrostatic potential on the boundary of the main grid is set equal to zero
  - the boundary condition for the internal grid is the solution of the Poisson equation from the previous coarser level, i.e. in the simple case of a dualgrid the potential computed at the internal nodes of the main grid.

- **Electric field computation**
  The electric field is evaluated at the internal nodes of each grid using a central difference formula:

$$E_{x\,i,j} = -\frac{\phi_{i+1,j} - \phi_{i-1,j}}{2\Delta h}, \quad E_{y\,i,j} = -\frac{\phi_{i,j+1} - \phi_{i,j-1}}{2\Delta h} \tag{56}$$

- **Gather**
  The electric field is interpolated at each MP location from internal grid nodes for the MPs falling inside the internal grid and from the main grid nodes for all the other MPs:

$$\begin{aligned} E(x_{MP}, y_{MP}) =& E_{i,j}\left(1 - \frac{d_x}{\Delta h}\right)\left(1 - \frac{d_y}{\Delta h}\right) + E_{i+1,j}\left(\frac{d_x}{\Delta h}\right)\left(1 - \frac{d_y}{\Delta h}\right) + \\ & + E_{i,j+1}\left(1 - \frac{d_x}{\Delta h}\right)\left(\frac{d_y}{\Delta h}\right) + E_{i+1,j+1}\left(\frac{d_x}{\Delta h}\right)\left(\frac{d_y}{\Delta h}\right) \end{aligned} \tag{57}$$

  It is important to note that this approach introduces an artifact due to a spurious image of a particle at the interface between the coarse and the fine grid resolution, as shown in Fig. 4.4. This artifact can be avoided by discarding the most external nodes of the internal grid during interpolation, as described in [45].

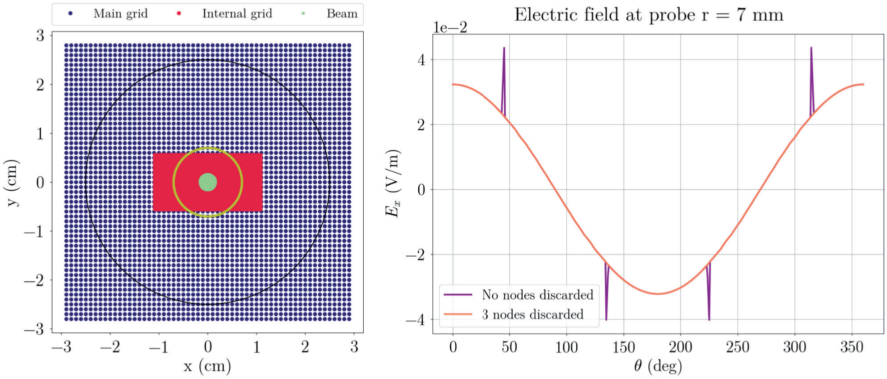

Figure 4.4: Horizontal component of the electric field computed at probe r = 7 mm (yellow line on the left plot) which crosses the edges of the internal grid. The artifact can be minimized by discarding the most external cells of the internal grid during interpolation.

Several tests have been performed to check the reliability of the code and to evaluate its accuracy. The dualgrid implementation was tested considering a 2 mm radius uniform charge distribution within a 30 mm radius circular chamber. In this first study, a main grid with 0.5 mm mesh size and an internal grid with 0.1 mm mesh size have been considered. The electric field was computed outside the beam (at a probe r = 20 mm) by using both the singlegrid and the dualgrid methods and then compared with the analytical radial electric field of an infinite cylinder of uniform volume charge density given by

$$E_r = \frac{q}{2\pi\epsilon_0 r} \tag{58}$$

with transverse components

$$\begin{aligned} E_x &= E_r \cos\theta = E_r \frac{x}{r} \\ E_y &= E_r \sin\theta = E_r \frac{y}{r} \end{aligned} \tag{59}$$

Results are reported in Fig. 4.5, showing that both pics give good accuracy outside the charge while at a probe r = 2 mm very close to the beam the electric field is more accurate by using the dualgrid method, due to the higher resolution of the internal grid, as shown in Fig. 4.6.

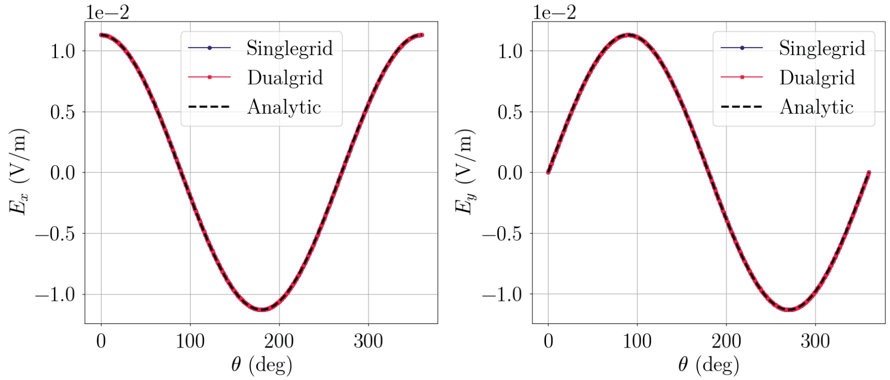

Figure 4.5: Horizontal (left) and vertical (right) components of the electric field computed at a probe r = 20 mm by using analytical, singlegrid and dualgrid methods.

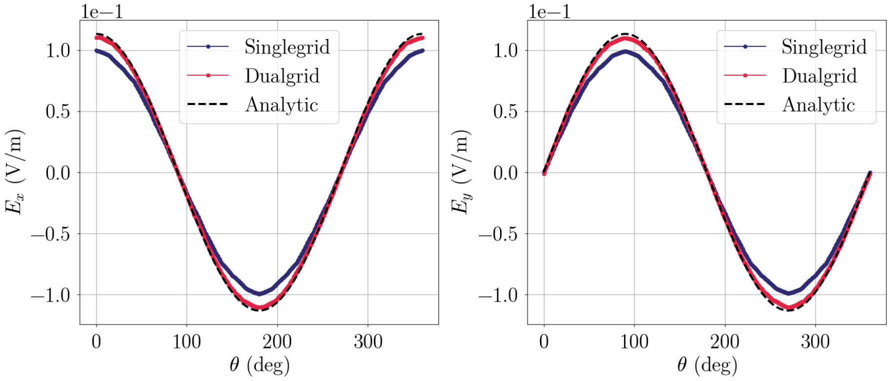

Figure 4.6: Horizontal (left) and vertical (right) components of the electric field computed at a probe r = 2 mm by using analytical, singlegrid and dualgrid methods.

4.2.2 *Multigrid implementation*

Thanks to the modular structure of PyPIC, it was possible to generalize the dualgrid module for an arbitrary number of nested grids. Fig. 4.7 shows the grids configuration implemented in the multigrid solver. If $S_i (i = 0, ..., n)$ is the size of the i-th internal grid, we want to impose:

$$S_i = f S_{i-1} \tag{60}$$

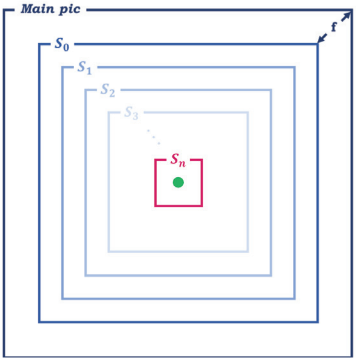

Figure 4.7: Multiple nested grid configuration implemented in the multigrid solver.

where $0 < f < 1$ is the magnification factor between two consecutive grids. Therefore, the final internal grid around the beam is given by

$$S_n = f^n S_0 \tag{61}$$

where S_0 is the size of the refinement grid of the main pic expressed as

$$S_0 = N\Delta h_0 \tag{62}$$

with N the minimum number of points of the first internal grid in the mesh size Δh_0 of the main grid. The parameters $N, \Delta h_0$ and f can be defined by the user in the simulation input files. The user also provides the coordinates $x_{min}, x_{max}, y_{min}, y_{max}$ of the vertexes of the target grid and its mesh size Δh_{target}.

Once the multigrid parameters are specified, by substituting Eq. 62 in Eq. 61, the size of the most internal grid can be obtained as

$$S_n = f^n N\Delta h_0 \tag{63}$$

From Eq. 63, we can derive the number of grids needed in the simulation to reach the required accuracy:

$$n_{grids} = \frac{ln(\frac{S_n}{N\Delta h_0})}{ln(f)} \tag{64}$$

By approximating this number to the smallest integer i such that $i \geq n$, the exact magnification factor is given by

$$f_{exact} = \sqrt[n]{\frac{S_{target}}{N\Delta h_0}} \tag{65}$$

and each coarser grid can be obtained by applying the formula

$$S_i - 1 = \frac{S_i}{f_{exact}} \quad (i = 0, ..., n) \tag{66}$$

The multigrid benchmarking was performed by considering first the LHC Gaussian beam at top energy with transverse sizes $\sigma_{x,y} = 0.33$ mm, within an elliptical chamber of dimensions 22×18 mm.
In general, a good setting for the multigrid solver is the following:

- $S_{x,target} = 10\sigma_x \Rightarrow x_{\substack{max \\ min}} = \pm 5\sigma_x$
- $S_{y,target} = 10\sigma_y \Rightarrow y_{\substack{max \\ min}} = \pm 5\sigma_x$
- $\Delta h_{target} = 0.3 \cdot \min(\sigma_x, \sigma_y)$

As in the previous test, the electric field components have been computed at a probe 1σ by using both singlegrid and multigrid methods, and then compared with the analytical electric field evaluated using the Bassetti-Erskine formula [46] for an elliptical chamber. Results are shown in Fig. 4.8: the estimation of the electric field in the vicinity of the beam is more accurate by using the multigrid method, due to the higher resolution of the inner grid ($\Delta h_{multi} = 9.89 \cdot 10^{-5}$ m, $\Delta h_{single,BE} = 1.65 \cdot 10^{-4}$ m).
In order to determine the error of the two methods w.r.t. the analytic estimation and the computational time of each solver, the same test has been performed considering a mesh size of $\Delta h = 9.89 \cdot 10^{-5}$ m for all methods. Fig. 4.9 shows the RMS error of the two methods compared to the analytic computation as a function of the distance from the beam: both methods show an error below 2%.
In terms of computational time, the multigrid solver significantly increases the simulation speed, as it can be easily seen in Fig. 4.10. Although the scattering time is higher for the multigrid solver (the scatter routine has to be performed for all the grids), the solving time, proportional to the

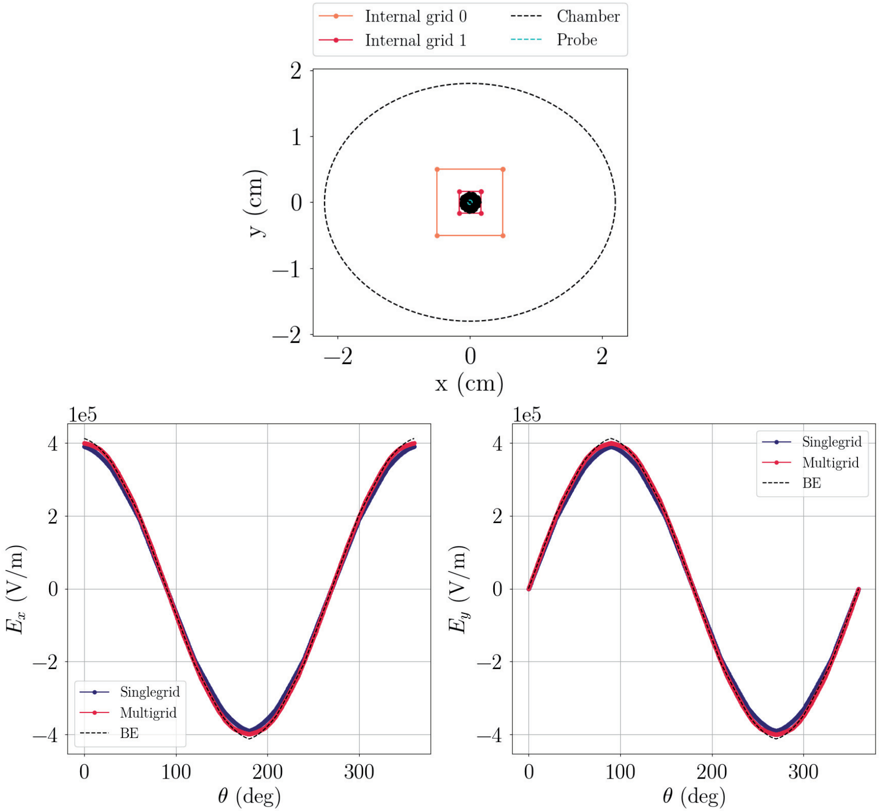

Figure 4.8: Multigrid configuration (top), horizontal and vertical components of the electric field (bottom) computed at a probe 1σ by using analytical Bassetti-Erskine formula, singlegrid and multigrid methods.

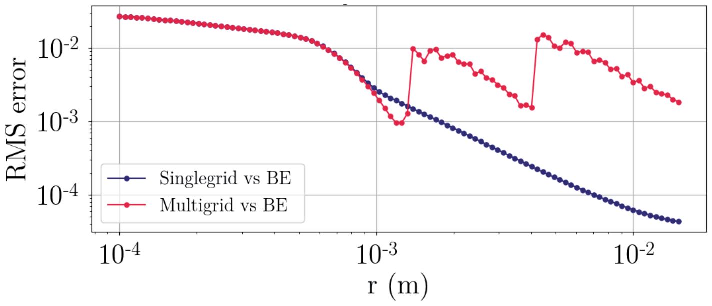

Figure 4.9: RMS error w.r.t. the analytical Bassetti-Erskine formula on the computation of the electric field as a function of the distance from the bunch center.

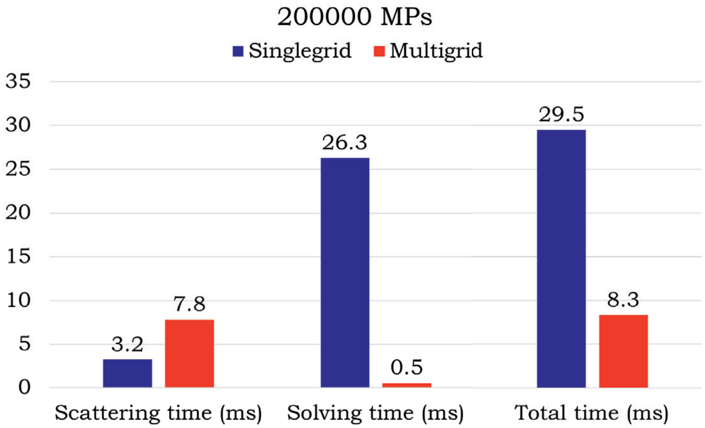

Figure 4.10: Scattering time and solving time required in simulation by using singlegrid and multigrid methods.

number of nodes, is about 50 times lower.

The multigrid solver has also been tested to the challenging case of FCC-ee at 45.6 GeV, by considering the same elliptical chamber of the LHC, and the electric field has been evaluated for all internal grids with different mesh sizes. Simulation results shown in Fig. 4.11 revealed that for such a machine EC studies would not have been possible without the support of this new implementation.

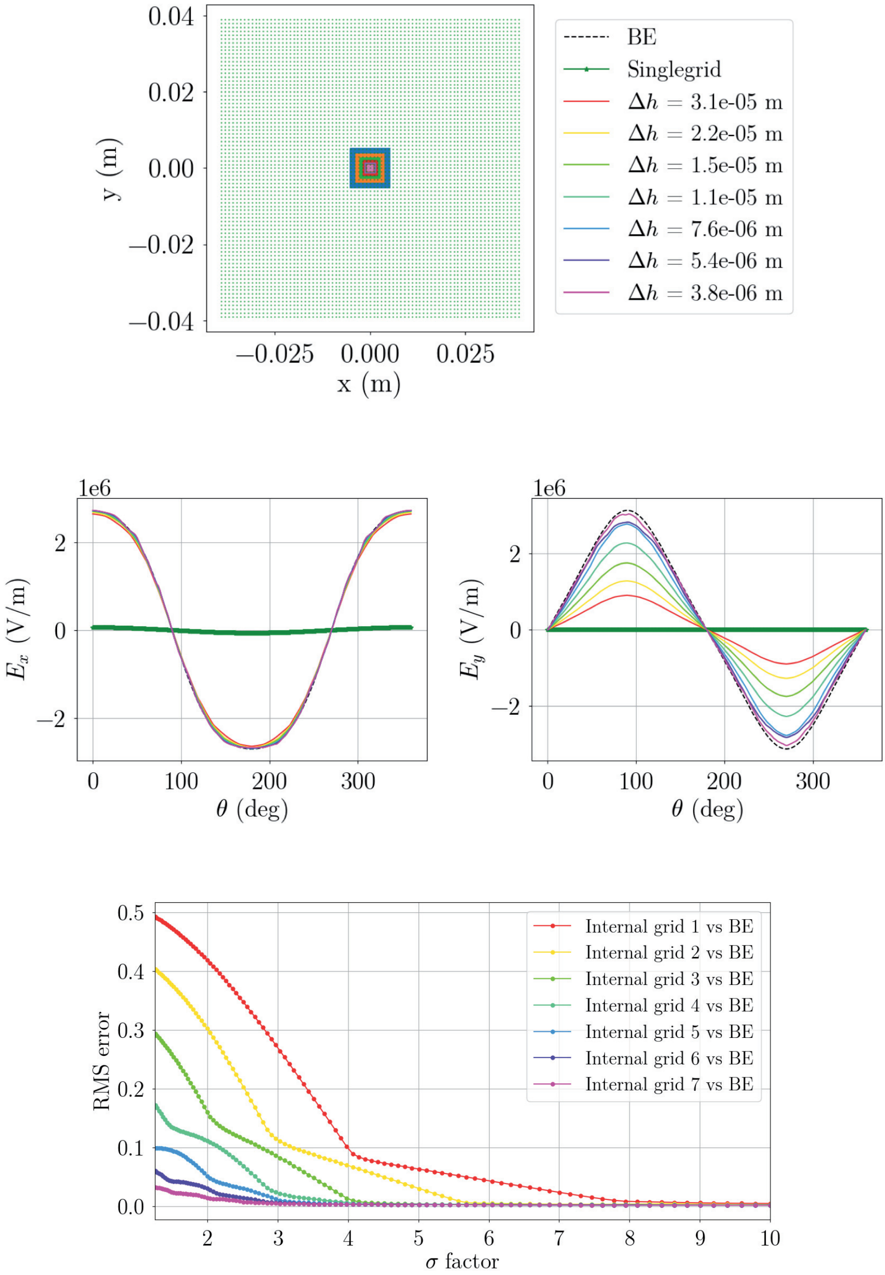

Figure 4.11: Multigrid configuration (top), electric field components (centre) and RMS error of all internal grids with different resolutions compared with the analytic one obtained by using the Bassetti-Erskine formula.

4.3 SIMULATION STUDIES FOR THE FCC-EE ARC COMPONENTS

About 90% of the total length of FCC-ee is occupied by dipole and quadrupole magnets. Although the lepton collider is a warm machine without any cryogenic component, the accumulation of electrons in the beam chamber of these magnets can represent an important source of heat load and produce transverse instabilities, thus limiting the machine performance. Therefore, PyECLOUD numerical simulations have been performed to study the EC build up in the drift space and all the magnets of the arcs and its dependence on bunch spacing. On the Z resonance, the arcs of FCC-ee are based on FODO cells with 60°/60° phase advance. Each cell contains two main dipoles with lengths of 21.94 m and 23.44 m and twin-aperture focusing and defocusing quadrupoles with the same length of 3.1 m. The packing factor of dipoles in the arcs is 81.8% while the ratio of quadrupoles over the ring is about 10%. Fig. 4.12 [47] shows the oscillations of the optics functions along the FODO lattice of the FCC-ee arcs. For these studies, the realistic shape of the vacuum chamber shown in Fig. 4.13 [48] has been used. The beam pipe is modelled as a circular pipe with 35 mm radius and two rectangular antechambers on both sides, as the one of SuperKEKB [49]. These antechambers are needed to reduce the effect of photoelectrons and the SR power density on the pipe walls, by installing SR absorbers on one

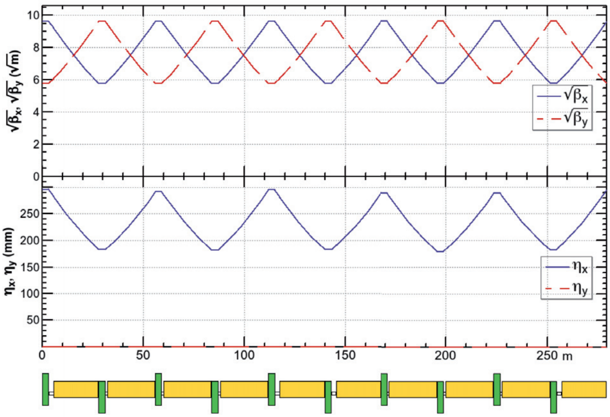

Figure 4.12: Beta functions and dispersion functions along the cells of the FCC-ee arc FODO lattice.

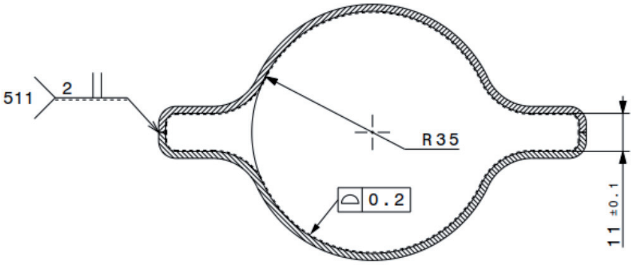

Figure 4.13: Transverse profile of the FCC-ee vacuum chamber.

side and slots for vacuum pumping just in front of the absorbers, thus efficiently capturing the SR and the molecule desorption. The secondary emission model used in these simulations is described in [38] and in Section 3.2.2. According to high order mode power loss computations [50], bunch spacings of 10 ns and 17.5 ns are not acceptable for the present cavity geometry and filling schemes with at least 100 RF buckets between the first bunches of consecutive trains are preferred. Therefore, for these studies 4 trains of 80 bunches interleaved with 25 empty buckets have been assumed by considering different bunch spacings of 2.5 ns, 5 ns and 15 ns. The nominal bunch intensity of $1.7 \cdot 10^{11}$ e^+/bunch has been used for all simulations. The magnetic parameters of each element are shown in Table 2 while the bunch parameters used for simulations are listed in Table 1.

The EC build up in the arc dipoles has been simulated by scanning the SEY for different bunch spacings and by assuming an initial uniform electron distribution in the vacuum chamber of $10^9 e^-/m$. Contrary to the residual gas ionization and the photoemission due to SR that reflect physical mechanisms of creation of primary electrons, this option is used to model the fact that in multi-turn operation electrons do survive in the

Element	**Length (m)**	**Magnetic field**
Dipole	21.94/23.44	0.01415 T
Quadrupole	3.1	± 5.65 T/m
Drift	-	-

Table 2: Arc magnet parameters used for build up simulations at 45.6 GeV.

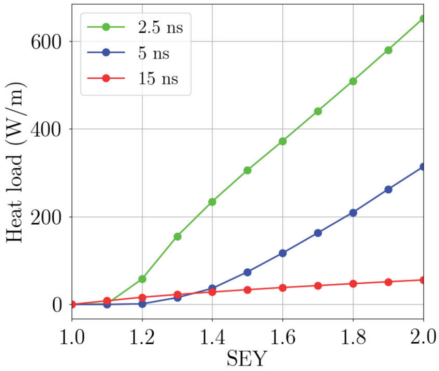

Figure 4.14: Heat load in the FCC-ee arc dipoles as a function of the SEY parameter.

machine even for long abort gaps. Therefore, when the beam arrives, the chamber is already filled with a certain basic level of electron density. This initial uniform electron distribution can affect only the initial transient of the build up process, the dominant steady state density being determined by beam parameters, chamber geometry and SEY. The initial transient has been therefore disregarded in the following computation of the heat load. Fig. 4.14 compares the EC induced heat load as a function of SEY for 2.5 ns, 5 ns and 15 ns bunch spacings. The heat load has been calculated as the energy of electrons impacting the pipe walls over the simulated time range rescaled to the total beam intensity.

Fig. 4.15 shows a typical EC build up inside a bending magnet: the total number of electrons per unit length in the chamber of the FCC-ee arc dipoles as a function of time has been evaluated for different SEY and bunch spacings. As can be seen, the saturation level is larger for decreasing bunch spacing and increasing SEY.

The multipacting threshold, defined as the highest SEY without EC multipacting, can be localized at SEY $\simeq 1.1$ for both 2.5 ns and 5 ns beams and at SEY $\simeq 1.0$ for the 15 ns beam. As mentioned before, the initial transient visible only on the first simulated train has been excluded in the heat load computation, because it depends on the initial value of the electron density. Only trains where the electron distribution inside the chamber reaches a dynamic steady state have been considered.

Figure 4.16 shows the energy spectrum of the electrons impacting the pipe

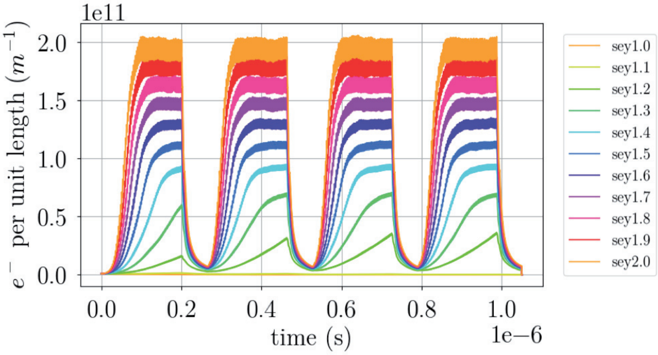

(a) 2.5 ns beam.

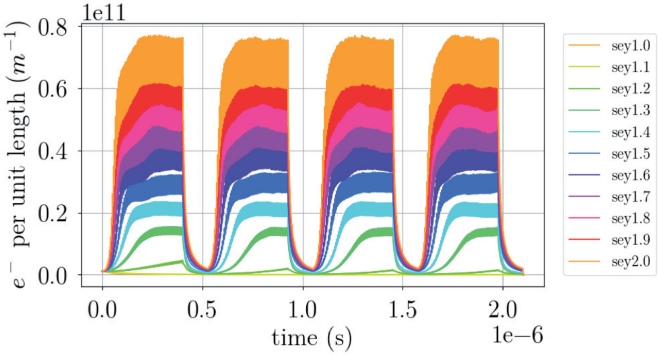

(b) 5 ns beam.

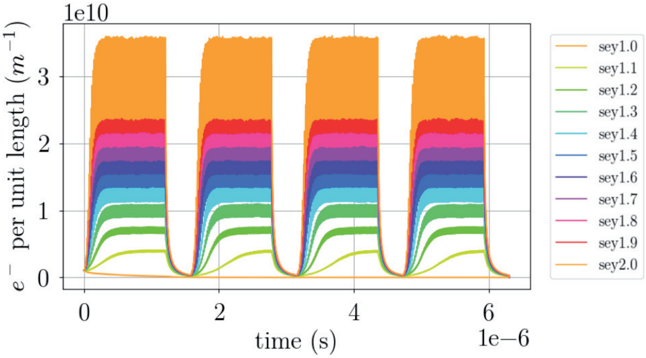

(c) 15 ns beam.

Figure 4.15: Evolution of the total number of electrons in the beam chamber of the FCC-ee arc dipoles as a function of time, for 2.5 ns (a), 5 ns (b) and 15 ns (c) bunch spacings.

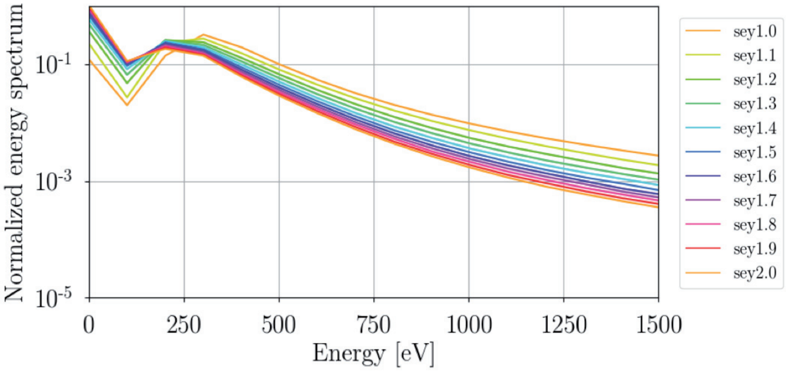

Figure 4.16: Energy spectrum of the electrons impacting the wall in a FCC-ee arc dipole magnet.

walls: the bump around 250 eV corresponds to the energy of electrons involved in multipacting.
The distribution of electrons in the chamber is shown in Fig. 4.17, where the different snapshots refer to different time steps during and after the bunch passage. Unlike the LHC dipoles where electrons are trapped around the field lines showing vertical stripes lateral to the beam and around the beam location, FCC-ee dipoles are characterized by an electron distribution spread out quite uniformly inside the vacuum chamber. This can be explained by the very small magnetic field B = 14 mT, responsible of a larger cyclotron radius of the helicoidal trajectory of the electron around the field lines [38]. These distributions are important to determine where the low SEY coating is required: in the case of dipoles, the coating should cover the full chamber.

As for the dipoles, the EC build up has been simulated in the arc quadrupoles and field-free regions for different SEY and bunch spacings. Figure 4.18 shows the EC induced heat load in the chamber of these components as a function of SEY for 2.5 ns, 5 ns and 15 ns bunch spacings. The highest multipacting thresholds correspond to the 2.5 ns beam and are localized at SEY $\simeq$ 1.2 in the quadrupoles and at SEY $\simeq$ 1.8 in the drifts. These values decrease to 1.0 and 1.3, respectively, for the 5 ns beam. For the 15 ns beam a SEY $\leq$ 1.0 is needed to suppress the EC multipacting in the quadrupoles while drifts requires a SEY $\simeq$ 1.0.

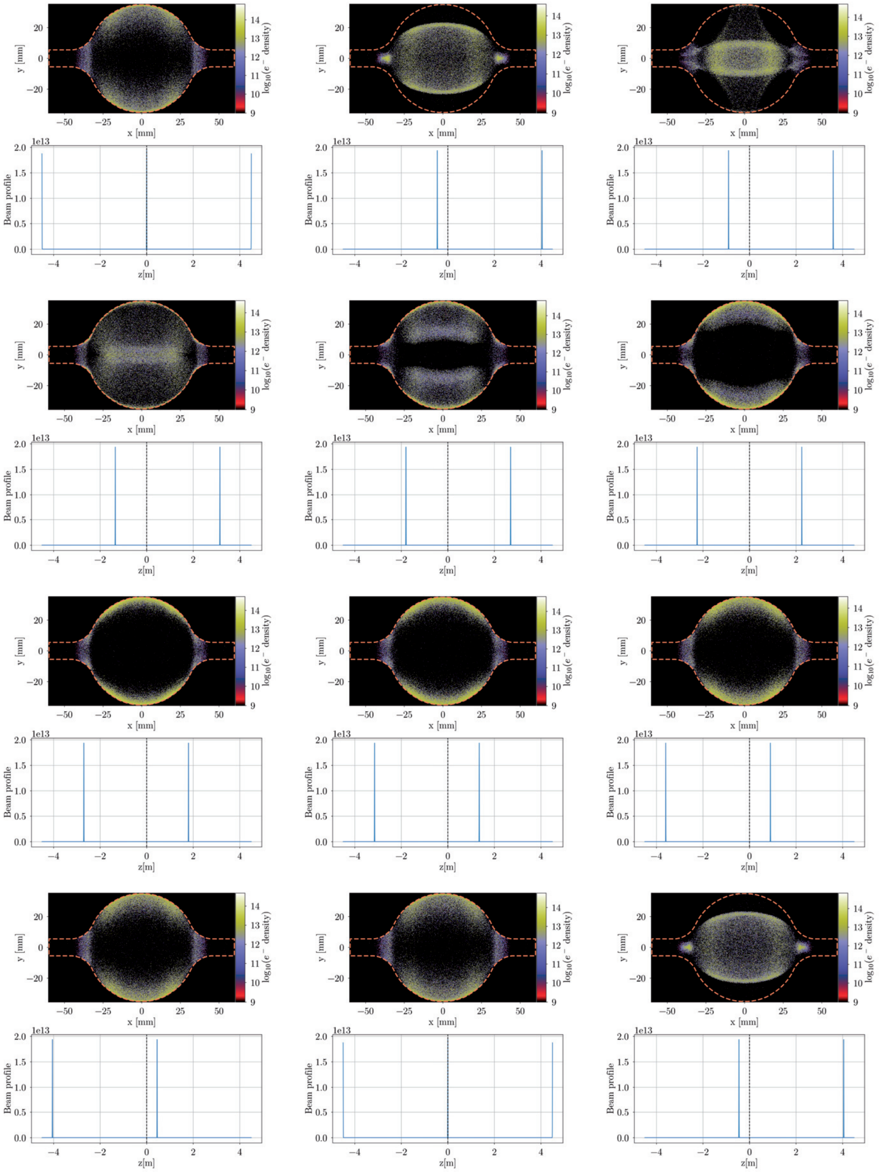

Figure 4.17: Different snapshots of the electron distribution in the FCC-ee arc dipoles during the passage of two consecutive bunches, at saturation level. The simulation is performed at low energy, with 15 ns bunch spacing, for SEY = 1.3.

Figure 4.19 shows the evolution of the total number of electrons per unit length in the chamber of the FCC-ee arc quadrupoles and drifts as a function

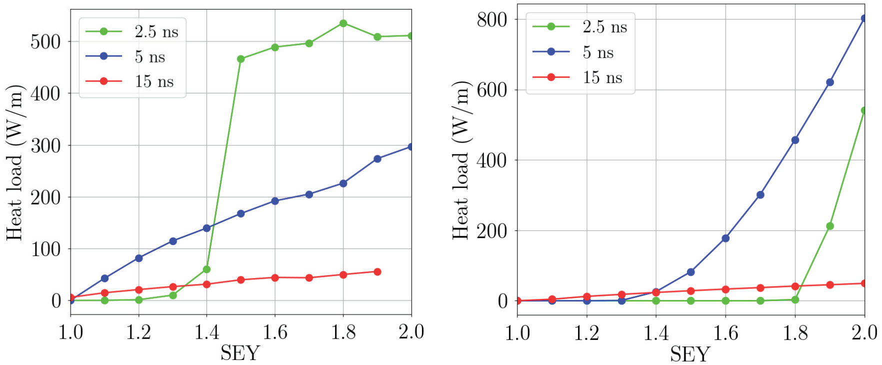

Figure 4.18: Heat load in the FCC-ee arc quadrupoles (left side) and drifts (right side) as a function of the SEY parameter.

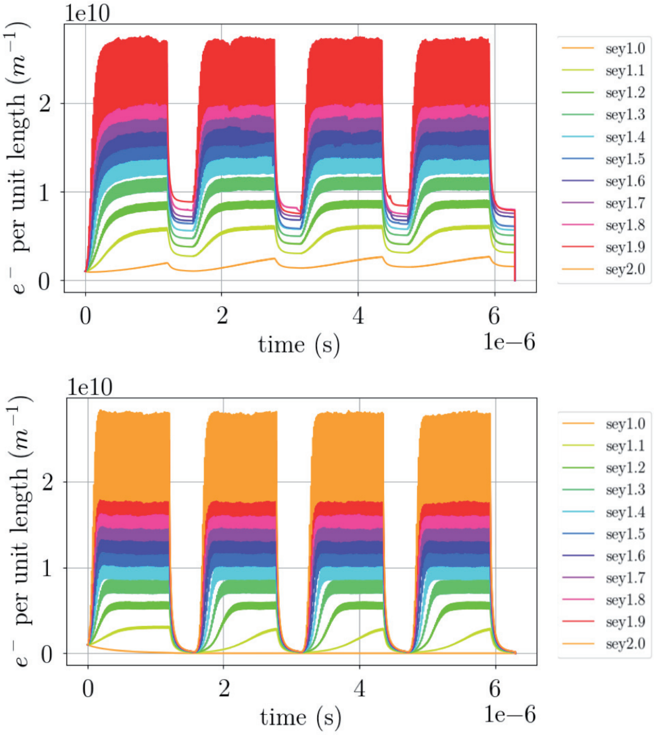

Figure 4.19: Evolution of the total number of electrons in the beam chamber of the FCC-ee arc quadrupoles (top) and drifts (bottom) as a function of time, for 15 ns bunch spacing.

Element	**2.5 ns**	**5 ns**	**15 ns**
Dipole	1.1	1.1	1.0
Quadrupole	1.2	1.0	<1.0
Drift	1.8	1.3	1.0

Table 3: Threshold SEY for multipacting for all the arc components.

of time in the case of 15 ns bunch spacing, while Figs. 4.20, 4.21 show the distribution of electrons in the chamber of these components: drifts require a low SEY coating at top and bottom of the chamber while in quadrupoles the multipacting is at 45° to the horizontal plane. Unlike the LHC case, the electron distribution is not concentrated along the pole-to-pole lines. Moreover, since there are very high electron densities in some regions of the vacuum chamber, the resolution of the simulation code could not ensure a correct evaluation of the electron density in the central region and further investigation by means of instability simulations is needed.

Table 3 summarizes the multipacting threshold for each arc component and beam: the highest thresholds of EC multipacting are given by the 2.5 ns beam but above the threshold the heat load is reduced by a factor of 10 in the case of 15 ns beam. It is important to note that the multipacting threshold is higher for shorter bunch spacing. This result should not be surprising since there are two extreme cases where multipacting does not occur:

- in the case of continuous beam (or very small bunch spacing) where electrons remain trapped around the beam: when electrons are attracted and accelerated by a bunch, the next bunch could be closer enough to attract these electrons again before they reach the pipe walls, thus reducing the secondary emission.
- in the case of very large bunch spacing: electrons with low energy generated after the passage of a bunch are absorbed by the pipe walls before the arrival of the next bunch.

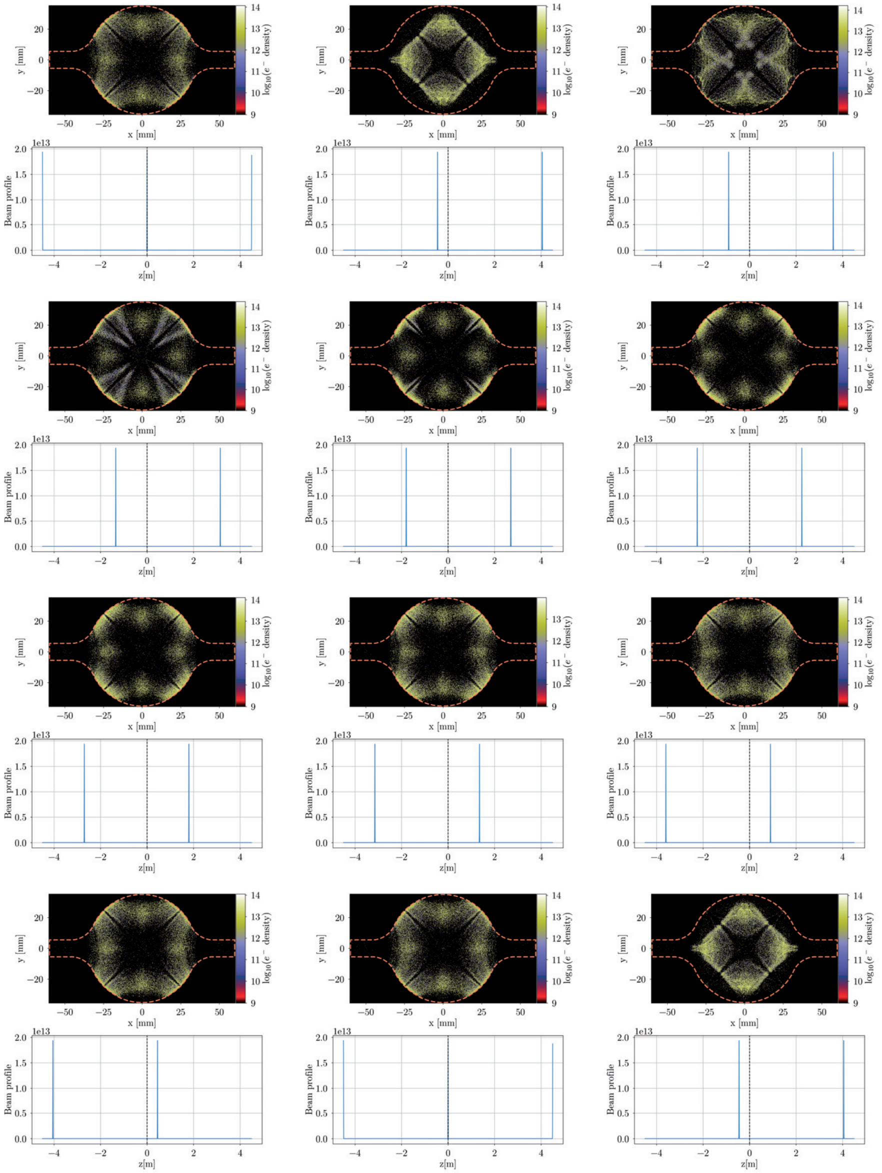

Figure 4.20: Different snapshots of the electron distribution in the FCC-ee arc quadrupoles during the passage of two consecutive bunches, at saturation level. The simulation is performed at low energy, with 15 ns bunch spacing, for SEY = 1.3.

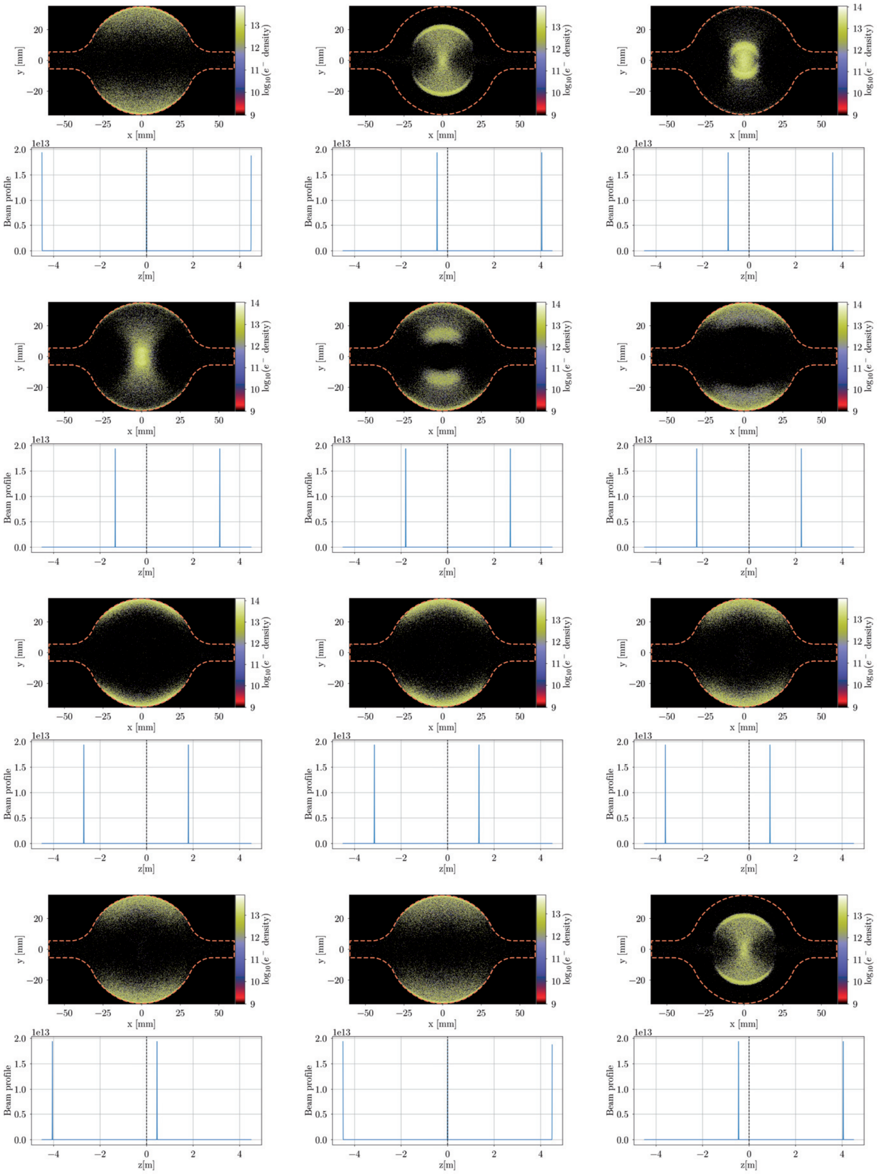

Figure 4.21: Different snapshots of the electron distribution in the FCC-ee arc drifts during the passage of two consecutive bunches, at saturation level. The simulation is performed at low energy, with 15 ns bunch spacing, for SEY = 1.3.

4.4 PHOTOEMISSION DUE TO SYNCHROTRON RADIATION

In the FCC-ee, due to the high SR, photoelectrons generated by photoemission are the main source of primary electrons.

At 45.6 GeV, the number of photons emitted per positron per unit length given by Eq. 41 is equal to $N_\gamma = 0.085\, ph/e^+m$, a value three times higher than LHC and twice FCC-hh at collision, and the critical photon energy (see Eq. 42) is $E_c \simeq 19$ keV. As described in [38], the photoemission seeding is modelled in PyECLOUD through photoelectron yield Y and photon reflectivity R. These two parameters depend both on material and SR properties. Dedicated measurements were performed between 1998 and 2004 at the LHC to study the photoemission properties of the beam screens [51–54] while in the case of FCC-ee with $E_c \simeq 19$ keV no experimental data exist. For this reason, a photoelectron yield $Y = 0.02$ (similarly to the one considered for SuperKEKB studies [55]) and a reflectivity in the range R = [30%, 80%] have been assumed in build up simulations.

Results for arc dipoles, quadrupoles and drifts in case of 15 ns bunch spacing are presented in Fig. 4.22, for different values of reflectivity and photoelectrons, obtained by assuming that 50%, 75% and 95% of photons are absorbed by the SR absorbers installed in the rectangular antechambers of the beam pipe.

One can observe that for all the components the photoemission seeding does not significantly change the results of the build up simulation obtained by uniform seeding and presented in the previous section. In other words, the heat load is not affected by photoelectrons: this means that after an initial transient the build up and maintenance of the EC is mainly determined by the secondary emission, while the dependence on the photoemission parameters is marginal.

4.5 SIMULATION STUDIES FOR THE FCC-EE IR COMPONENTS

Build up simulations have also been performed for the final focusing quadrupoles in the IR, whose magnetic parameters are summarised in Table 4. For these components, the beam pipe is circular with 15 mm radius for the QC1 quadrupole and 20 mm radius for the QC2 quadrupole.

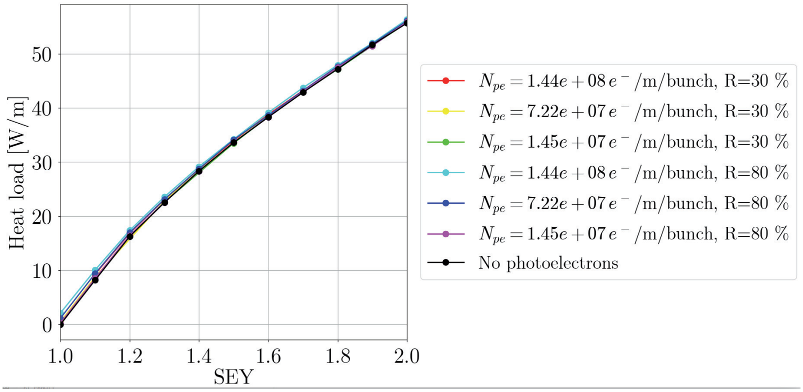

(a) Dipole

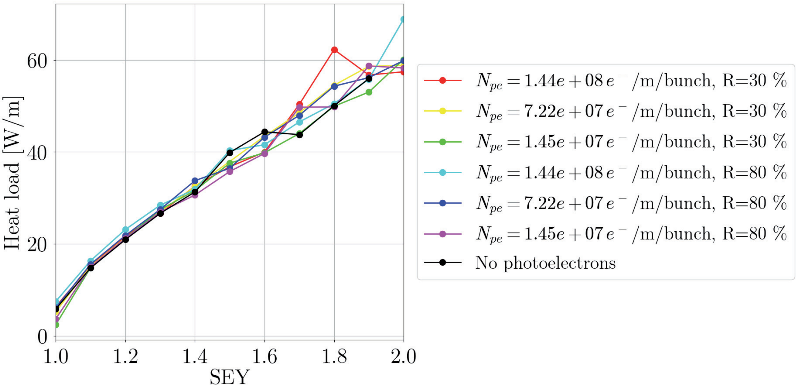

(b) Quadrupole

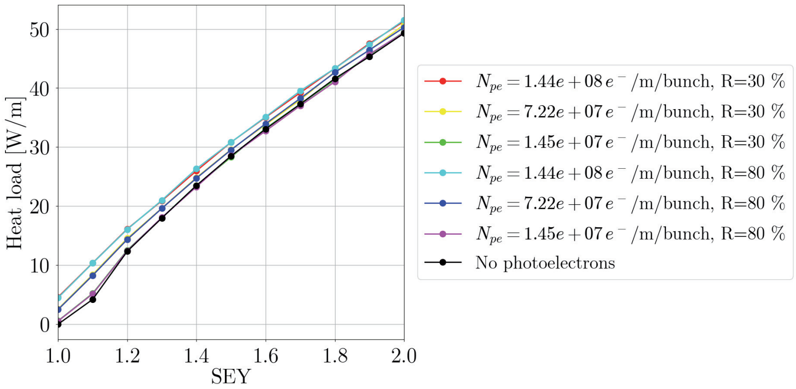

(c) Drift

Figure 4.22: Heat load as a function of SEY for arc dipoles, quadrupoles and drifts in case of no photoelectrons and different values of photoelectrons and reflectivity, for a bunch spacing of 15 ns.

Element	Length (m)	Magnetic field (T/m)
QC1L1	1.2	-96.3
QC1L2	1.0	50.3
QC1L3	1.0	9.8
QC2L1	1.25	6.7
QC2L2	1.25	3.2

Table 4: IR Magnet parameters used for build up simulations at 45.6 GeV.

Figure 4.23 [47] shows the beam optics around the IP used in simulations. Also in this case, the EC build up has been simulated by scanning the SEY for different bunch spacing and by assuming an initial uniform electron distribution in the vacuum chamber of $10^9 e^- / m$, with the same filling pattern and bunch parameters assumed in the arcs.

Figure 4.24 shows the EC induced heat load in the chamber of the IR quadrupoles as a function of SEY for 2.5 ns, 5 ns and 15 ns bunch spacings, while the multipacting threshold for each component and beam has been reported in Table 5. These results indicate that in the IR the highest thresholds and lower heat load are given by the 15 ns beam. In particular, a SEY $\leq$ 1.2 is needed to run the IR without multipacting.

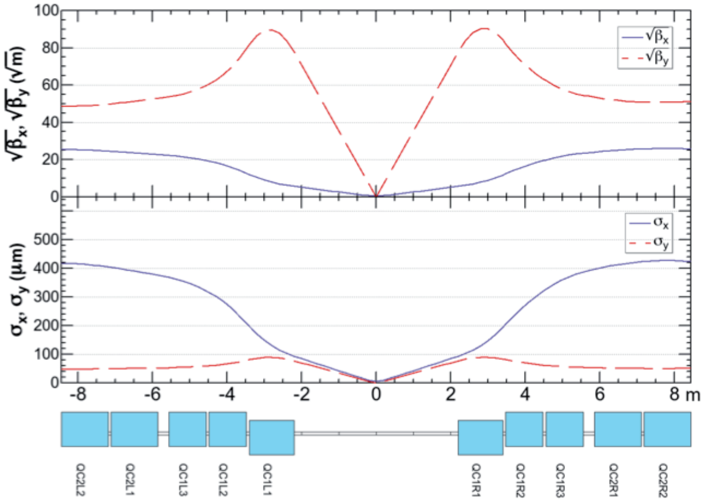

Figure 4.23: Beta functions and dispersion functions around the IP.

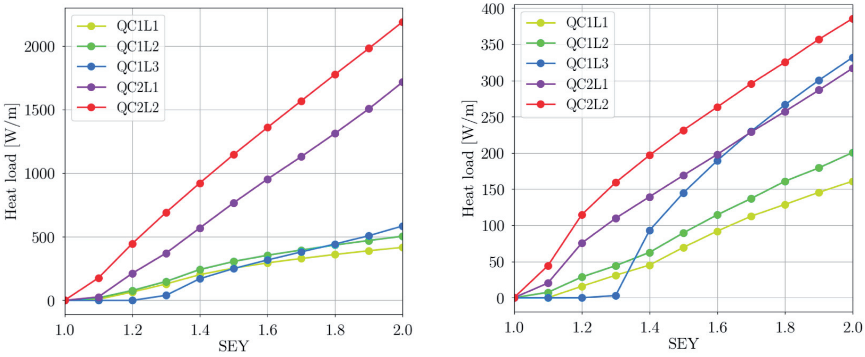

(a) 2.5 ns beam.

(b) 5 ns beam.

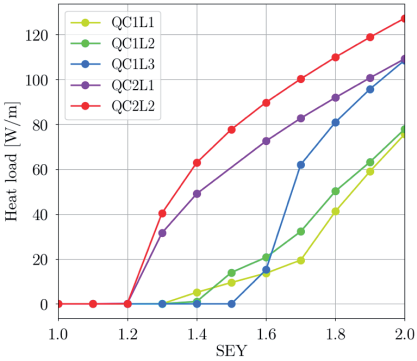

(c) 15 ns beam.

Figure 4.24: Heat load in the FCC-ee IR quadrupoles as a function of the SEY parameter for 2.5 ns (a), 5 ns (b) and 15 ns (c) bunch spacings.

Element	**2.5 ns**	**5 ns**	**15 ns**
QC1L1	1.0	1.1	1.3
QC1L2	1.0	1.0	1.4
QC1L3	1.2	1.3	1.5
QC2L1	1.0	1.0	1.2
QC2L2	1.0	1.0	1.2

Table 5: Threshold SEY for multipacting for all the IR components.

4.6 ELECTRON DENSITY THRESHOLD FOR TRANSVERSE INSTABILITY

EC single bunch head tail instability has been analyzed and observed in several machines [56, 57]. This instability is produced by the interaction

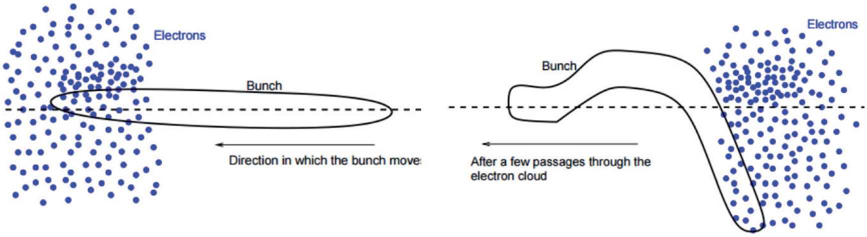
Electrons
Bunch
Direction in which the bunch move
Bunch
Electrons
After a few passages through the electron cloud

Figure 4.25: Schematic of the EC induced single bunch instability.

of the bunch with the EC (see Fig. 4.25 [56]): if the head of the bunch is slightly displaced from the beam axis when entering the EC, electrons will be attracted towards the head centroid position and there will be an EC formation in this region that will attract the following particles of the bunch. After a few passes through the EC, this will result in a strong deflection of the bunch tail. In this case, the EC acts as a short range wake field with frequency

$$\omega_e = \sqrt{\frac{\lambda_p r_e c^2}{\sigma_y(\sigma_x + \sigma_y)}} \tag{67}$$

where $\lambda_p = \frac{N_p}{\sqrt{2\pi}\sigma_z}$ is the positron line density with N_p bunch population and σ_z bunch length, r_e is the classical electron radius and $\sigma_{x,y}$ are the transverse beam dimensions.
The threshold density for the instability is given by [58]

$$\rho_{th} = \frac{2\gamma Q_s \omega_e \sigma_z / c}{\sqrt{3} K Q r_e \beta_y C} \tag{68}$$

where Q_s is the synchrotron tune, C the machine circumference, $K = \omega_e \sigma_z / c$, $Q = min(7, \frac{\omega_e \sigma_z}{c})$ and $\beta_y = \frac{C}{2\pi Q_y}$.
Considering the baseline beam parameters of Table 1, the corresponding electron density threshold for the transverse instability at low energy is about $2.29 \cdot 10^{10}/m^3$. Such a low threshold can create potential problems for the collider operation and this issue requires further investigation by means of numerical simulations. Therefore, it is important to minimise the SEY in the entire ring by applying a low SEY coating, paying particular attention to the resistive wall impedance seen by the beam.

5

RESISTIVE WALL WAKEFIELDS AND IMPEDANCES

When the beam passes through the vacuum chamber, it induces image currents on the pipe walls. If the beam pipe walls have a finite conductivity, these currents extend behind the position of the charges, creating electromagnetic fields which can act on the trailing particles and perturb their motion by increasing the amplitude of their oscillations. This kind of instability due to the so called resistive wall (RW) wakefields can occurr in both longitudinal [59] and transverse [60] directions. In a metal with conductivity σ_c and permeability μ, the skin depth is equal to

$$\delta_s = \sqrt{\frac{2}{\sigma_c \omega \mu}} \tag{69}$$

Figure 5.1 shows the skin depth of copper as a function of frequency. In the FCC-ee, for a bunch length of 3.5 mm corresponding to the Z resonance the frequency of interest does not exceed 100 GHz. At this frequency the skin depth of copper is about 0.2 μm and it is higher for lower frequencies. For a circular beam pipe with radius b and a single layer of conductivity σ_c and infinite thickness, the exact expressions of the longitudinal monopolar

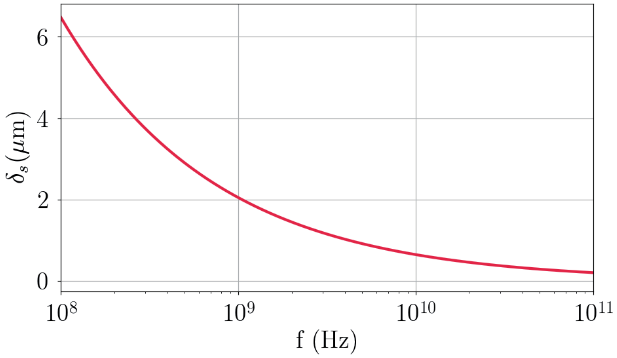

Figure 5.1: Skin depth as a function of frequency for copper.

(m = 0) and transverse dipolar (m = 1) coupling impedances can be found in [61]. In the following frequency range:

$$\frac{\chi c}{b} \ll \omega \ll \frac{c\chi^{-1/3}}{b} \tag{70}$$

with $\chi = 1/\left(Z_0\sigma_c b\right)$, c the speed of light and Z_0 the vacuum impedance, the exact expressions of the impedances can be written respectively as:

$$\frac{Z_{||}\left(\omega\right)}{C} = \frac{Z_0 c}{\pi}\frac{1}{\left[1 + i\mathrm{sgn}\left(\omega\right)\right] 2bc\sqrt{\frac{\sigma_c Z_0 c}{2|\omega|}}} \tag{71}$$

$$\frac{Z_{\perp}\left(\omega\right)}{C} = \frac{Z_0 c^2}{\pi}\frac{2}{\left[\mathrm{sgn}\left(\omega\right) + i\right] b^3 c\sqrt{2\sigma_c Z_0 c\left|\omega\right|}} \tag{72}$$

where C is the machine circumference. For the lepton collider with a 35 mm radius beam pipe made of copper ($\sigma_{Cu} \simeq 5.9 \cdot 10^7 S/m$), the frequency range of validity of Eqs. 71 and 72 given by Eq. 70 is very wide (1 Hz $\ll f \ll$ 1 THz) and fully satisfied by a bunch length in the order of mm, as that of FCC-ee. From these equations it is clear that the possibilities to optimize the RW impedance are more limited, contrary to other machine devices that can be optimized from the impedance point of view by using for example new designs, smooth transitions and high order mode damping systems [62]. The only two parameters that can be changed are the conductivity of the vacuum chamber and the beam pipe radius.

Regarding this last parameter, from Eqs. 71 and 72 one can observe that the longitudinal impedance is inversely proportional to the beam pipe radius b while the transverse impedance to the third power of b. This scaling can be used to optimize the pipe geometry, by finding a good compromise between RW impedance and magnet power requirements. In fact, by reducing the pipe radius it is possible to reduce the power required for magnets, but this would increase the coupling impedances, thus reducing the thresholds of the instabilities. Based on these considerations, a radius b = 35 mm has been chosen for the lepton collider.

Moreover, as discussed in the previous chapter, a low SEY coating with a lower conductivity than copper is foreseen to mitigate the EC build up in the machine. The presence of this layer will affect the RW impedance and its effects on beam dynamics, as will be illustrated in Sections 5.2 and 5.3 of this chapter.

5.1 THE IMPORTANCE OF THE RESISTIVE WALL IMPEDANCE IN FCC-EE

The main difference of FCC-ee with respect to other colliders is the large circumference of 97.75 km. Since the RW impedance is proportional to the machine length, it is not surprising that in the lepton collider its contribution to the total broad band impedance is larger compared to the other machine components, becoming critical for the microwave instability, as will be illustrated in Section 5.3.1.

This property in fact is not true for other machine devices like bellows, RF cavities, etc. For example, the number of bellows in an accelerator is not proportional to the machine length: the total number of bellows in KEKB, whose circumference is 3 km, is about 1000 while FCC-ee needs 8000 bellows, despite a circumference about 30 times larger.

In order to highlight the importance of the RW impedance in FCC-ee with respect to other colliders, and also as reference for the beam dynamics studies presented in Section 5.3, the beam parameters summarized in Table 1 have been used to evaluate the effects of the RW wakefields on beam dynamics.

Consider first the longitudinal plane. It is strongly believed and supported that the microwave instability mechanism relies on the coupling among azimuthal and/or radial intrabunch modes [63]. In the case of azimuthal modes, the coupling is strong and the frequencies of the modes have to shift by an amount comparable to the synchrotron frequency ω_s, while in the case of radial mode coupling the frequency shifts are small and the instability is weak. An important peculiarity of the lepton collider is the very low momentum compaction (see Table 1), due to the low dispersion and to the large machine circumference, that can affect the microwave instability in combination with the energy spread and the short bunch length. Accordingly to the Boussard criterion [64] that can be used as a first rough approximation to obtain a scaling of the instability threshold with the beam parameters, on the Z resonance the maximum allowed longitudinal broad-band impedance to avoid the instability, evaluated at the n^{th} harmonic of the revolution frequency ω_0, is equal to

$$\frac{Z_{\parallel}(n\omega_0)}{n} \leq \frac{(2\pi)^{\frac{3}{2}}E_0}{ce^2}\alpha_c\frac{\sigma_z}{N_p}\sigma_{dp}^2 \simeq 0.66\,m\Omega \tag{73}$$

This value is quite demanding, also for a very large machine. Therefore, in order to operate at nominal current below the microwave instability regime, a careful design of the different devices is needed, with the aim of minimising their coupling impedance and ensuring beam stability during operation.

Also in the transverse plane the RW impedance is responsible of a quite low single bunch instability threshold. As will be seen in Section 5.3.2, this instability occurs when there is a coupling between azimuthal intrabunch modes [27]. The analytic transverse mode coupling instability (TMCI) threshold is given by the well known Sacherer formula [65,66]:

$$N_{th} = \frac{4\pi\frac{E_0}{e}\tau_b Q_s}{e\beta_{av}Im[Z_m^{eff}]} \tag{74}$$

where m is the mode number, $\tau_b = \frac{4\sigma_z}{c}$ is the full bunch length in s, $\beta_{av} = \frac{C}{2\pi Q_\beta}$ is the average beta of the machine and Z^{eff} is the effective transverse impedance computed as [67]

$$Z^{eff} = \frac{\sum_{p=-\infty}^{+\infty} Z_\perp(\omega_p)h_m(\omega_p - \omega_\xi)}{\sum_{p=-\infty}^{+\infty} h_m(\omega_p - \omega_\xi)} \tag{75}$$

i.e., the transverse impedance $Z_\perp$ averaged over the bunch power spectrum of azimuthal mode m

$$h_m(\omega) = \left(\frac{\omega\sigma_z}{c}\right)^{2|m|} e^{-\frac{\omega^2\sigma_z^2}{c^2}} \tag{76}$$

In Eq. 75, the bunch spectrum is discrete at lines $\omega_p - \omega_\xi$ where

$$\omega_\xi = \omega_0\frac{\xi}{\eta} \tag{77}$$

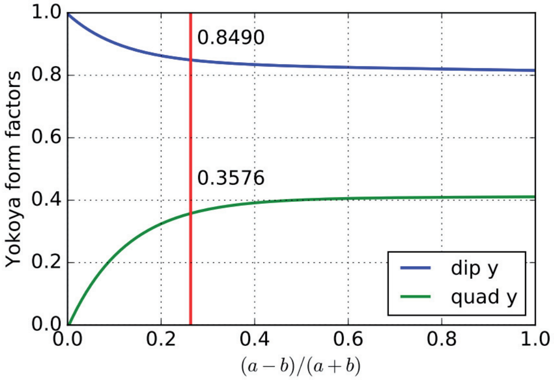

Figure 5.2: Yokoya form factors as a function of the major (a) and minor (b) semi-axes.

is the chromatic angular frequency which depends on the revolution frequency ω_0, the chromaticity ξ and the slippage factor η, and

$$\omega_p = (p + \Delta Q)\omega_0 + m\omega_s \tag{78}$$

where ΔQ is the fractional part of the betatron tune and ω_s is the synchrotron frequency. The maximum allowed effective transverse impedance to avoid the instability can be obtained from Eq. 74 and in the FCC-ee on the Z resonance it is about 425 kΩ/m. By considering a Gaussian bunch of nominal length and the transverse impedance due to RW of Section 5.3 for a copper pipe with 35 mm radius and without coating, the effective transverse impedance is about 155 kΩ/m, only a factor of 2.7 below the threshold. This result here obtained by using approximate expressions will be confirmed in Section 5.3.2 with more accurate simulations.

Before concluding this section, it is important to make a final remark about the choice of the beam pipe shape. In the initial phase of the design of the lepton collider, an elliptical vacuum chamber with semi-axes 60x35 mm was considered for allowing the installation of SR absorbers on one side of the beam pipe along the major semi-axis. Compared to a round pipe, an elliptical chamber gives a reduced dipolar impedance in the horizontal plane but it produces an additional quadrupolar transverse impedance (which is zero for a round pipe). Figure 5.2 shows the Yokoya form factors [68], representing the ratio between the impedance of an elliptic pipe and the impedance of a circular pipe, as a function of $q = \frac{a-b}{a+b}$, where a and b represent the major and minor semi-axes of the ellipse, respectively. For the elliptic chamber initially proposed for FCC-ee, these factors give a reduction of the dipolar impedance of about 15% while there is an increase of the quadrupolar impedance of about 36%. This quadrupolar wake component is responsible for a large incoherent betatron tune shift [69]. As a rough estimation of the possible effect of the elliptic chamber, the tune shift for a rectangular vacuum chamber inside dipole magnets is given by [70,71]

$$\frac{dQ_{x,y}}{dI} = \pm\left(\frac{\pi r}{48Q_{x,y}}\right)\left(\frac{Z_0}{E_0/e}\right)\left(\frac{R}{b}\right)^2\left(\frac{L}{C}\right), \qquad r = \frac{1}{2} + \frac{b^2}{d^2} \tag{79}$$

where $Q_{x,y}$ is the transverse tune, R the radius of the machine, b and d the half height and half width of the vacuum chamber, E_0 the nominal energy and L/C the ring fraction with the rectangular chamber (dipoles). This equation predicted very well the tune shifts observed in the high current lepton factory PEP-II [70]. By assuming dipole vacuum chambers with a cross section of $2a \times 2b = 120 \times 70$ mm occupying a fraction L/C = 0.82 of the ring, the tune shift is about $\pm 0.27I$. This means that during the beam injection and up to the nominal current of 1.39 A, the tune variation is about 38%. In order to cope with such a big tune change, additional feedback systems would be necessary to keep the tune constant as required by the beam-beam interaction, dynamic aperture considerations and other beam dynamics issues. These studies led to the choice of a circular pipe that allows overcoming this issue. Actually the beam pipe of FCC-ee is not totally round: as already illustrated in Chapter 4, two rectangular antechambers have been designed on both sides of the pipe for SR absorbers installation and pumping purposes.

5.2 RESISTIVE WALL IMPEDANCE WITH COATING

In the proposed lepton collider, a coating of the copper surface is required to reduce the SEY of the beam pipe walls for EC mitigation. The presence of this film makes the surface resistance of the beam pipe higher than pure copper and the RW effect is more pronounced. Moreover, the uncertainty on the coating conductivity varying with frequency may give inaccurate results of instability thresholds. This section will show that in the case of FCC-ee the dominant effect on beam dynamics mainly comes from the thickness of the coating while its conductivity only plays a marginal role. Therefore, the best way to decrease the RW contribution is to reduce the coating thickness. In order to evaluate the impedance of a two-layer beam pipe, let us consider a good conductor with $\sigma_c \gg \omega\varepsilon$, where ε is the material dielectric constant. By assuming that for FCC-ee the frequency of interest for the coupling impedance does not exceed 100 GHz, the conductivity of the materials should be much bigger than 10 S/m, condition verified for copper and in general for all the materials typically used in accelerators. Moreover, in the particular case of FCC-ee on the Z resonance, if $\omega b/(\gamma\beta c) \simeq 8 \times 10^{-4} \ll 1$, the longitudinal and transverse impedances of a two-layer circular beam pipe [72] can be written in a simple form as

$$\frac{Z_{||}(\omega)}{C} = \frac{Z_0\omega}{4\pi cb}\left\{\left[\mathrm{sgn}(\omega) - i\right]\delta_1 \frac{\alpha \tanh\left[\frac{1-i\mathrm{sgn}(\omega)}{\delta_1}\Delta\right] + 1}{\alpha + \tanh\left[\frac{1-i\mathrm{sgn}(\omega)}{\delta_1}\Delta\right]}\right\} \tag{80}$$

and

$$\frac{Z_{\perp}(\omega)}{C} = \frac{Z_0}{2\pi b^3}\left[1 - i\mathrm{sgn}(\omega)\right]\delta_1 \frac{\alpha \tanh\left[\frac{1-i\mathrm{sgn}(\omega)}{\delta_1}\Delta\right] + 1}{\alpha + \tanh\left[\frac{1-i\mathrm{sgn}(\omega)}{\delta_1}\Delta\right]} \tag{81}$$

where δ_1 and Δ are the skin depth and the thickness of the coating, respectively, and for a good conductor $\alpha \simeq \delta_1/\delta_2$, with δ_2 the skin depth of the substrate, which is supposed to be of infinite thickness.

If the skin depth of the coating material is much bigger than its thickness, i.e. $\delta_1 \gg \Delta$, then the longitudinal and transverse impedances can be written as

$$\begin{aligned}\frac{Z_{||}(\omega)}{C} &= \frac{Z_0\omega}{4\pi cb}\frac{\left[\mathrm{sgn}(\omega) - i\right]\delta_2 - 2i\Delta}{1 + \frac{\delta_2\Delta[1-i\mathrm{sgn}(\omega)]}{\delta_1^2}} \simeq \\ &\simeq \frac{Z_0\omega}{4\pi cb}\left\{\left[\mathrm{sgn}(\omega) - i\right]\delta_2 - 2i\Delta\left(1 - \frac{\sigma_1}{\sigma_2}\right)\right\}\end{aligned} \tag{82}$$

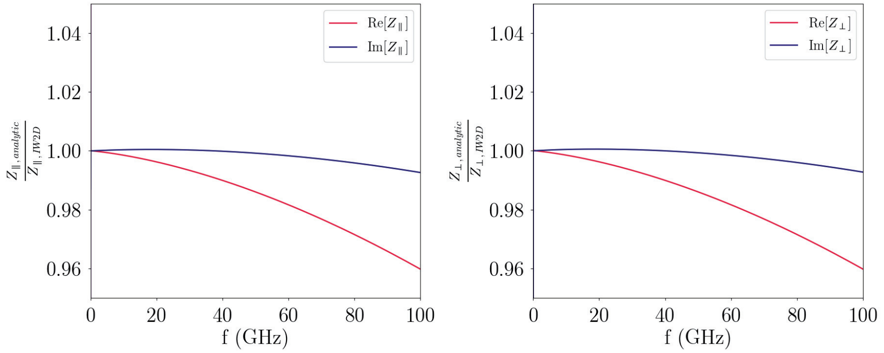

Figure 5.3: Ratio between the analytic impedances given by Eqs. 82 and 83 and the corresponding impedances obtained from ImpedanceWake2D, in the longitudinal (left side) and transverse (right side) planes. The red and blue curves represent the real part and the imaginary part of the impedance, respectively.

and

$$\begin{aligned}\frac{Z_\perp(\omega)}{C} &= \frac{Z_0}{2\pi b^3}\left[1-i\mathrm{sgn}(\omega)\right]\delta_1\frac{\left[1-i\mathrm{sgn}(\omega)\right]\Delta+\delta_2}{1+\frac{\delta_2\Delta[1-i\mathrm{sgn}(\omega)]}{\delta_1^2}} \simeq \\ &\simeq \frac{Z_0}{2\pi b^3}\left\{\left[1-i\mathrm{sgn}(\omega)\right]\delta_2 - 2i\Delta\mathrm{sgn}(\omega)\left(1-\frac{\sigma_1}{\sigma_2}\right)\right\}\end{aligned} \tag{83}$$

where σ_1 and σ_2 are the conductivities of coating and substrate, respectively. These two equations have been obtained by ignoring in the last passage the second order terms in the ratio Δ/δ_1.

In order to demonstrate that all the assumptions made to derive these two equations are valid in the case of FCC-ee, Fig. 5.3 shows the ratio in the longitudinal and transverse case between the simplified expressions given by Eqs. 82 and 83 and the exact solutions obtained from the ImpedanceWake2D code [73, 74] for a copper pipe of 35 mm radius coated with a layer of 100 nm thickness and conductivity 10^6 S/m (corresponding to the NEG films used for beam dynamics studies presented in Section 5.3). By considering these parameters and the highest frequency of 100 GHz (corresponding to the smallest skin depth), the ratio Δ/δ_1 is about 0.06. From these plots, it is evident that in the worst case at 100 GHz the difference between impedances is only 5% for the real part, while the imaginary part is essentially the same. These results show that the two expressions (82) and

(83) represent a very good approximation of the impedances of a two-layer beam pipe when the coating thickness is much lower than its skin depth.
Regarding Eqs. 82 and 83, one further important remark needs to be made. The first term in the curly brackets on the right side of these equations represents the impedance of a single layer beam pipe given by Eqs. 71 and 72. Therefore, the longitudinal and transverse impedances of a two-layer beam pipe can be read as the sum of two terms, one representing the impedance of a single layer pipe and a second term representing an inductive perturbation proportional to the thickness of the coating. The same conclusion has also been obtained in [75].
Moreover, if the conductivity of the coating is much smaller than the conductivity of the substrate, i.e. if $\sigma_1/\sigma_2 \ll 1$, the ratio σ_1/σ_2 in the second term can be neglected and the perturbation becomes independent on the coating conductivity. This condition is verified in general for all the coatings typically used in accelerators for EC suppression and in particular for FCC-ee, also taking into account the variation of the NEG resistivity with frequency [76].
This important result shows that if the coating can be reduced to a very low value such that up to the maximum frequency of interest the skin depth remains much higher than its thickness, then the material conductivity can be ignored and the effects of the impedances on beam dynamics are mainly affected by the perturbation of the imaginary part of the impedance proportional to the thickness. The real part of the impedance is not affected by the coating and the beam losses remain the same as in the case without coating.
Figure 5.4 shows the ratio between the impedance of a two-layer beam pipe with a coating of 100 nm thickness and conductivity 10^6 S/m and the impedance of a two-layer beam pipe with a coating of 100 nm thickness and conductivity 10^4 S/m, which is two order of magnitudes lower. The longitudinal and transverse impedances are shown on the left and right side of Figure 5.4 , respectively. These results have been obtained with the exact solutions of the ImpedanceWake2D code. These plots show that in this large conductivity range, as long as the thickness of the coating remains much smaller that the skin depth, the impedance does not change significantly, with a small difference of about 2% up to a frequency of 100 GHz. The

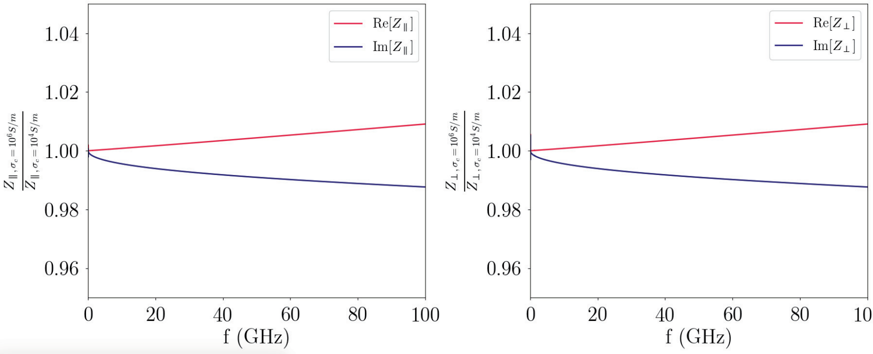

Figure 5.4: Ratio between the impedances of a two-layer beam pipe with a coating of 100 nm thickness and conductivities 10^6 S/m and 10^4 S/m, as given by ImpedanceWake2D, in the longitudinal (left side) and transverse (right side) planes. The red and blue curves represent the real part and the imaginary part of the impedance, respectively.

perturbation of the imaginary part of the impedance increases linearly with thickness up to values comparable with the skin depth, while for larger values Eqs. 82 and 83 become more complicated.

From all the results presented in this section, it follows that for the beam parameters considered for the lepton collider at low energy the contribution of the RW impedance can be reduced by decreasing the thickness of the coating. For this reason, the effects of NEG films with thicknesses below 250 nm on the single bunch beam dynamics have been studied by means of numerical simulations and will be presented in the following.

5.3 SINGLE BUNCH DYNAMICS

In Section 5.1, the impact of the RW impedance on beam dynamics has been evaluated analytically by using approximated expressions. This section presents more rigorous numerical studies on the effect on single bunch beam dynamics of reducing the thickness of coating.

Macro-particle beam dynamics has been simulated by using the tracking code PyHEADTAIL [77,78] developed at CERN to study a wide range of collective effects in synchrotrons. Systematic studies have been performed as comparisons with theoretical predictions and other simulation codes which take into account collective effects (SBSC [79], MuSiC [80] and BLonD [81],

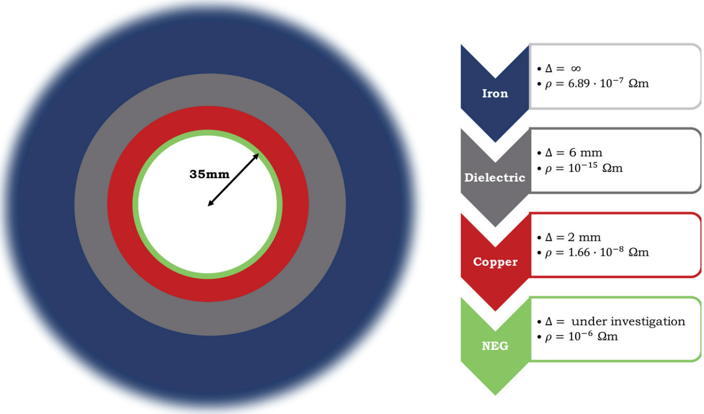

Figure 5.5: Model of the vacuum chamber used for simulations.

all of them benchmarked against theoretical and experimental data [82–84]). The excellent agreement found in all these comparisons increased the confidence in PyHEADTAIL results. PyHEADTAIL benchmark concerning TMCI threshold can be found in [76, 85].

For these studies, the vacuum chamber is assumed to be circular with 35 mm radius and three layers: a first inner layer of copper with 2 mm thickness, then 6 mm of dielectric to account for the gap between the beam pipe and the magnet chamber and finally the magnet chamber modelled as an outer layer of iron with resistivity $\rho = 10^{-7}$ Ωm and infinite thickness. As already discussed in Chapter 4, a coating of the copper surface is foreseen to reduce the SEY of the chamber walls for the mitigation of the EC build up in the machine. On the basis of the positive experience of the LHC warm sections [86, 87], it was decided to use TiZrV NEG films to provide a surface with low photon-stimulated desorption (PSD) and SEY [88].

In order to study the impact of the thickness of the coating on single bunch instability thresholds, four different thicknesses have been taken into account: 1 μm (which is the standard thickness used for accelerator purposes), 200 nm, 100 nm and 50 nm, with the beam parameters listed in Table 1. For these studies, the conductivity of NEG is assumed to be $\sigma_{NEG} = 10^6$ S/m [89].

The chamber model used for simulations is shown in Fig. 5.5. Figure 5.6 shows the real and imaginary part of the transverse and longitudinal RW impedances obtained by the ImpedanceWake2D code as a function of the frequency in the case of no coating and in the case of NEG coating with all the thicknesses under study. For the transverse impedance, the logarithmic scales have been used to highlight the behaviour at low frequency, which is important for the study of the transverse coupled bunch instabilities, as will be seen in Section 5.4.

It is important to observe that for all beam dynamics computations reported in this section the wakefield of this multilayer beam pipe obtained from ImpedanceWake2D has been used as input of tracking simulations. However, considering that in the frequency range of interest of the lepton collider the electromagnetic fields do not penetrate beyond the copper layer, all the considerations derived for the simplified analytic model of a two layer beam pipe presented in the previous section are valid also in the multilayer case.

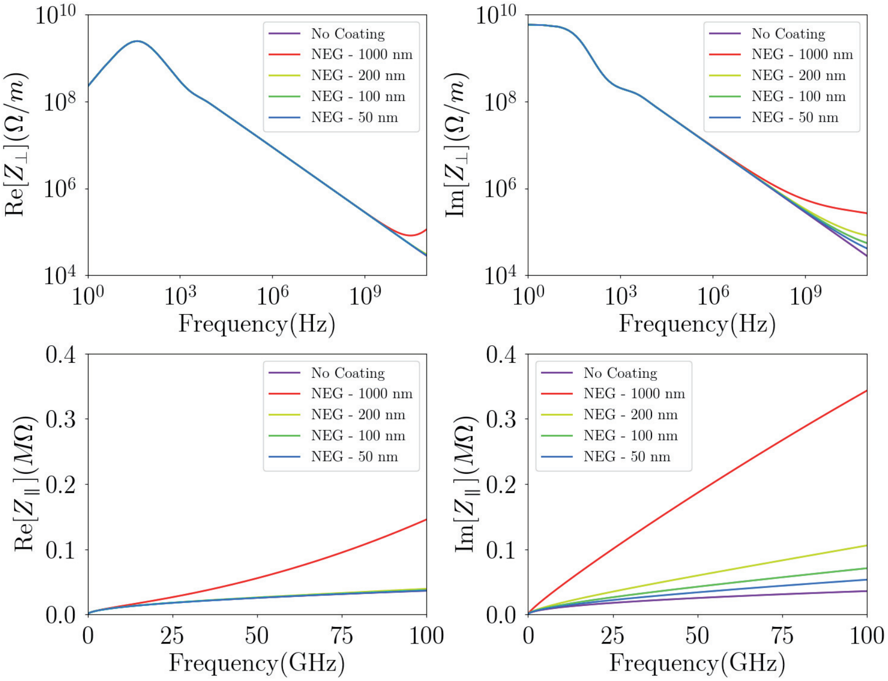

Figure 5.6: Real and imaginary part of transverse (top) and longitudinal (bottom) RW impedances as a function of the frequency for a copper pipe with 35 mm radius in the case of no coating and with NEG coating at different thicknesses.

5.3.1 *Longitudinal dynamics*

As most of the macroparticle tracking codes, PyHEADTAIL computes the wake potential as given by Eq. 16. This integral represents the energy gained or lost by a charge due to the entire bunch and has to be evaluated at each turn for each macroparticle. In order to have reliable results, a simulation usually tracks 10^6 macroparticles, which translates into more than 10^{11} operations at each turn for the computation of the wake potential. For numerical efficiency and in order to reduce the number of operations, the bunch is longitudinally divided into slices, each one containing a certain number of macroparticles. The wake potential within each slice created by all the previous slices is then computed and interpolated for all the macroparticles of the bunch.
However, the input wake function can cause some problems to simulations based on this approach, since if it varies in very short distances then a very large number of slices would be necessary, thus increasing the computational time [90]. One possible solution is to use as Green function for the code the wake potential of a very short bunch, i.e. the wake potential of a bunch with a bunch lenght $\sigma_z \simeq \frac{1}{10}\sigma_{z,nominal}$ corresponding to a relative error of about 0.5% in the computation [91].
Figure 5.7 shows the analytic wake potentials for a Gaussian bunch with nominal RMS bunch length $\sigma_{z,nominal} = 3.5$ mm compared to the wake potentials obtained from PyHEADTAIL as solutions of the convolution integral of Eq. 16, in the case of no coating and different thicknesses of NEG coating. These results show that the wake potential of a very short bunch can be treated as the wake potential generated from of a point charge, for all the cases under study.

Microwave threshold, bunch lengthening and potential well distortion

One important effect of the longitudinal RW wakefield on the single bunch dynamics is the microwave instability.
The energy spread remains constant below the instability threshold, above which it starts to increase with the bunch intensity. In these studies the instability threshold has been defined as the value of the bunch population corresponding to an increase of the energy spread of about 10% compared

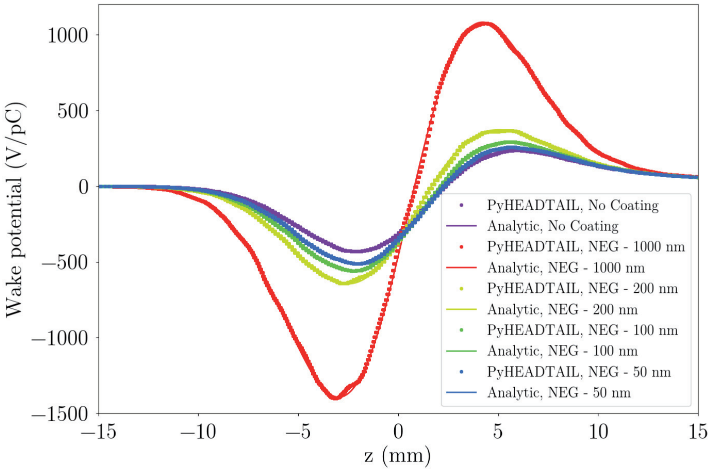

Figure 5.7: Comparison of the analytic longitudinal wake potentials of a 3.5 mm Gaussian bunch with the wake potentials obtained from PyHEADTAIL as convolution between the longitudinal bunch distribution and the wake potential of a 0.35 mm Gaussian bunch in the case of no coating, with a copper pipe of 35 mm radius, and with NEG coating at different thicknesses.

to its nominal value. Figure 5.8 shows the energy spread increase due to the RW longitudinal wakefield obtained from simulations as a function of the bunch population for all the investigated thicknesses. These results show that a standard coating of 1000 nm thickness makes the bunch unstable in

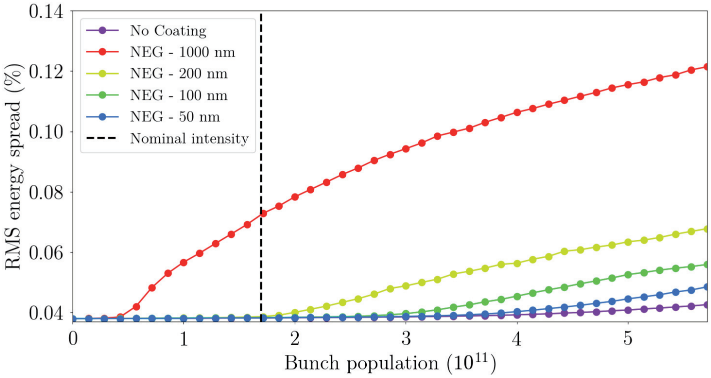

Figure 5.8: RMS energy spread as a function of the bunch population given by numerical simulations considering only the RW impedance in the case of no coating, with a copper pipe of 35 mm radius, and with NEG films at different thicknesses. The dashed black line correspond to the nominal bunch population.

the longitudinal plane, while thinner films allow to significantly increase the microwave instability threshold. For example, in the case of 100 nm thickness the instability threshold is increased by a factor 7 with respect to 1000 nm thickness and it is about 2 times higher than the nominal bunch intensity.

Numerical simulations have also been performed by taking into account the variation of NEG conductivity with frequency [76]. Figure 5.9 shows the microwave instability threshold as a function of the conductivity of the coating layer for all the considered thicknesses. This plot confirms what already stated in the previous section: for thin films with conductivities much smaller than the conductivity of the substrate, the threshold of the instability depends mainly on the thickness of the coating while it is not affected by its conductivity.

Another important effect is the increase of the bunch length with the bunch intensity, as shown in Fig. 5.10. For example, for the thinnest film of 50 nm, the bunch length at nominal current is about 5.7 mm, i.e. the bunch length is about 40% larger than its nominal value. This increase is only due to the RW impedance, while the studies presented in Chapter 7 will take into account all the machine components.

The longitudinal RW impedance is also responsible for the distortion of the

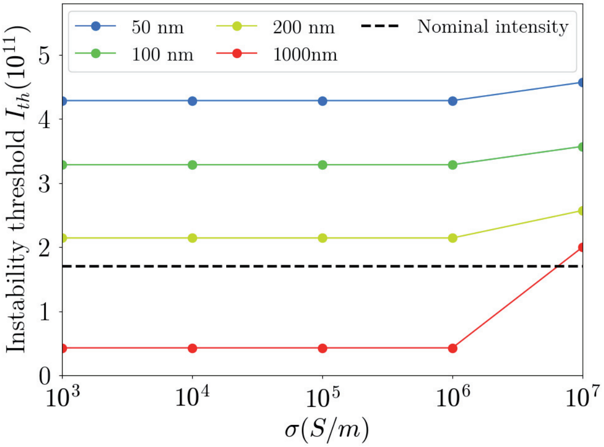

Figure 5.9: Microwave instability threshold as a function of the coating conductivity for all the thicknesses under study. The black dashed line corresponds to the nominal bunch intensity.

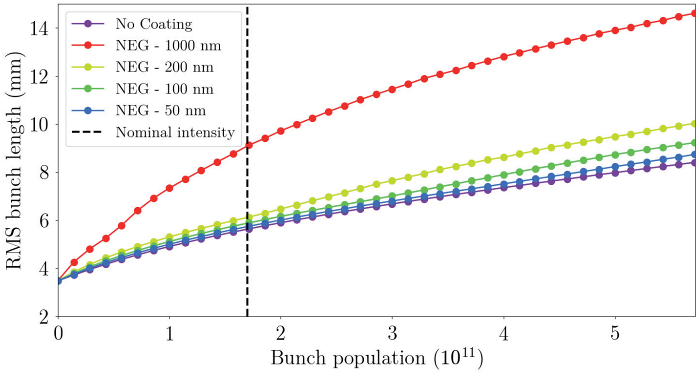

Figure 5.10: RMS bunch length as a function of the bunch population given by numerical simulations considering only the RW impedance in the case of no coating, with a copper pipe of 35 mm radius, and with NEG films at different thicknesses. The dashed black line correspond to the nominal bunch population.

bunch shape. The shape of a bunch is Gaussian at low intensities while there is a distortion as the bunch intensity increases. For intensities below the microwave instability threshold, the bunch length and the distortion from a Gaussian distribution can be predicted with the Haissinski integral equation in the form [92]

$$\lambda(z) = \lambda_0 e^{\frac{1}{E_0 \eta \sigma_{\epsilon 0}^2} \Psi(z)} \tag{84}$$

with

$$\Psi(z) = \frac{1}{C}\left[\int_0^z [eV_{RF}(z') - U_0]dz' - e^2 N_p \int_0^z dz' \int_{-\infty}^{z'} \lambda(z'')\omega_{\|}(z'-z'')dz''\right] \tag{85}$$

where λ_0 is a constant determined by normalization, η is the slippage factor, $\sigma_{\epsilon 0}$ is the RMS energy spread, V_{RF} is the RF peak voltage, U_0 is the energy lost per turn due to SR, and N_p the bunch population.

Figure 5.11 shows the bunch shape at nominal bunch intensity of 1.7×10^{11} with the corresponding bunch length in the case of no coating and with different thicknesses of NEG coating for FCC-ee at 45.6 GeV. In the case of the RW impedance, the Haissinski equation predicts an increase of the bunch length with the bunch intensity which is in good agreement with

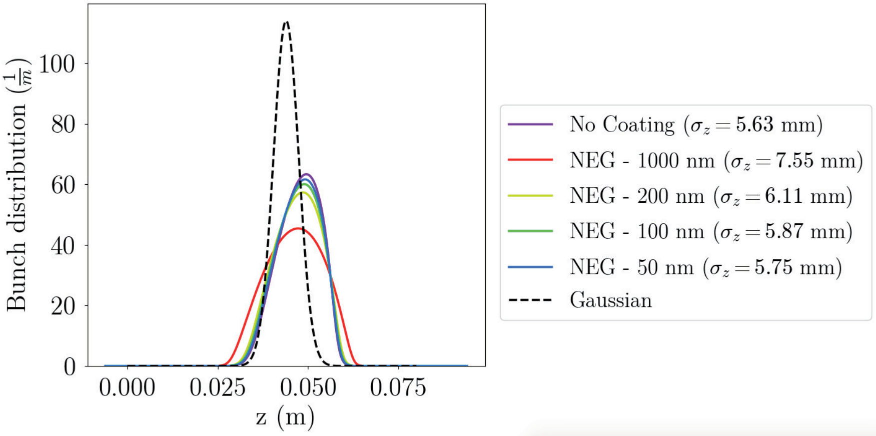

Figure 5.11: Longitudinal bunch distribution obtained from Haissinski equation at nominal intensity in the case of no coating, with a copper pipe of 35 mm radius, and with NEG films at different thicknesses. The dashed black line represents the Gaussian equilibrium shape.

the one predicted by numerical simulations and shown in Fig. 5.10, except for the 1000 nm thickness case that is indeed longitudinally unstable.

Loss factor

Figure 5.12 shows the loss factor as a function of the bunch length obtained by using Eq. (22) with $\Delta\phi$ given by numerical simulations data, in the case of 100 nm thick films with different conductivities. This plot shows that for such a small thickness of the coating the loss factor does not depend on the coating conductivity, thus confirming the results of the previous section. From the loss factor it is possible to derive the total power lost per turn by the beam as

$$P = \frac{N_b (N_p e)^2 k_{||}}{T_0} \tag{86}$$

with N_b the number of bunches per beam and T_0 the revolution period. From Fig. 5.12, the loss factor at nominal intensity is about 100 V/pC. This value, only due to the RW impedance, corresponds to a total power lost per beam of about 3.7 MW at Z resonance, representing about 7% of the SR power of 50 MW dissipated by the beam.

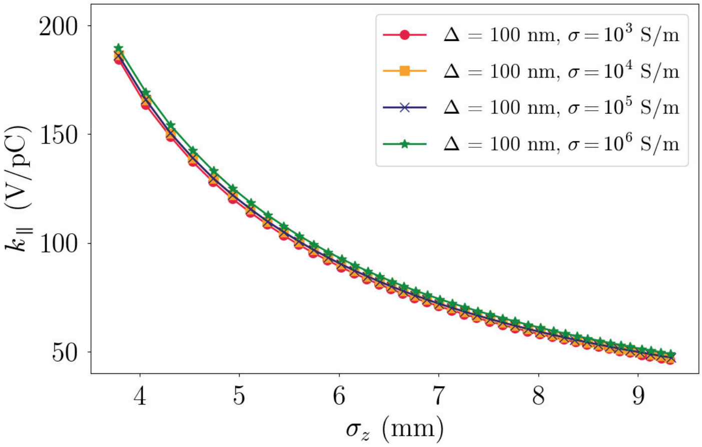

Figure 5.12: Loss factor as a function of the bunch length obtained from numerical simulations in the case of 100 nm thick films with different conductivities.

Incoherent synchrotron frequency shift and spread

Since the wake potential oscillates rigidly with the bunch, the dipole (rigid) coherent synchrotron frequency is not affected by the wakefield, contrary to all the other higher coherent modes (quadrupolar, sextupolar etc.) which do not represent rigid bunch motions. Also the internal motion of the particles in the bunch is affected by the longitudinal wakefield, resulting in a reduction of the synchrotron tune and a large incoherent synchronous tune spread. Both these effects influence the beam-beam performance, shifting the collider working point and affecting the coherent and incoherent beam-beam resonances. In order to evaluate the effect of the wakefield on the incoherent tune spread, the synchrotron frequency of the macroparticles at the nominal bunch intensity has been obtained with PyHEADTAIL, by considering a coating of 100 nm thickness. Figure 5.13 shows an histogram of the frequency distribution with and without wakefield, indicating a quite high incoherent tune shift of about a factor 2 compared to the unperturbed synchrotron tune $Q_s = 0.0248$. Figure 5.13 also shows a large incoherent spread, comparable with the synchrotron tune value. This result deserves further investigations in order to study how the incoherent synchrotron tune spread affects the X-Z coherent beam-beam instability appearing in

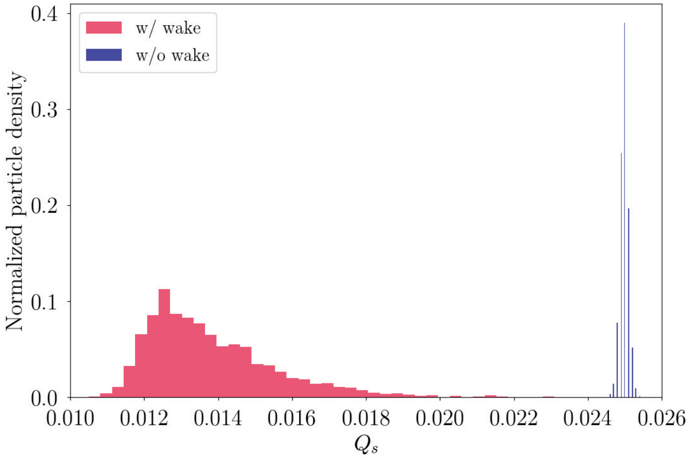

Figure 5.13: Incoherent synchrotron tune distribution at nominal intensity, produced by the RW impedance with a coating of 100 nm thickness. The results are obtained with PyHEADTAIL by using the machine parameters of Table 1 at Z resonance.

collisions with a large angle and coupling the horizontal and longitudinal motion [93].

5.3.2 *Transverse dynamics*

Another important effect of the transverse short range RW wakefield is the shift of the coherent betatron frequencies of the intrabunch modes when increasing the bunch intensity. The TMCI occurs when the frequencies of two neighboring modes are merging. Unlike the microwave instability in the longitudinal plane, above the transverse instability threshold the bunch is lost and this makes the TMCI very dangerous for the beam.

As already discussed in Section 5.1, an important RW effect is expected also in the transverse plane. For these studies, the TMCI threshold has been evaluated with the analytic Vlasov solver DELPHI [94], which uses a decomposition over orthogonal Laguerre polynomials for the radial modes, by considering the transverse impedance of NEG coatings at different thickness shown in Fig. 5.6. These studies take into account the bunch lengthening due to the longitudinal RW wakefields given by PyHEADTAIL at different intensities (see Fig. 5.10), by assuming a Gaussian distribution.

Figure 5.14 shows the real part of the tune shift of the first two radial modes, with azimuthal number going from -2 to 2, as a function of the bunch population, in the case of NEG coating with 100 nm and 1000 nm thicknesses. For both films, the TMCI threshold is a factor of about 2.6 higher than the nominal bunch intensity, as predicted analytically in Section 5.1. It is important to note that also in the transverse case the coating

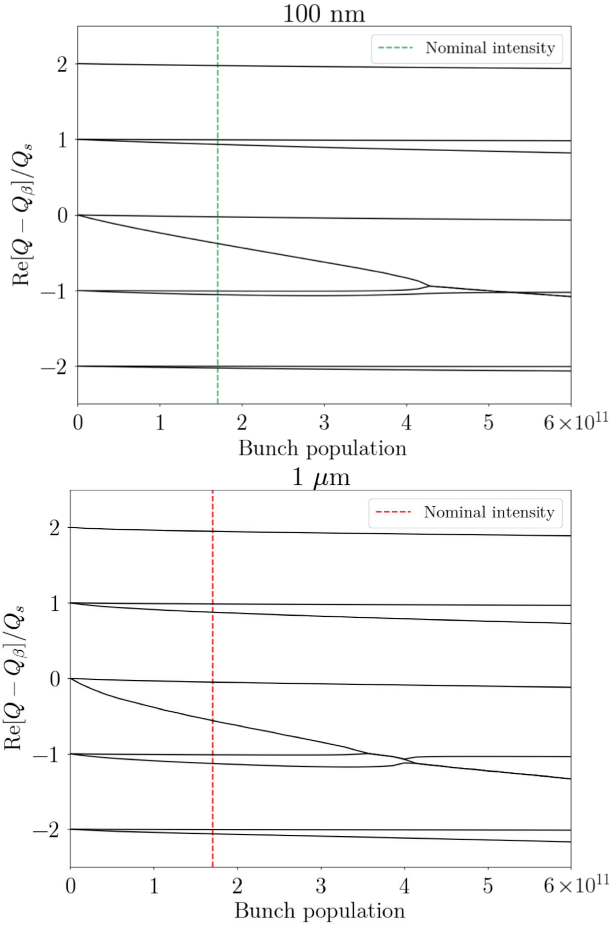

Figure 5.14: Real part of the tune shift of the first coherent oscillation modes as a function of the bunch population for 100 nm (top) and 1000 nm (bottom) thicknesses of NEG coating. The curves are obtained with DELPHI code by using the machine parameters of Table 1 at Z resonance and the bunch length given by PyHEADTAIL at different intensities. The dashed lines represent the nominal bunch population.

thickness affects the threshold of the instability, according to the results of Section 5.2, but to a lesser extent than it does in the longitudinal plane. The longitudinal impedance produces longer bunches at higher intensities which increase the TMCI threshold.

Another important effect related to TMCI is due to the collision with the other beam: two counterrotating beams can produce coherent dipole oscillation modes modifying the stability conditions. In this situation, coherent beam-beam effects and impedance are not independent and their interplay should be taken into account [95]. This subject, as well as the mitigation effect due to BS also based on colliding beams, is an important topic which deserves future investigations.

5.4 MULTI BUNCH DYNAMICS

5.4.1 *Transverse dynamics*

For the multibunch case, the most critical situation is related to the transverse coupled bunch instability due to the long range RW wakefield. In this case, the motion of the entire beam (and not of a single bunch) can be considered as the sum of coherent coupled bunch modes. The growth rate of the lowest azimuthal mode $m = 0$ for a Gaussian bunch is given by [96]

$$\alpha_{\mu,\perp} = -\frac{cI}{4\pi \frac{E_0}{e} Q_\beta} \sum_{q=-\infty}^{\infty} Re\left[Z_\perp\left(\omega_q\right)\right] G_\perp(\sigma_\tau \omega_q') \tag{87}$$

where I is the total beam current, E_0 the machine energy, Q_β the betatron tune, σ_τ the RMS bunch length in time, $G_\perp$ a form factor due to the bunch shape assumed to be equal to 1 and

$$\omega_q = \omega_0\left(qN_b + \mu + Q_\beta\right) \qquad \omega_q' = \omega_q + \omega_0 \xi \frac{Q_\beta}{\mu} \tag{88}$$

with N_b the number of bunches, ξ the chromaticity, ω_0 the revolution frequency and μ an integer number from 0 to $N_b - 1$ representing a coupled bunch mode. The instability occurs when α_μ is positive, i.e. when the real part of the transverse RW impedance given by Eq. 72 is evaluated at negative frequencies. Positive frequencies give rise instead to damped oscillations.

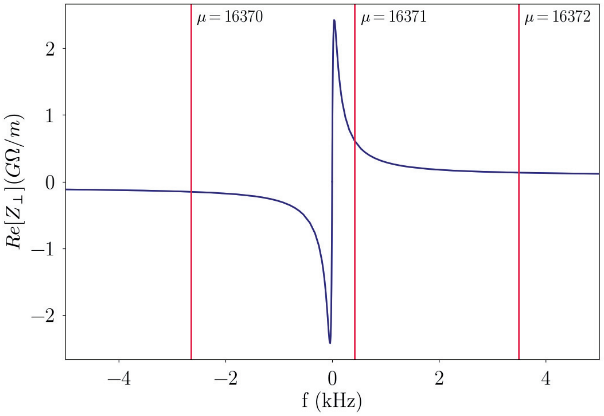

Figure 5.15: Vertical coupled bunch spectrum obtained by using the machine parameters of Table 1 at Z resonance and real part of the resistive wall impedance for a copper beam pipe of 35 mm without coating, as a function of frequency around f = 0.

Moreover, the transverse impedance is inversely proportional to the square root of the frequency. Therefore, the most dangerous coupled bunch mode is the one with coherent frequency ω_q closest to zero and negative. By considering for example the beam parameters at Z resonance and q = -1 and by defining as Q_0 and ν_β the integer part and the fractional part of the betatron tune, respectively, i.e. $Q_\beta = Q_0 + \nu_\beta$, the most dangerous coupled bunch mode can be obtained from Eq. 88 as $\mu = N_b - Q_0 - 1$ = 16370 and its lowest negative frequency is equal to $\omega_q = -\omega_0(1 - \nu_\beta)$. By considering in Eq. 87 a single betatron frequency line instead of the sum over q, for the vertical plane with a fractional part of the tune of ν_y = 0.22 the growth rate of the most dangerous mode is about 435 s^{-1}, corresponding to a rise time of 2.3 ms, i.e. 7 machine turns. This value has been obtained by using a NEG coating of 100 nm thickness but the results for the other thicknesses do not change significantly, since the real part of the transverse impedance at low frequencies is not affected by the thickness and the conductivity of the material. It is also important to note that the transverse radiation damping time is about 0.83 s, corresponding to 2550 turns, i. e. it is much longer than required for instability suppression.

Figure 5.15 shows the beam spectrum of three coupled bunch modes and the real part of the transverse impedance of a 35 mm copper pipe without

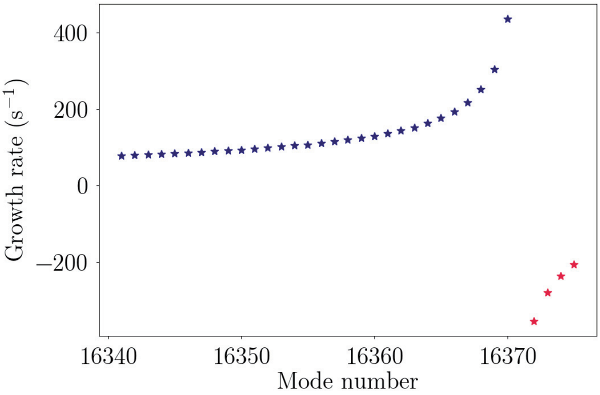

Figure 5.16: Growth rate of the coupled bunch modes with azimuthal mode number $m = 0$.

coating close to zero frequency, while Fig. 5.16 shows the growth rate as a function of the coupled bunch mode number, highlighting the presence of several unstable modes that need to be damped. The rise times of these modes are in the range of few milliseconds, which are usually cured by transverse bunch by bunch feedback systems in other lepton factories [97]. However, in the case of FCC-ee these rise times correspond to few turns due to the large circumference of the machine and a new challenging feedback system is required. Some schemes to cope with this fast instability have been proposed in [98].

5.4.2 *Longitudinal dynamics*

Similarly to the transverse case, by neglecting the coupling between different azimuthal modes and by considering only the lowest longitudinal azimuthal mode m = 1, the real part of the longitudinal impedance can produce stability or instability depending on the sign of the growth rate:

$$\alpha_{\mu,\parallel} = -\frac{\mu I}{4\pi \frac{E_0}{e} Q_s} \sum_{q=-\infty}^{\infty} Re\left[Z_{\parallel}\left(\omega_q\right)\right] G_{\parallel}(\sigma_\tau \omega_q) \tag{89}$$

where Q_s is the synchrotron tune and $\omega_q = \omega_0\left(qN_b + \mu + Q_s\right)$. In the longitudinal case, the real part of the impedance is always positive and stability occurs for negative frequencies. The worst and most unstable case occurs when the resonance frequency ω_r of the high order mode (HOM) is equal to $\omega_q > 0$. By considering in Eq. 89 the coupling with a single synchrotron frequency line of the coupled bunch modes and not the sum of the impedance over the frequency, the growth rate of the most dangerous unstable mode is given by

$$\alpha_{\parallel} = -\frac{\mu I}{4\pi \frac{E_0}{e} Q_s} \omega_r R_s \tag{90}$$

where R_s is the HOM shunt impedance. This growth rate must be compared with the natural damping rate due to SR which is about 1270 turns on the Z resonance.

Figure 5.17 shows the maximum HOM shunt impedance as a function of the resonance frequency, such that the corresponding growth rate is exactly balanced by the radiation damping. Also in the longitudinal case, the development of a feedback system is required for safe operation.

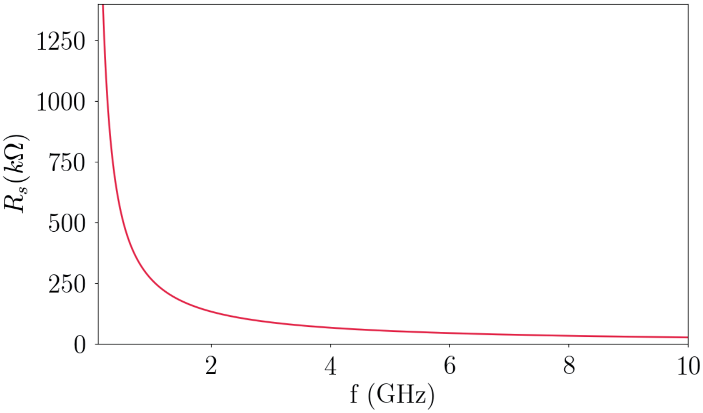

Figure 5.17: Maximum shunt impedance of a HOM as a function of its resonance frequency, producing a growth rate which is compensated by the natural radiation damping.

6

ACTIVATION OF NEG THIN FILMS AND SEY MEASUREMENTS

As discussed in Chapter 4, one possible strategy to mitigate the EC build up in the future lepton collider is to lower the SEY of the beam pipe walls by applying a coating of non-evaporable getters (NEG), an alloy of the three metals Ti, Zr and V. Compared to other materials like Titanium Nitride (TiN) and amorphous Carbon (aC), these getters are characterized by low photon-stimulated desorption (PSD) and SEY.

However, studies on single bunch beam dynamics presented in Section 5.3 pointed out that the standard NEG thickness of 1 μm increases significantly the RW impedance seen by the beam, making it responsible for quite low single bunch instability thresholds, in both transverse and longitudinal planes. It has also been demonstrated that for the beam parameters considered for the lepton collider at low energy the contribution of the RW impedance can be reduced by decreasing the thickness of the coating.

Chapter 5 was focused on impedance requirements: the effects of NEG thin films on single bunch beam dynamics have been studied by means of numerical simulations, indicating that thicknesses below 250 nm allow increasing significantly the instability thresholds. However, reducing the thickness of NEG coatings can affect the performance of the material itself and therefore the maximum SEY and related EC mitigation.

For this reason, an extensive measurement campaign was performed at CERN to characterize TiZrV films with thicknesses below 250 nm, with the purpose of finding the minimum effective thickness satisfying vacuum and EC requirements.

This chapter is focused on the experimental characterization of NEG thin films. Sections 6.1 and 6.2 describe the properties of the material and the coating process while Section 6.3 presents the characterization of samples in terms of activation performance, investigated by surface analysis, and

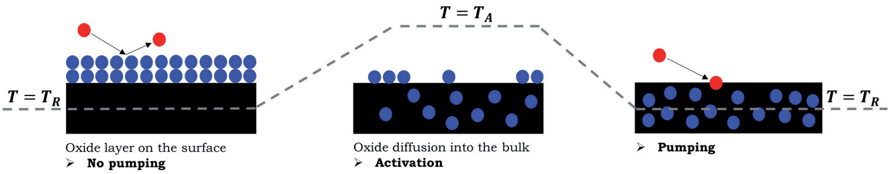

Figure 6.1: NEG activation: the dissolution process of the oxide into the bulk is obtained by heating in vacuum.

SEY measurements. Finally, Section 6.4 investigates the impact of SEY measurements on EC build up simulations.

6.1 NON-EVAPORABLE GETTERS

Getters are materials that can absorb gas molecules thus ensuring the pumping of a vacuum system. In order to perform this task, their surface must be clean. In general, when a surface is exposed to air, it reacts chemically with oxygen and an oxide layer grows on it. When the clean surface is obtained by diffusion of the oxide layer into the bulk by heating the material in vacuum (**activation** process), one refers to **non-evaporable getters** [99] (see Fig. 6.1). Usually NEG thin films are deposited on alluminum or copper vacuum chambers (as in the case of FCC-ee), transforming the pipe walls from a gas source into an effective pump. In addition to their pumping properties, NEG films are able to reduce the gas desorption and SEY of the surface, thus representing an excellent solution to vacuum issues and EC mitigation.

6.2 SAMPLE PREPARATION

In order to evaluate the activation performance and SEY, NEG thin films at target thicknesses of 1000 nm, 200 nm, 100 nm and 50 nm were deposited on 12 chemically polished copper samples with dimensions 20x20x2 mm by DC magnetron sputtering [100] in the cylindrical coating system shown in Fig. 6.2. The working principle of the sputtering system is shown in Fig. 6.3. A noble gas (in this case Krypton at a pressure of about $2.1 \cdot 10^{-2}$ mbar) is introduced into the system through a valve. A negative potential is

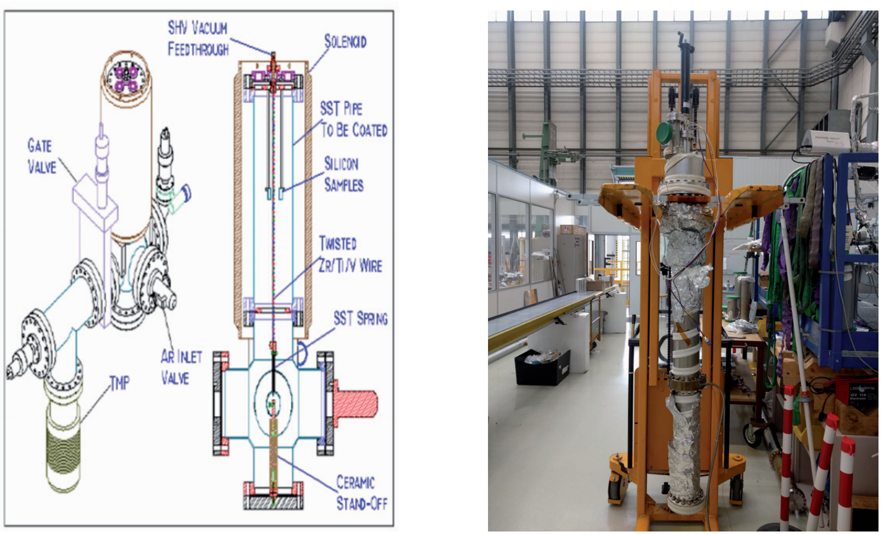
SHV VACUUM FEEDTHROUGH
SOLENOID
SST PIPE TO BE COATED
SILICON SAMPLES
GATE VALVE
TWISTED ZR/TI/V WIRE
SST SPRING
AR INLET VALVE
TMP
CERAMIC STAND-OFF

Figure 6.2: Magnetron sputtering system.

applied to the cathode or target (in this case consisting of intertwisted 3 mm diameter wires of Ti, Zr and V) so that free electrons will accelerate away, approach the neutral Kr atoms and produce positively charged ions by driving off their outer shell electrons. These ions will be accelerated

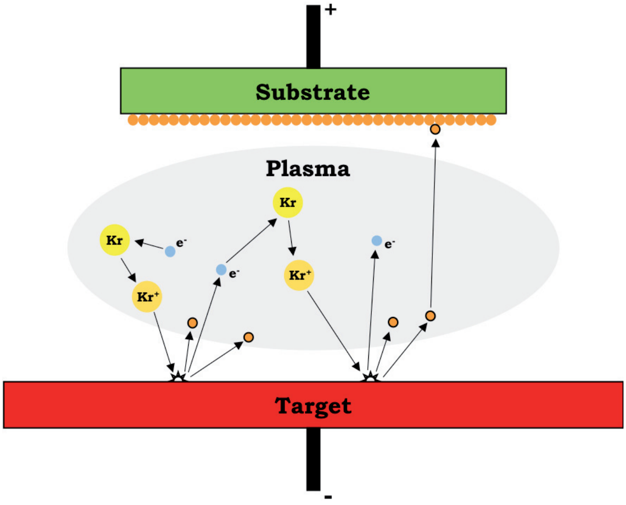
+
Substrate
Plasma
Kr
Kr
e^-
e^-
Kr^+
Kr^+
e^-
Target
-

Figure 6.3: Magnetron sputtering working principle.

into the cathode, striking its surface and extracting more free electrons and atoms from the different wires. A fraction of free electrons would tend now to move away from the negative charged wire but the 200 G magnetic field generated by the solenoid mantains these electrons around the target and "feeds" the plasma, by ionizing other gas atoms. Another fraction of free electrons recombines with ions and the resulting neutral gas atoms gain an energy that has to be release in the form of photons for the energy conservation law. This explaines the brightness of the plasma (see Fig. 6.4). The atoms extracted from the target will be recombined on the samples, giving rise to Ti-Zr-V composition.

In this coating process the stainless steel vacuum chamber was 95 mm in diameter and 1.5 m long, positioned in the centre of the solenoid. Samples were mounted at 46 mm from the cathode and a movable mask allowed deposition of coatings at different thickness in the same run.

Film composition was measured to be 28 atomic % (at.%) Ti, 29 at.% Zr and 43 at.% V by energy dispersive X-ray spectroscopy (EDS).

The thickness was measured on cross sections of the samples and determined by Scanning Electron Microscopy (SEM) [101]. The working principle of this kind of imaging is shown in Fig. 6.5. An electron beam is scanned

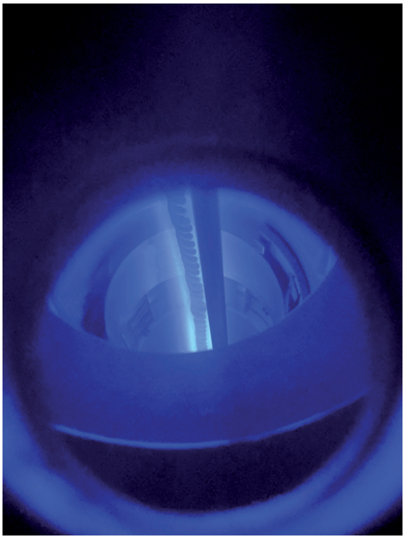

Figure 6.4: The blue light is produced by the plasma when sputtering TiZrV cathode.

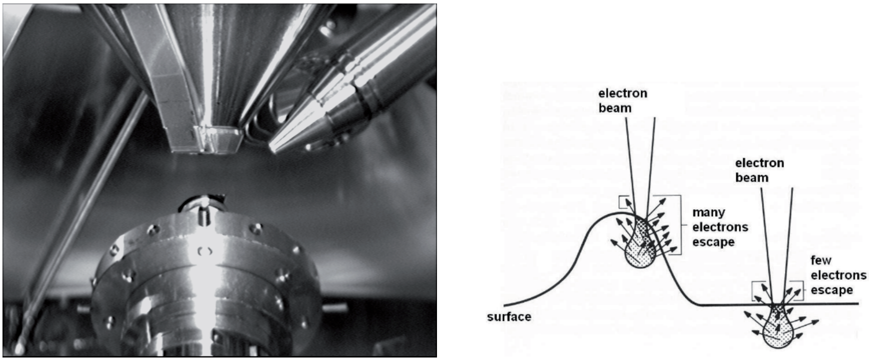

Figure 6.5: SEM analysis system (left side) and edge effect (right side).

across the surface of the sample and secondary electrons are emitted from each point of the surface, providing information about its morphology and topography. In fact, the brightness of each pixel in the output image is proportional to the emitted current, in accordance with the so called edge effect: the secondary electron emission from the surface of the samples depends on the incidence angle on the sample surface (defined w.r.t. the normal to the surface) [38] which means the higher the angle, the higher the emission. SEM images are shown in Fig. 6.6, resulting in film thicknesses of 1100 nm, 203 nm, 87 nm and 30 nm, obtained as average values from five measurements.

Figure 6.7 shows the surface morphology of each sample: as seen by SEM, the films cover the entire surface with a homogeneus thickness, while thicker films show an increasing roughness, the latter playing an important role on surface adsorption capacity and impedance.

After deposition, all samples were vented to air and wrapped in Al foil before being introduced into the vacuum system for characterization. In the following these samples will be referred as "as received" samples.

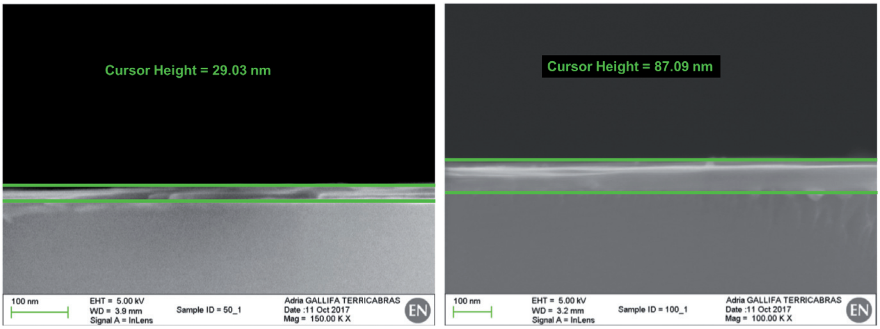
Cursor Height = 29.03 nm
100 nm
EHT = 5.00 kV
WD = 3.9 mm
Signal A = InLens
Sample ID = 50_1
Adria GALLIFA TERRICABRAS
Date :11 Oct 2017
Mag = 150.00 K X
EN
Cursor Height = 87.09 nm
100 nm
EHT = 5.00 kV
WD = 3.2 mm
Signal A = InLens
Sample ID = 100_1
Adria GALLIFA TERRICABRAS
Date :11 Oct 2017
Mag = 100.00 K X
EN

(a) 30 nm. (b) 87 nm.

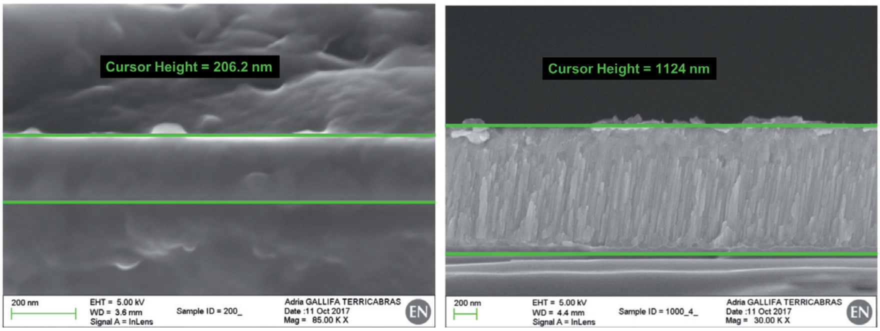
Cursor Height = 206.2 nm
200 nm
EHT = 5.00 kV
WD = 3.6 mm
Signal A = InLens
Sample ID = 200_
Adria GALLIFA TERRICABRAS
Date :11 Oct 2017
Mag = 85.00 K X
EN
Cursor Height = 1124 nm
200 nm
EHT = 5.00 kV
WD = 4.4 mm
Signal A = InLens
Sample ID = 1000_4_
Adria GALLIFA TERRICABRAS
Date :11 Oct 2017
Mag = 30.00 K X
EN

(c) 203 nm. (d) 1100 nm.

Figure 6.6: SEM images of NEG thin films on copper substrate.

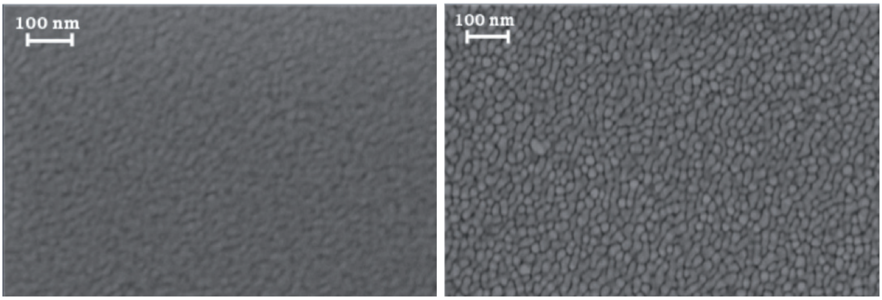
100 nm
100 nm

(a) 30 nm. (b) 87 nm.

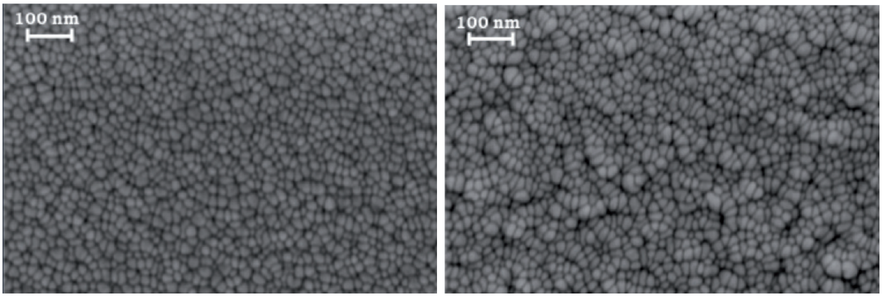
100 nm
100 nm

(c) 203 nm. (d) 1100 nm.

Figure 6.7: Morphology of NEG thin films analyzed by SEM.

6.3 SAMPLE CHARACTERIZATION

6.3.1 *XPS analysis*

The activation performance was measured by X-ray Photoelectron Spectroscopy (XPS) [102] by following changes to surface composition during a thermal treatment. A XPS system is illustrated schematically in Fig. 6.8. X-rays at fixed energy $h\nu$ are irradiated on the surface of the sample and ionize its atoms by extracting electrons. For the conservation of energy, the kinetic energy of these ejected electrons is given by

$$E_k = h\nu - E_B - E_{WF} \tag{91}$$

where E_B is the characteristic binding energy of the electron, defined as the difference in energy between the ionized and neutral atoms, and E_{WF} is the work function of the surface. An electron energy analyzer measures the kinetic energy distribution of the emitted electrons, i.e. the number of emitted electrons as a function of their kinetic energy, allowing to record a photoelectron spectrum in which all the surface elements can be identified from their characteristic photoelectron peaks. For these studies, all spectra were acquired by using a monochromatic MgK_α source (1253.6 eV) with 350 W power at 45° emission angle. Multiplex spectra were collected by

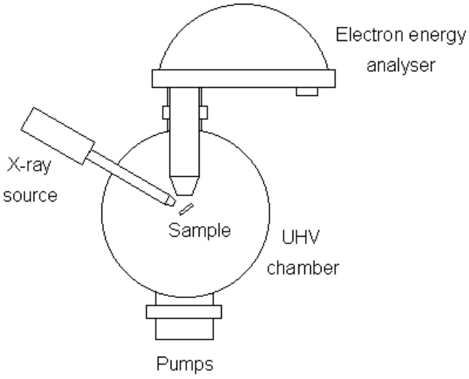

Figure 6.8: Schematic view of a XPS system, consisting of a X-ray source, an electron energy analyzer and a ultra high vacuum environment.

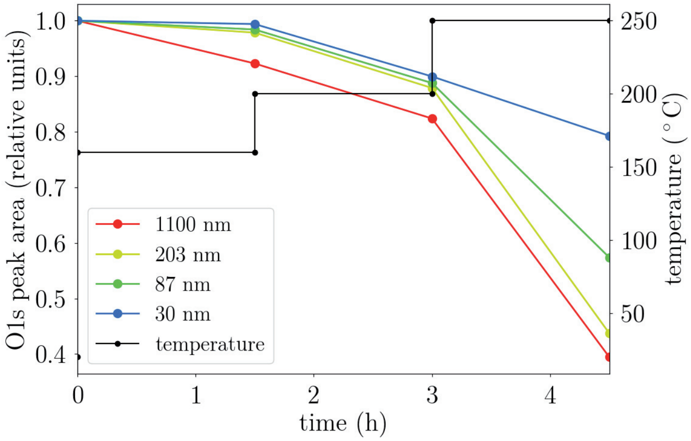

Figure 6.9: Activation performance: reduction of the area of the oxygen peak from the XPS spectrum after the fourth activation cycle.

a PHI-ESCA 5400 analyzer operating in small area mode with 35 eV pass energy. The XPS spectra have been taken at four different steps for a total activation time of 4 hours:

- as received sample, at room temperature
- after 1 hour heating at 160°C
- after 1 hour heating at 200°C
- after 1 hour heating at 250°C

This procedure of 4 steps will be referred to as a cycle in the following. This thermal activation was performed for 4 cycles, with air exposure between two consecutive cycles. The activation performance was evaluated by the reduction of the area of the oxygen peak O1s during a cycle of 4 hours. Figure 6.9 shows the O1s peak area as a function of the activation time and temperature after the fourth activation cycle: a higher reduction of the oxygen corresponds to a better activation and the plot shows that the oxygen surface concentration is increasing for thinner layers. In particular, for the 1100 nm film the oxygen decrease after activation is about 60% while for the 30 nm film the oxygen reduction is only 20%. Figure 6.10 shows the activation effects in the C1s peak area evolution with the temperature for all the thicknesses under study while Table 6 compares the metallic surface composition of NEG thin films determined in the as received state

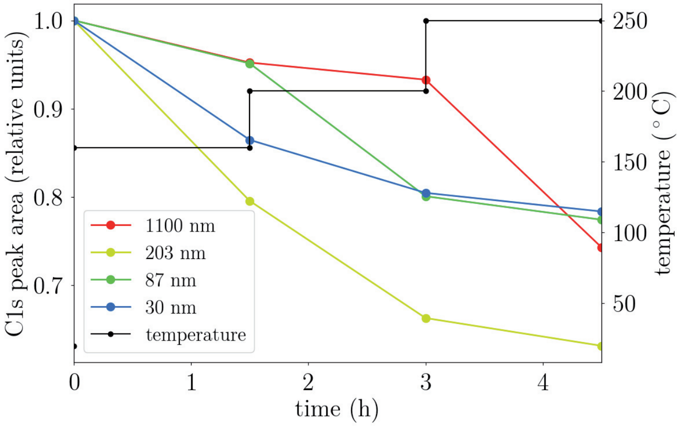

Figure 6.10: C1s peak area as a function of the activation temperature after the fourth activation cycle.

at the first and fourth activation cycles. Only metals are considered for the computation of the relative concentrations, calculated by normalizing the total concentration of the metals to 100%. These results show that after three activations Ti and Zr enrich while V content decreases. XPS analysis also allowed observations of the oxidation state of the metals. The collected signals from Ti, Zr and V on the uppermost surface of the films for activated states after the fourth activation cycle are shown in Fig. 6.11. The as-received 1100 nm film has been taken as reference to visualize the shift of Zr3d, Ti2p and V2p peaks occurring during the NEG activation process. The analysis of these photopeaks reveals the presence of mainly metallic components on Ti and V while the Zr signal, which is the most sensitive in terms of activation due to its higher binding energy with oxygen, shows still a strong oxide component for the 87 nm and 30 nm films after activation.

	Ti		**Zr**		**V**	
	Act. I	**Act. IV**	**Act. I**	**Act. IV**	**Act. I**	**Act. IV**
30 nm	23.7	26.8	44.8	57.7	31.4	15.5
87 nm	24.7	27.5	42	49	33.3	23.5
203 nm	23.5	26.5	43	50.8	33.5	22.7
1100 nm	23.6	27.3	38.4	44.3	38	28.3

Table 6: Metallic surface composition in at.% determined in the as received state at the first and fourth activation cycles.

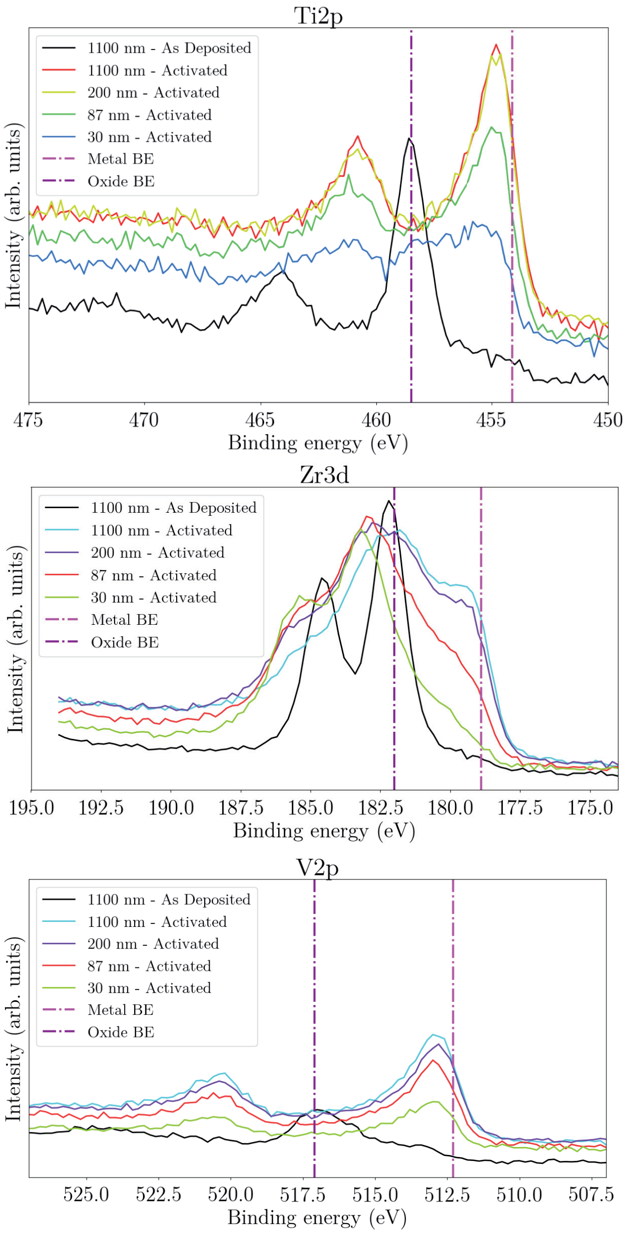

Figure 6.11: Ti2p (top), Zr3d (centre) and V2p (bottom) photopeaks obtained by XPS analysis for all the thicknesses under study. 2p and 3d refer to subshells of electronic configuration.

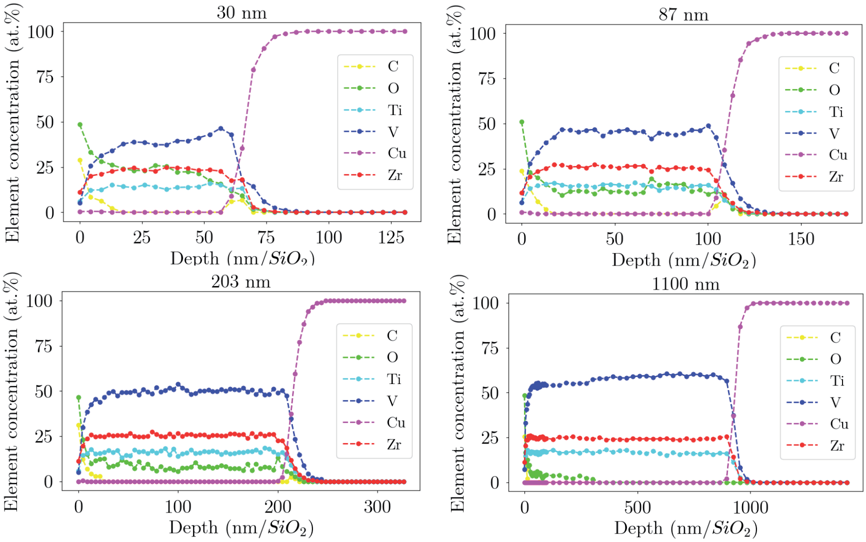

Figure 6.12: Profile of C, O, Ti, V, Zr and Cu as a function of depth for all the samples.

6.3.2 *Depth profile*

Figure 6.12 shows the depth profile, i.e. a XPS profiling of C, O, Ti, Zr, V and Cu from the surface of the layer to the Cu substrate, after the fourth activation cycle for each sample, in order to determine the elemental composition as a function of depth. The XPS profile was obtained by successive data acquisition and etching steps, performed using Ar^+ ions at 2 kV with an etching rate calibrated from a standard SiO_2 layer. This analysis shows that the oxygen content (green curve) is decreasing rapidly in all films but while in the 1100 nm sample it decreases below 5% in less than 100 nm, in the thinner samples it is detected in the whole layer, with the highest percentage close to 25% for the 30 nm film. As illustrated in the next section, the presence of oxygen in the layer affects the activation performance and as a consequence the SEY. The migration of oxygen from the surface oxide to the bulk of the material is a diffusion process driven by concentration gradient, temperature and time and depending on the material structure (defining the availability of diffusion pathways). The diffusion of oxygen from high to low concentration zones will be faster in the case of a steep gradient, which is not the case of the 30 nm film, with an oxygen concentration going from 50% at the surface to 30% inside the layer. This represents a big loss in gradient and the major limiting factor, considering that the material structure is not changing at this activation temperature [103].

6.3.3 *SEY measurements*

Build up simulations presented in Chapter 4 predict a maximum SEY of 1.2 for the surfaces of the FCC-ee vacuum system, in order to run the IR without EC multipacting and to have the lowest heat load in the arcs. From the literature [104], the maximum SEY of the clean metals Ti and Zr are 0.9 and 1.1, respectively, but these values increase when surfaces are exposed to air and covered with contaminating species. This section will present SEY measurements for all the samples under study, showing the dependence of SEY on the coating thickness and the activation time. SEY measurements were performed by using the apparatus shown in Fig. 6.13, consisting of an electron gun to produce primary electrons, a collector for emitted electrons and a holder with the samples under study. Primary electrons are accelerated in the electron gun to energies up to 1800 eV. All

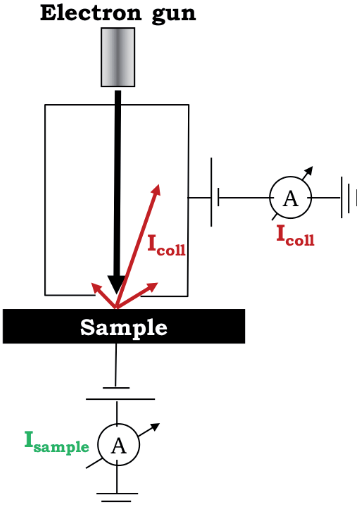

Figure 6.13: Experimental setup for SEY measurements.

the SEY measurements reported in this section have been carried out with a low primary electron current of about 5 nA and an angle of incidence normal to the surface of the sample. The beam was moved away from the surface in between each measured point in order to avoid irradiation dose during the adjustment to the new primary energy. The electron dose received by the sample during one full SEY curve is below 10^{-6} C/mm^2 to avoid any conditioning effect. A positive voltage (+45 V) is applied to the collector in order to capture all secondary electrons emitted by the sample and a negative bias (-18 V) is applied to the sample. The sample current I_{sample} and the secondary electron current I_{coll} are measured simultaneously by two current amplifiers with an accuracy of $\pm 1\%$ and the total SEY is computed as

$$\delta = \frac{I_{coll}}{I_{coll} + I_{sample}} \tag{92}$$

All samples were analyzed after XPS heating and were exposed to air between two consecutive activation cycles. A reproducibility of $\pm 3\%$ can be considered for all the measurements reported in this section.

Influence of thickness on SEY

Figure 6.14 shows the SEY curves of NEG thin films for all the thicknesses under study after the fourth activation cycle. The highest SEY of about 1.5 is obtained for the thinnest coating of 30 nm, due to incomplete activation, while the SEY value for a 87 nm coating is about 1.25 and is lower for thicker films. The oxygen reduction and the maximum SEY as a function of the coating thickness are shown in Fig. 6.15: elevated concentrations of oxygen in thinner films are responsible for higher SEY. In general, this is not a systematic effect: as an example, for initially clean copper the maximum SEY value decreases after pure oxygen exposure for higher doses of oxygen [105]. However, in the case of Ti, Zr and V the increase of the SEY with oxygen is due to the building up of the oxides of these metals which have a higher SEY than the clean metal surface. These oxides are insulators or wide-band-gap semiconductors, meaning that secondary electrons which are excited can escape much easier from their surface provoking a higher SEY.

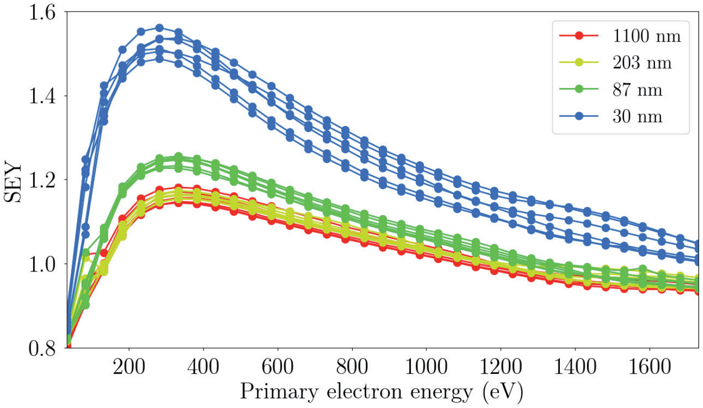

Figure 6.14: SEY as a function of the primary electron energy for all the samples under study after the fourth activation cycle of 4 hours up to a temperature of 250°C.

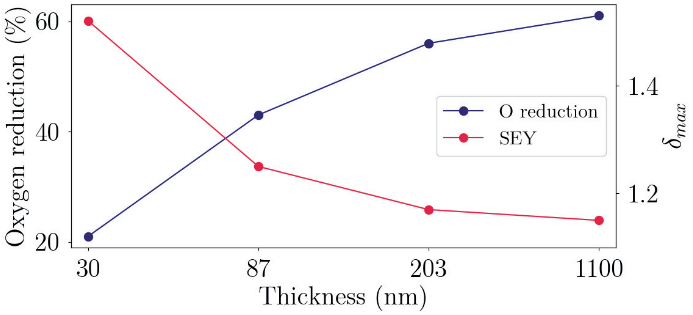

Figure 6.15: Oxygen reduction and maximum SEY as a function of the coating thickness for all the samples under study after the fourth activation cycle of 4 hours up to a temperature of 250°C.

Influence of activation time on SEY

Further SEY measurements have been performed at the same temperatures after longer activation cycles of 24 hours which are typical activation times for accelerator use. Observations after longer activation times show a lower SEY compared to the one obtained after shorter activation times, as shown in Fig. 6.16, where for example the maximum SEY for the 87 nm film was reduced from 1.25 to 1.16. These results confirm that activation is mainly a diffusion limited process: longer activation times allow oxygen at the film surface to migrate away and to lower the electron yield.

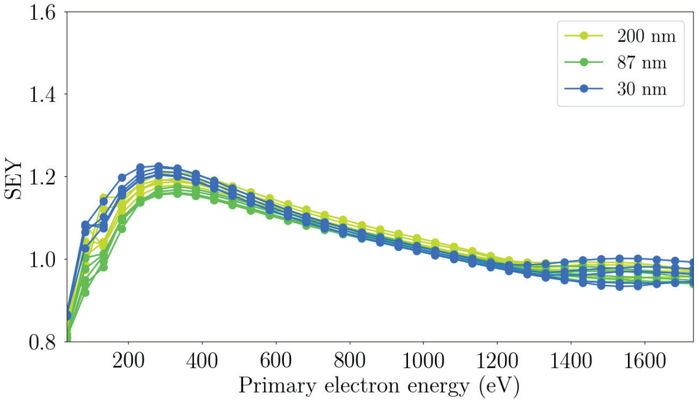

Figure 6.16: SEY as a function of the primary electron energy for the thin films after the fourth activation cycle of 24 hours up to a temperature of 250°C.

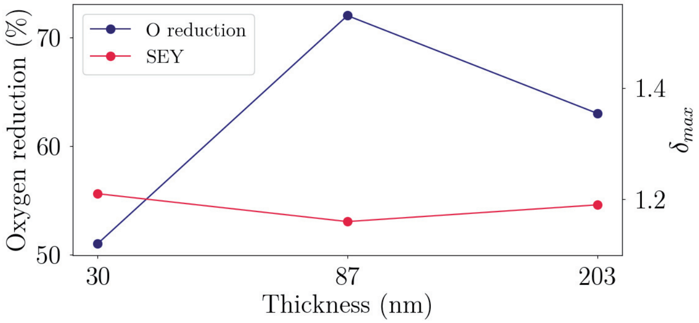

Figure 6.17: Oxygen reduction and maximum SEY as a function of the coating thickness for the thin films after the fourth activation cycle of 24 hours up to a temperature of 250°C.

6.4 IMPACT OF SEY MEASUREMENTS ON EC BUILD UP SIMULATIONS

In order to investigate the impact of SEY measurements on EC build up simulations, the measured SEY curve of the 87 nm film has been taken as reference (black dashed line in Fig. 6.18) and compared with the analytic SEY curve given by Eqs. 46, 47 and 48 for $\delta_{max} = 1.16$ and LHC chamber parameters (blue line). The orange curve is obtained from the analytic model by changing the parameter R_0 of the elastic component from 0.7 to 0.1 and the parameter s of the true secondary component from 1.35

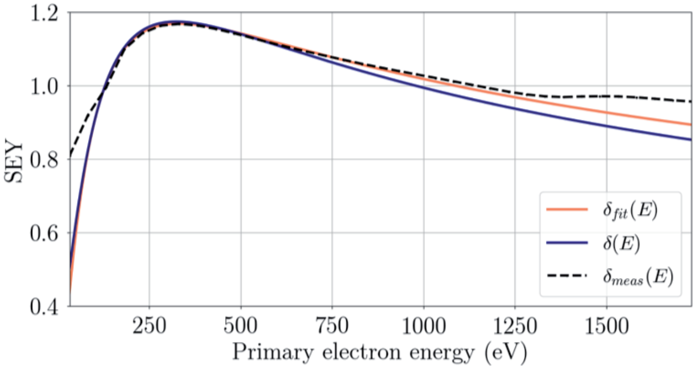

Figure 6.18: Analytic curve for $\delta_{max} = 1.16$ and LHC chamber parameters (blue), measured curve of the 87 nm film with $\delta_{max} = 1.16$ and fit curve obtained by modified free parameters.

to 1.30, in order to fit the measured trend. Build up simulations have been performed for all the machine components at SEY = 1.16 using the optimized parameters, i.e. $R_0 = 0.7$, $E_0 = 150$ eV, $s = 1.30$ and $E_{max} = 332$ eV. Results are shown in Fig. 6.19: for all the components, the heat load does not significantly differ from previous results, confirming that the SEY model used for simulations and based on LHC measurements is a good approximation for the measured SEY curves of NEG thin films proposed for the lepton collider.

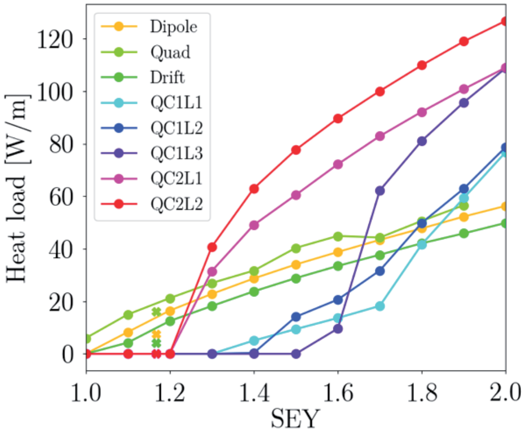

Figure 6.19: Heat load at SEY = 1.16 for all the machine components compared with previous results, in the case of 15 ns beam.

7

THE FCC-EE LONGITUDINAL IMPEDANCE MODEL

In addition to the RW impedance, there are other sources of wakefields in the machine that will be described in this chapter. The studies on the effects of the RW impedance presented in Chapter 5 indicate that its contribution on beam dynamics is very important, especially in multi bunch operation where active feedback systems are required to keep under control beam instabilities. As the main impedance source, the RW wake potential can be taken as reference to compare the wake potentials of all the other machine devices. Section 7.1 will describe all the current machine components and their optimization from the impedance point of view while Section 7.2 will present the longitudinal impedance budget.

7.1 OTHER IMPEDANCE SOURCES

7.1.1 *RF cavities and tapers*

For the Z case, the RF system consists of about 56 LHC-like cavities at 400 MHz [106] with a single cell, as the one shown in Fig. 7.1.

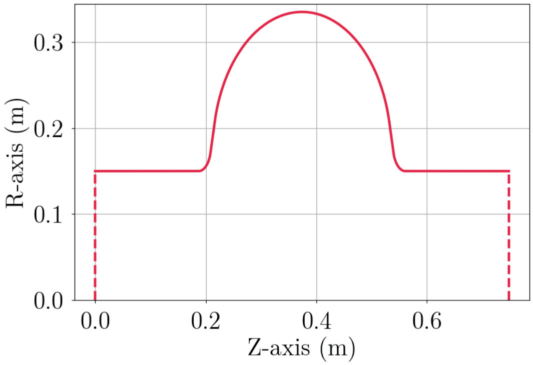

Figure 7.1: 400 MHz single cell cavity used in ABCI.

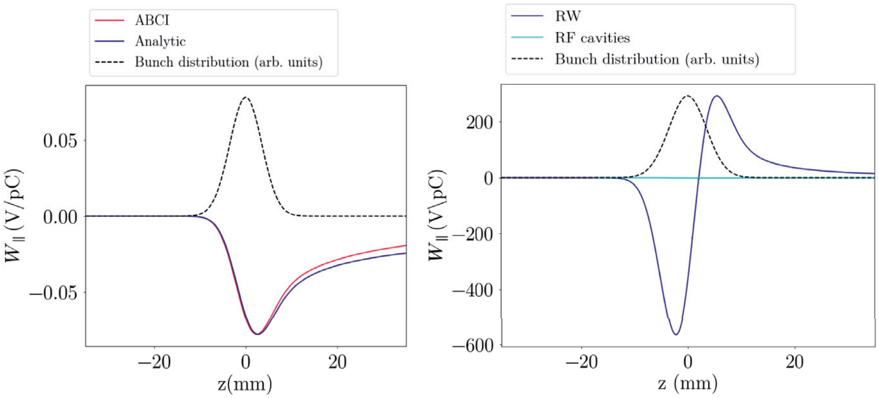

Figure 7.2: Left side: wake potential of a cavity for σ_z=3.5 mm given by the ABCI code and by Eq. 93. Right side: total wake potential due to RF cavities compared to the RW wake potential of 100 nm NEG coating for σ_z=3.5 mm.

The number and the design of these cells have been optimized for strong high order mode damping and low longitudinal loss factor [107, 108]. For a Gaussian bunch with a nominal RMS bunch length of 3.5 mm, the wake potential of one cavity given by the ABCI code [109] is shown in Fig 7.2 (left side). This result has been compared with the analytic wake potential at high frequencies of a cavity with attached tube corresponding to the fourth term of the Heifets-Bane broadband impedance model (see Eq. 39):

$$W_z(\tau) = \frac{\tilde{Z}_c}{2\sqrt{\sigma_\tau}}\sqrt{\frac{|\tau|}{\sigma_\tau}}\{I_{-\frac{1}{4}}(\mu) \pm I_{\frac{1}{4}}(\mu)\}e^{-\mu} \tag{93}$$

where $\mu = \left(\frac{\tau}{2\sigma_\tau}\right)^2$ and I_ν are the modified Bessel functions of fractional order. The parameter $\tilde{Z}_c$ depends on the geometry and has been obtained from ABCI by fitting the numerical wake potential to the analytic expression of Eq. 93. The same value of $\tilde{Z}_c$ has been considered to compute the analytic wake potential of a very short bunch ($\sigma_z = 0.35$ mm) to be used as input for PyHEADTAIL tracking simulations, as illustrated in the next section. ABCI wakefield simulations estimated a loss factor of 0.33 V/pC for each cavity. Figure 7.2 (right side) shows a comparison between the total wake potential due to RF cavities and the RW wake potential of a 100 nm NEG coating for a Gaussian bunch with σ_z = 3.5 mm: the contribution of cavities is negligible compared to the RW one.

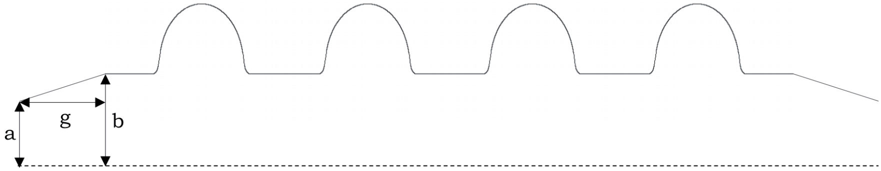

Figure 7.3: Sketch, not in scale, of a group of 4 cells with tapers.

These cavities will be arranged in groups of 4 cavities, as shown in Fig. 7.3, with two tapers at the ends. The taper-out corresponds to the transition from radius a = 50 mm outside the cryomodule to radius b = 150 mm inside the cryomodule and vice versa for the taper-in. For a fixed ratio $\frac{b}{a}$, the loss factor of a double taper depends on the taper length g, according to the formula [110]

$$k_{\parallel} = \frac{1}{2\pi\epsilon_0\sqrt{\pi}\sigma_z}(1-\tilde{\mu})\ln\left(\frac{b}{a}\right) \tag{94}$$

where $\tilde{\mu} = \min(1, \mu)$ and $\mu = \frac{g\sigma_z}{(b-a)^2}$. Figure 7.4 shows a comparison between the loss factors obtained by ABCI for different taper lengths with analytic estimations. For the FCC-ee impedance model, a taper length of $g = 0.5$ m has been chosen (see Fig. 7.5). ABCI simulations estimated an additional loss factor of 1.9 V/pC for a single double taper (in and out, considered independently). The wake potential of a single double taper is shown in Fig. 7.6 (left side) and compared to the RW contribution (right

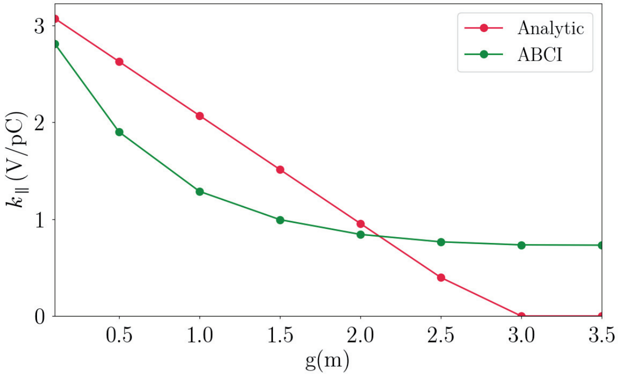

Figure 7.4: Longitudinal loss factor as a function of the taper length obtained from ABCI code (green dots) and analytically (red dots).

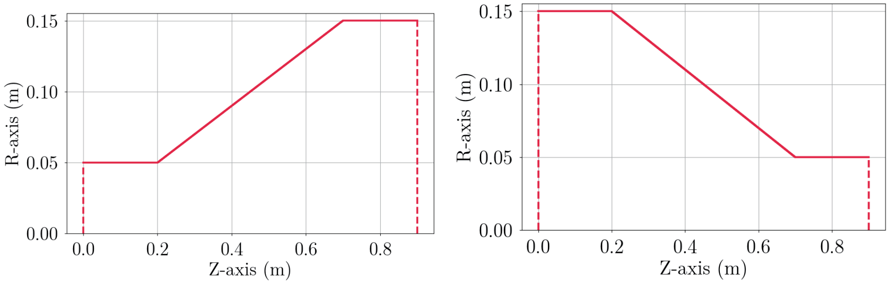

Figure 7.5: Tapers used in ABCI.

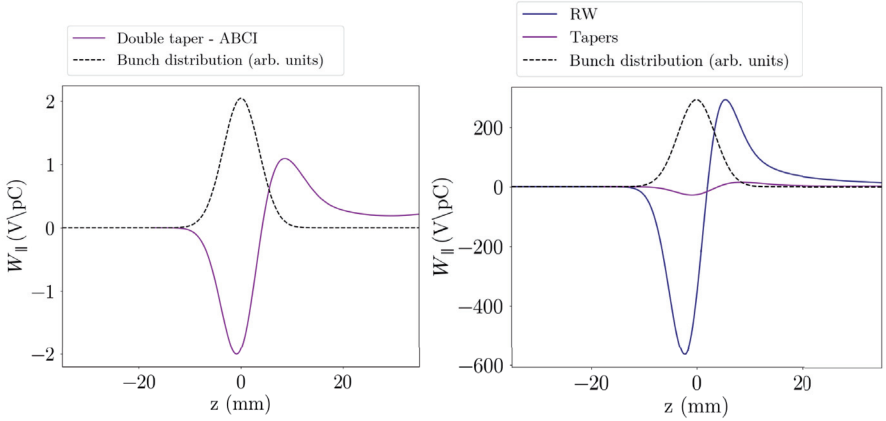

Figure 7.6: Wake potential of a double taper for σ_z=3.5 mm given by the ABCI code (left side) and total wake potential due to tapers compared to the RW wake potential of 100 nm NEG coating for σ_z=3.5 mm (right side).

side). In total, the loss factor for 14 4-cell cavities at 400 MHz with double tapers will be 45.1 V/pC.

7.1.2 *Synchrotron radiation absorbers*

SR represents an important source of heating and photoelectrons for the machine. In order to recover the lost energy, a sufficient number of RF cavities is needed together with SR absorbers to cope with extra heating and eventual background. Due to their large number, SR absorbers may represent a very important source of wakefields. Initially, as shown in Fig. 7.7, an elliptical vacuum pipe was proposed [111] with absorbers on

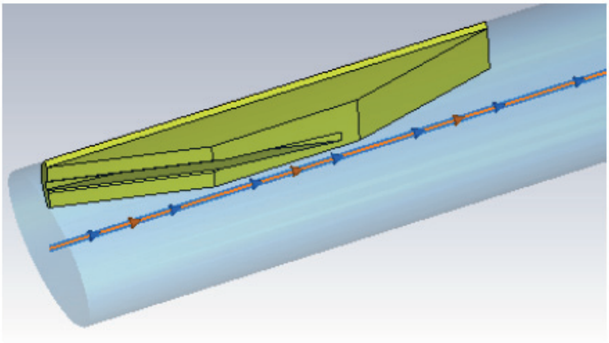

Figure 7.7: Elliptic vacuum chamber with one absorber insertion.

one side of the major semi-axis, for a total number of 9228 absorbers in the ring. Figure 7.8 shows the total wake potential due to 9228 absorbers for a 4 mm Gaussian bunch obtained from the CST code [112] and the total wake potential due to 10000 absorbers given by CST considering a new design that will be described in the following. Compared to the RW wake potential, one can observe that the contribution of absorbers is not acceptable. This is another reason why an elliptic beam pipe has not been considered, in addition to the tune shift produced by quadrupolar wakefields discussed in Section 5.1. The new proposed design shown in Fig. 7.9 takes into account the vacuum chamber shown in Fig. 4.13 with

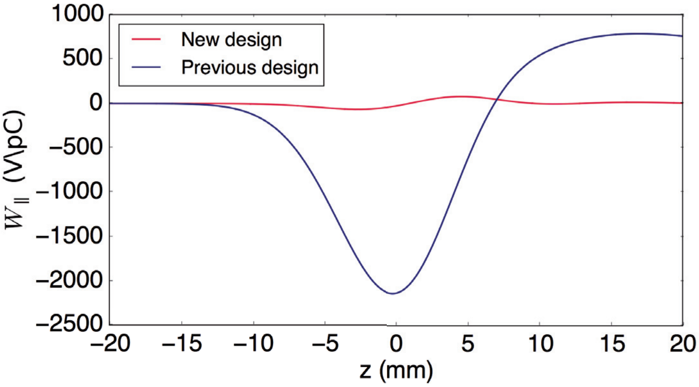

Figure 7.8: Longitudinal wake potential of a 4 mm Gaussian bunch produced by 9228 absorbers with elliptic chamber and 10000 absorbers with the new design.

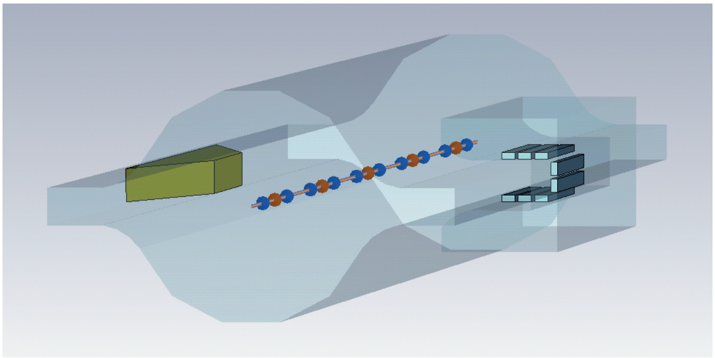

Figure 7.9: 3D model of the FCC-ee chamber and a SR absorber with pumping slots used for CST simulations.

35 mm radius and two rectangular antechambers on both sides. Absorbers will be then installed inside the chamber winglets every 4-6 meters, with the purpose of intercepting the radiation that, otherwise, would impact on the beam chamber. These metallic devices are shaped like a trapezoid, with a total length of 30 cm and placed at about 42.5 mm from the beam axis. Placing slots for vacuum pumps just in front of each absorber allows to efficiently capture the molecule desorption. The pumping slots have a racetrack profile, length of 100-120 mm and width of 4-6 mm. Behind the slots, a cylindrical volume and a flange will be installed to support a NEG pump. Numerical simulations of the beam chamber profile with one absorber insertion have been performed using CST. These impedance studies do not include pumping slots and pumps. Simulations show that below 3 GHz the longitudinal impedance is purely inductive, giving a longitudinal broadband impedance $\frac{Z}{n} \simeq 1m\Omega$ for 10000 absorbers in the ring.

7.1.3 *Collimators*

In order to suppress the background and to cut off the beam halo, a total number of 20 collimators (10 for each plane) are considered in this model, with a design very similar to those of PEP-II [113] and SuperKEKB [114]. 3D models used for CST simulations are shown in Fig. 7.10. By considering the minimum apertures of 5 mm and 2 mm for horizontal and vertical

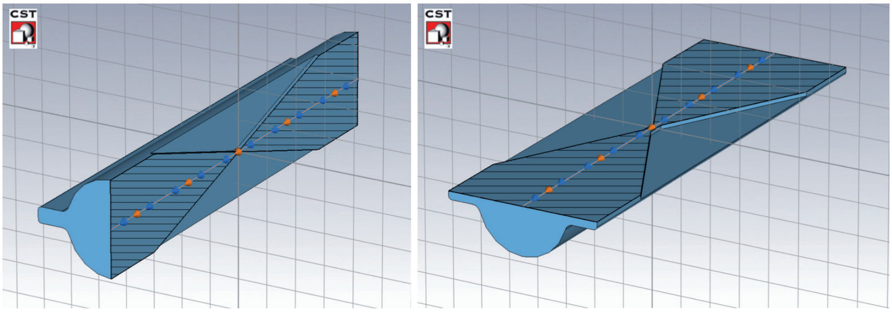

Figure 7.10: CST perspective view of the vertical collimator (left side) and top view of the horizontal one (right side).

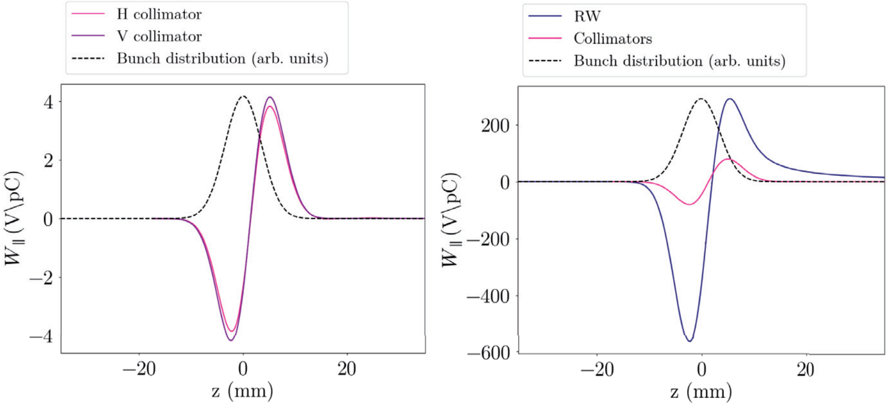

Figure 7.11: Wake potential of horizontal and vertical collimators given by CST (left side) and total wake potential due to collimators compared to the RW wake potential of 100 nm NEG coating (right side), for σ_z=3.5 mm.

collimators, respectively, the total loss factor is about 18.7 V/pC for the nominal RMS bunch length of 3.5 mm. Figure 7.11 shows the wake potential of horizontal and vertical collimators (left side) and the total wake potential due to collimators compared to the RW contribution (right side), for a Gaussian bunch with nominal RMS bunch length of 3.5 mm.

7.1.4 *Beam Position Monitors*

Diagnostic elements like four-button Beam Position Monitors (BPMs) are planned to be installed in the machine, for a total number of about 4000. The geometry shown in Fig. 7.12 (left side) has been optimized from the

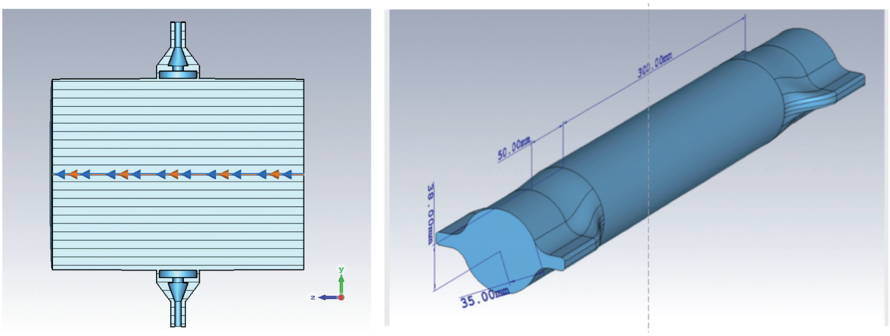

Figure 7.12: CST perspective view of the four-button BPM (left side) and CST model of the winglet-to-circular taper for BPM installation(right side).

impedance and heat transfer point of view [115]: the button has a diameter of 15 mm and a thickness of 3 mm. Moreover, in order to push the higher order modes trapped in the BPM structure to higher frequencies a BPM design with a conical button, similar to the one used in SIRIUS [116], is also being considered. Time domain simulations have been performed with CST, obtaining the wake potential shown in Fig. 7.13 for a single BPM and a total loss factor of about 40.1 V/pC for 4000 elements in the ring. Because of the particular shape of the vacuum chamber in the arcs, a special type of winglet-to-circular tapers shown in Fig. 7.12 (right side) was initially designed to install BPMs, for a total number of 4000 double

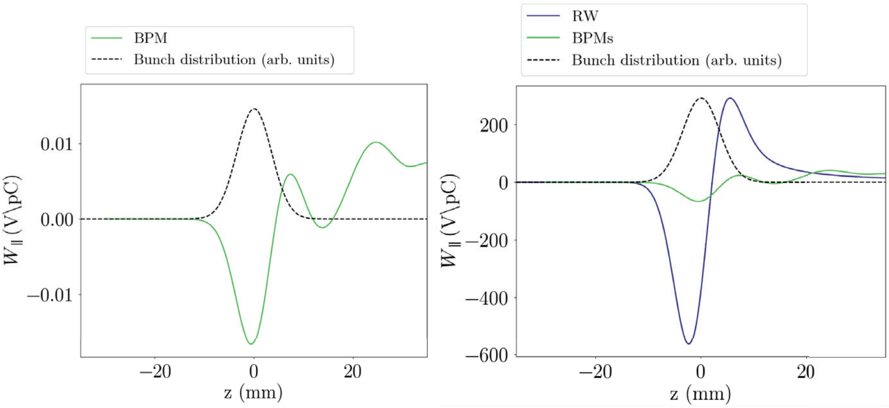

Figure 7.13: Wake potential of a BPM obtained from the CST code (left side) and total wake potential due to BPMs compared to the RW contribution of 100 nm NEG coating (right side), for σ_z=3.5 mm.

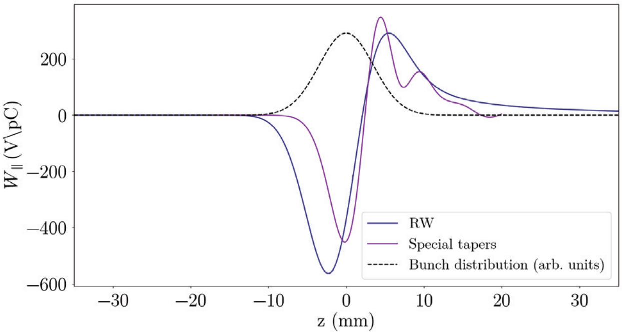

Figure 7.14: Longitudinal wake potential due to 4000 special tapers compared to the RW wake potential of 100 nm NEG coating (right side), for σ_z=3.5 mm.

tapers. As can be seen from Fig. 7.14, the contribution of these special tapers to the impedance budget is very large and comparable with the RW one. Therefore, BPMs will be installed directly on the beam pipe with a rotation angle of 45°.

7.1.5 *RF shielding*

In addition to the previous components, 8000 bellows with RF shield will be installed before and after each BPM. Since the conventional finger-type RF shielding shown in Fig. 7.15 (left side) showed a not negligible impedance contribution compared to the RW one [117] (red curve in Fig. 7.16), it was decided to use the comb-type bellows and flanges similar to those

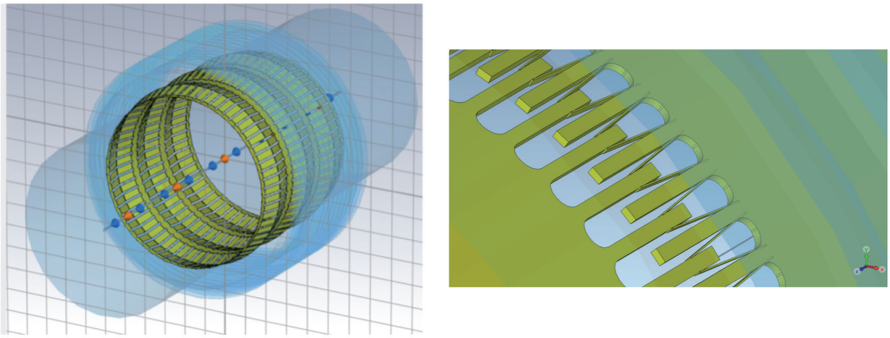

Figure 7.15: Conventional finger-type RF shielding (left side) and inside view of the new comb-type bellows with small fingers between the teeth (right side).

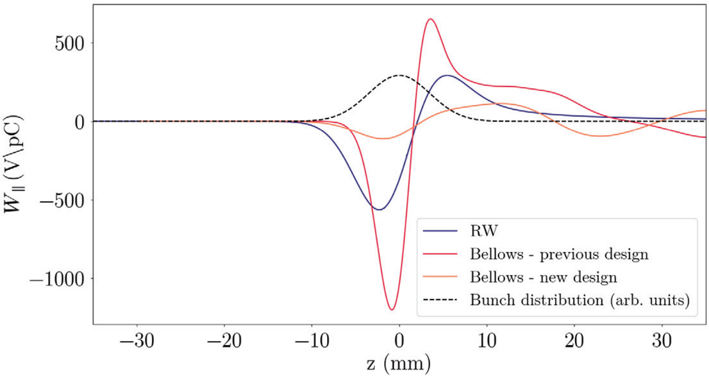

Figure 7.16: Wake potential of conventional finger-type RF shielding (in red) and new comb-type bellows (in orange) compared to the RW one (in blue) for 3.5 mm RMS bunch length obtained from the CST code.

of SuperKEKB [118] shown in Fig. 7.15 (right side). In this case, the RF shielding consists of nested teeth with 10 mm length, 1 mm width, 0.5 mm radial thickness and 2.14 mm gap between adjacent teeth, corresponding to a gap of 0.57 mm between the nested teeth. This design also includes small fingers to ensure electrical contacts. The total loss factor of the bellows has been computed using CST and found to be about 49 V/pC for 8000 elements.

7.2 LONGITUDINAL IMPEDANCE BUDGET

As illustrated in the previous section, the contribution of all the current machine components to the longitudinal impedance budget has been evaluated by means of ABCI and CST simulations in time domain for a Gaussian bunch with nominal bunch length of $\sigma_z = 3.5$ mm.

Figure 7.17 shows the longitudinal wake potentials of each component compared to the RW contribution of a 100 nm NEG coating, computed analytically as the convolution between the wakefield obtained from ImpedanceWake2D and a 3.5 mm Gaussian bunch.

Table 7 summarizes the corresponding loss factors. The major contribution to the machine impedance is given by the RW with a total loss factor at nominal intensity and bunch length of 210 V/pC. The total dissipated power at nominal intensity is 13.6 MW, about a factor 3.7 smaller than the

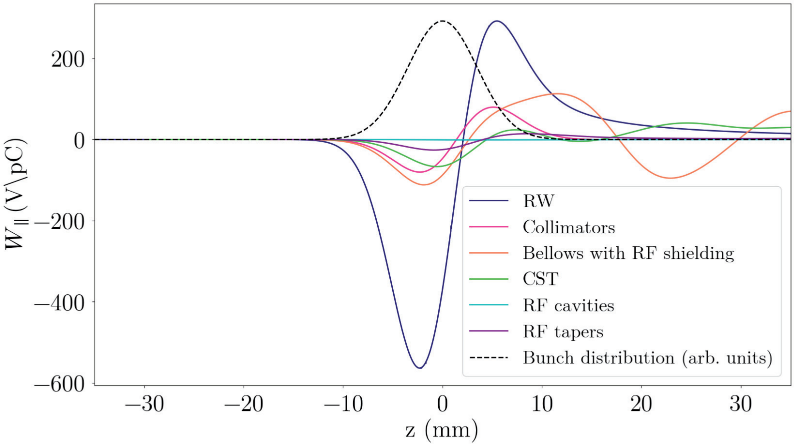

Figure 7.17: Longitudinal wake potentials for a Gaussian bunch with nominal bunch length $\sigma_z = 3.5mm$ due to the main FCC-ee components compared with the RW contribution (blue line).

Component	**Number**	$k_{loss}[V/pC]$	$P_{loss}[MW]$
Resistive wall	97.75km	210	7.95
Collimators	20	18.7	0.7
RF cavities	56	18.5	0.7
RF double tapers	14	26.6	1.0
BPMs	4000	40.1	1.5
Bellows	8000	49.0	1.8
Total		**362.9**	**13.7**

Table 7: Power loss contribution of the main FCC-ee components at nominal intensity and bunch length, in the lowest energy case of 45.6 GeV.

total SR power dissipated by the beam of 50 MW. However, this value of power loss is expected to be lower due to the bunch lenghtening effect.

As for the RW beam dynamics studies presented in Section 5.3, the wake potential of a bunch with $\sigma_z = 0.35$ mm has been used as Green function for PyHEADTAIL tracking simulations. For each component, Fig. 7.18 shows the wake potential obtained from ImpedanceWake2D, ABCI and CST codes for a Gaussian bunch with nominal RMS bunch length of 3.5 mm compared to the wake potential obtained from PyHEADTAIL as solution of the convolution integral of Eq. 16.

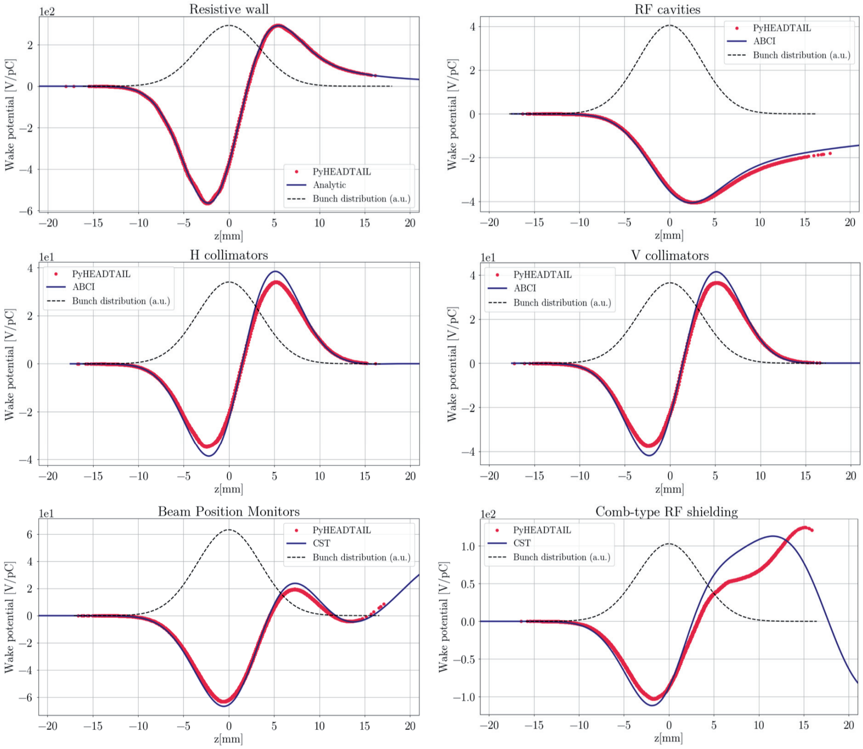

Figure 7.18: Comparison of the longitudinal wake potentials of a 3.5 mm Gaussian bunch obtained from ImpedanceWake2D, ABCI and CST codes with the wake potentials obtained from PyHEADTAIL as convolution between the longitudinal bunch distribution and the wake potential of a 0.35 mm Gaussian bunch for each component.

The bunch lengthening and the MI threshold have been evaluated by considering all the current machine components and a 100 nm NEG film. The instability threshold in the longitudinal plane is about $2.5 \cdot 10^{11}$, a factor of 1.5 larger than the nominal bunch intensity and about 25% smaller than the one due to RW only. The threshold is much higher if the effect of BS is included, as shown in Fig. 7.20, where the energy spread remains constant at least up to $5 \cdot 10^{11}$. Moreover, at nominal intensity the bunch lengthening in presence of BS amounts to only 7% whereas without BS the bunch length is twice the nominal value (about 25% larger than the one due to RW only).

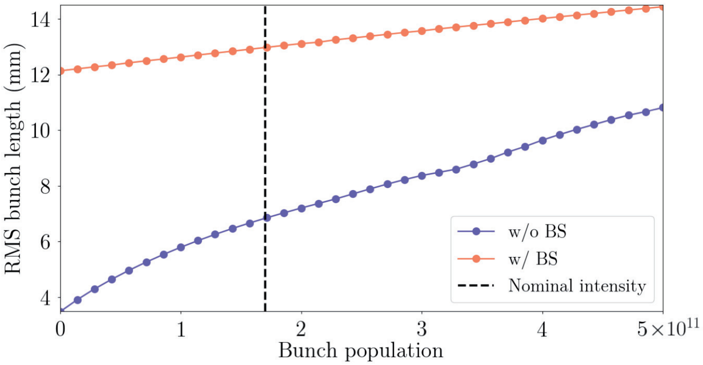

Figure 7.19: RMS bunch length as a function of the bunch population with (orange curve) and without (blue curve) beamstrahlung, given by numerical simulations by considering the impedance contribution of all the machine components.

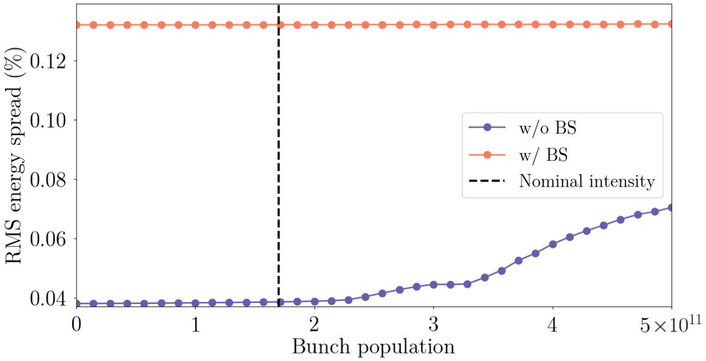

Figure 7.20: RMS energy spread as a function of the bunch population with (orange curve) and without (blue curve) beamstrahlung, given by numerical simulations by considering the impedance contribution of all the machine components.

8

IMPEDANCE STUDIES IN THE INTERACTION REGION

The IR is the region of the accelerator where particle detectors are hosted for the analysis of the collisions. Since the high physics potential of FCC-ee can be reached only if its design luminosity is achieved, it follows that the design of the detectors and in general of the IR (including background and radiation that can affect the detector performance) is an essential study for a new collider. In 2016, a Machine Detector Interface (MDI) working group has been established for FCC-ee as bridge between the accelerator and physics studies. The main task was to study the machine elements in the IR and the detectors able to produce and digest the very high luminosities expected for FCC-ee. This chapter is focused on impedance studies for the IR of FCC-ee, with an evaluation of the power loss due to geometrical and RW impedances and trapped modes. A sketch of the IR is shown in Fig. 8.1 [119]. Its length (from the IP to the first quadrupole QC1) is about 2.2 m and the final focusing quadrupoles are superconducting magnets. A

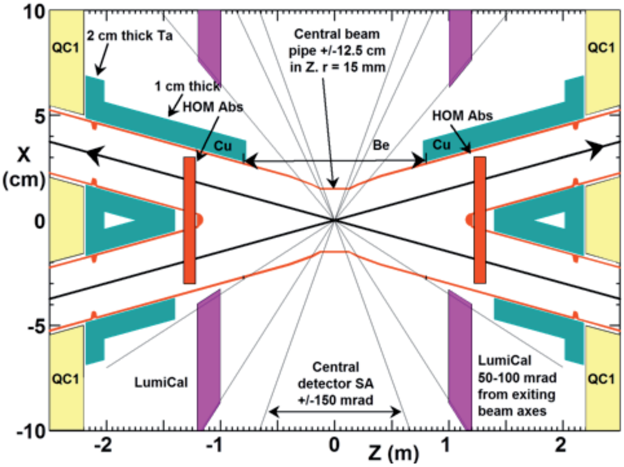
10
5
0
-5
-10
X (cm)
-2
-1
0
Z (m)
1
2
QC1
QC1
QC1
QC1
2 cm thick Ta
1 cm thick HOM Abs
HOM Abs
Cu
Cu
Be
Central beam pipe +/-12.5 cm in Z. r = 15 mm
LumiCal
Central detector SA +/-150 mrad
LumiCal 50-100 mrad from exiting beam axes

Figure 8.1: Layout of the IR (expanded horizontal scale).

compensating solenoid for the detector magnetic field is located from 1.25 m to 2.2 m from the IP on both sides and just in front of each solenoid there is a luminosity calorimeter to measure the collision luminosity (LumiCal). The two beams circulate in two separate beam pipes which merge into a single vacuum chamber around the IP. The crab-waist collision scheme has been chosen to reach the highest possible luminosity, with a crossing angle of 30 mrad. The central beam pipe is circular with 15 mm radius, as well as the entering and exiting beam pipes through the QC1 quadrupole. In QC2 quadrupole the beam pipe radius increases to 20 mm and it becomes 30 mm outside QC2. The beam pipe is made of copper, possibly NEG coated for electron cloud mitigation, as explained in Section 4.5. However, the beam pipe of the central region (±0.9 m from the IP), is made of Beryllium (Be), a low-Z material to minimize interactions between particles and beam pipe.

8.1 IP RESISTIVE WALL IMPEDANCE

Assuming a 15 mm radius pipe made of 1.2 mm thick beryllium at ±90 cm from IP and 2 mm thick copper elsewhere, Fig. 8.2 shows the corresponding RW longitudinal impedances.

Let us consider a Gaussian bunch with distribution

$$\lambda(z) = \frac{N_p}{\sqrt{2\pi}\sigma_z} e^{-\frac{z^2}{2\sigma_z^2}} \xrightarrow{\mathscr{F}} \Lambda(\omega) = N_p e^{-\frac{\omega^2\sigma_z^2}{2c^2}} \tag{95}$$

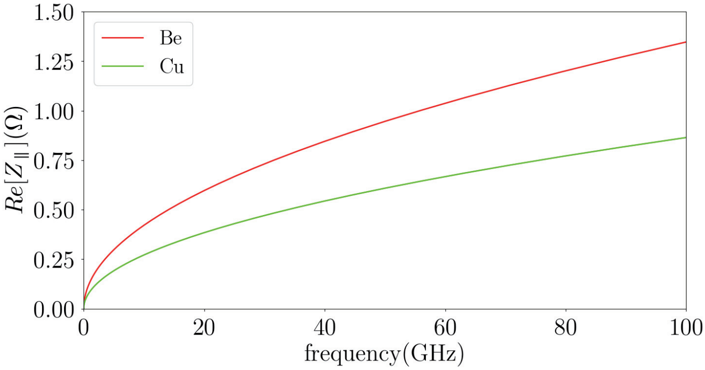

Figure 8.2: Longitudinal RW impedance for copper and beryllium.

For a circular resistive pipe with radius b and conductivity σ_c, the power loss per unit length can be obtained by substituting Eqs. 71 and 95 in Eq. 24 [120]:

$$\frac{P_{loss}}{L} = \frac{1}{t_0} \frac{N_p^2 e^2 c}{4\pi^2 b \sigma_z^{\frac{3}{2}}} \sqrt{\frac{Z_0}{2\sigma_c}} \Gamma\left(\frac{3}{4}\right) N_b \tag{96}$$

where Z_0 is the vacuum impedance and $\Gamma\left(\frac{3}{4}\right) \simeq 1.225$.
By applying Eq. 96 (or, equivalently, Eq. 24) for a Gaussian bunch with nominal RMS bunch length $\sigma_z = 3.5$ mm, the power loss is about 526 W for the copper pipe ($\sigma_{Cu} = 5.9 \cdot 10^7 \frac{S}{m}$) and 560 W for the beryllium pipe ($\sigma_{Be} = 2.5 \cdot 10^7 \frac{S}{m}$), for a total power loss in the IR due to RW of about 1 kW.

8.2 SR MASKS

As shown in Fig. 8.1, SR masks are placed at ±2.1 m, before and after each quadrupole, in order to protect the vacuum chamber and the detector from photons generated by the last bending magnet located 100 m from the IP. These masks are 2 cm long with a 1 cm long ramp back to the larger radius at each end and produce a variation of 2 mm in the pipe radius, from 15 mm to 13 mm in QC1 and from 20 mm to 18 mm in QC2, as shown in Fig. 8.3. Numerical simulations with the ABCI code indicate a power loss of about 3.8 W per bunch at the design intensity on the Z resonance.

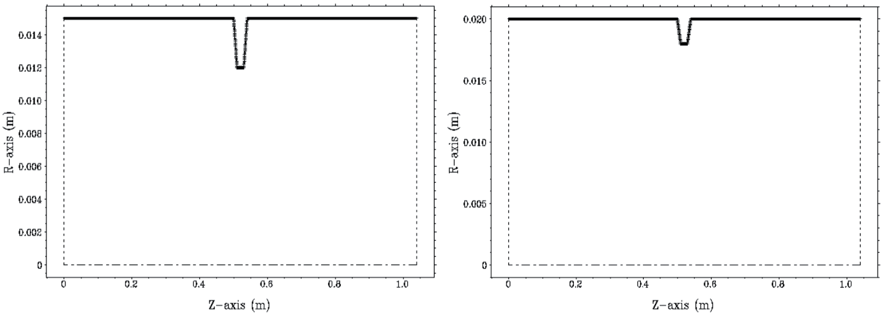

Figure 8.3: SR masks in QC1 quadrupole (left side) and QC2 quadrupole (right side) used for ABCI simulations.

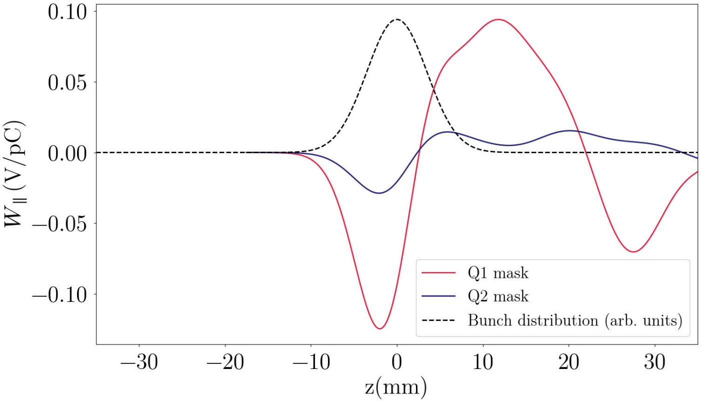

Figure 8.4: Wake potential of a σ_z = 3.5 mm bunch given by SR masks obtained from the ABCI code.

Figure 8.4 shows the corresponding wake potentials for a Gaussian bunch with nominal RMS bunch length σ_z= 3.5 mm.

8.3 AN UNAVOIDABLE TRAPPED MODE

As illustrated before, in FCC-ee the colliding beams have different incoming and outgoing beam pipes which are combined into one pipe near the collision point. This variation in the beam pipe geometry can unintentionally generate cavities and the beams generate electromagnetic fields with frequencies below the cutoff frequency of the beam pipe that therefore cannot propagate and remain localized near the discontinuity. The cutoff frequency is determined by the pipe geometry. For a round pipe with radius b, the cutoff frequencies of the longitudinal TM_{01} and transverse TE_{11} modes are given by, respectively:

$$f^{co}_{TM_{01}} = \frac{c}{2\pi}\frac{\nu_{01}}{b} \tag{97}$$

$$f^{co}_{TE_{11}} = \frac{c}{2\pi}\frac{\mu_{11}}{b} \tag{98}$$

with ν_{01} = 2.4048 and μ_{11} = 1.8412. In the IR of FCC-ee, the radius of the incoming and outgoing pipes is 15 mm, corresponding to cutoff frequencies of $f^{co}_{TM_{01}}$ =7.65 GHz and $f^{co}_{TE_{11}}$ =5.86 GHz.

A trapped mode can be modeled as a narrowband resonator (see Eq. 38) characterized by a resonant frequency, a shunt impedance and a quality factor. If this mode has a longitudinal electrical component collinear with the particle velocity, it can interact with the beam. Moreover, if it has a large quality factor and its frequency is in resonance with the frequency of some of the revolution harmonics, then the local heating in the IR can reach tens of kW. The other electromagnetic waves excited by the beam with a frequency above the cutoff will propagate through the beam pipe away from the IR, depositing heat elsewhere. The energy loss of the beams in the IR can be a very critical aspect, causing an increase of the temperature of the vacuum chamber and vacuum degradation. If the IR chamber has small gaps or hidden cavities (like in shielded bellows or valves), then electric sparks or arcing may cause additional vacuum spikes. Heating of NEG films (if used in the IR) may cause instabilities, due to a temperature above the recovery level. A more detailed description of all these effects can be found in [121, 122]. Detuning, i.e. changing the mode frequency such that it is not equal to any harmonics of the revolution frequency, and the suppression of the loaded quality factor seem to be the only ways to decrease the HOM heating power. However during the design of the IR these effects can be reduced by making the geometry of the IR very smooth, thus reducing the number of trapped HOMs. In trying to find an optimum geometry, an unavoidable trapped mode has been identified which remains even in a very smooth pipe and it is mainly due to the geometry of the connection of the two pipes. The structure of this mode has been analysed in the different IR models by means of electromagnetic simulations and a solution has been proposed.

8.3.1 *Wave excitation in the IR*

Fig. 8.5 shows the electric field line distribution obtained from the NOVO code [123] right after the passage of a bunch through the beam pipe connection. One can observe that the bunch has extended its self-field into the larger common pipe, a fraction of the field propagates back into the other pipe and another fraction is reflected back into the original beam pipe. An image charge also appears at the edge of the pipe connection. This charge (and later the image current running across the chamber) produces

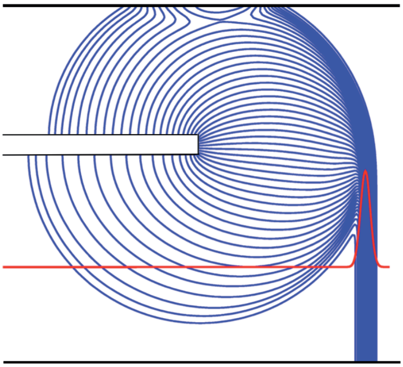

Figure 8.5: Electric force field line distribution at the time when a relatively short bunch has just passed a pipe connection. The red line shows the bunch line charge density distribution and the bunch trajectory.

electromagnetic fields in both pipes which propagate from the edge of the pipe connection to the common central pipe of the IR and chase the bunch. It is important to note that a shorter bunch excites higher frequency fields, which may propagate in the pipe. Figure 8.6 shows the electric force line distribution obtained from NOVO when a bunch has passed the outgoing pipe connection. In this plot, green and blue lines represent force lines with opposite direction.

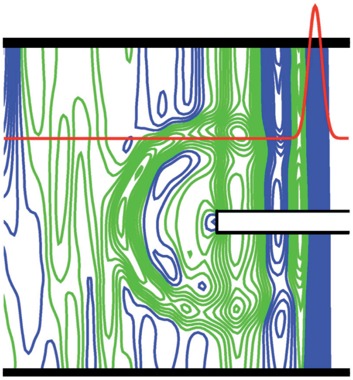

Figure 8.6: Electromagnetic field line distribution at the time when a short bunch has passed the outgoing pipe connection. Green and blue lines represent force lines with opposite directions. The red line shows the bunch line charge density distribution and the bunch trajectory.

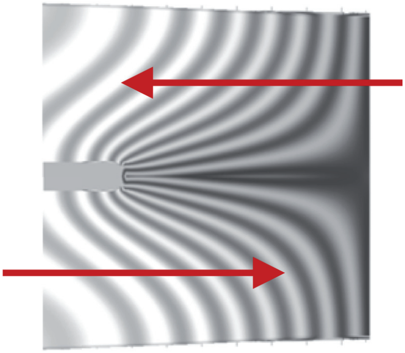

Figure 8.7: Electric field line distribution of the trapped mode. The red arrows show the direction of the colliding beams.

8.3.2 *Structure of the unavoidable trapped mode in the IR*

In trying to find an optimal geometry for the IR with minimum electromagnetic wave resonance excitation, one mode has been identified which remains even in a very smooth geometry. This mode is localised near the connection of the two incoming and outgoing pipes. The electric field distribution is shown in Fig. 8.7. The cutoff frequency of the incoming pipes is much higher than the mode frequency and this results in a trapped mode. One can observe from Fig. 8.7 that this mode has both transverse and longitudinal components and it can be easily excited by the colliding beams, especially when the two beams travel close to the pipe connection. The transverse kicks in the incoming and outgoing pipe connections compensate each other.

8.3.3 *HOM analysis*

In order to reduce the HOM effects, the geometry of the beam pipe has been optimized from the impedance point of view. In these studies, three different models of the IR have been considered, by assuming the same diameter of the incoming pipes and a 15 mm radius central pipe. CST simulations in time domain were performed for each model to find the resonances in the spectrum of the wake potential. Then CST eigenmode simulations were performed in the frequency region around these resonances

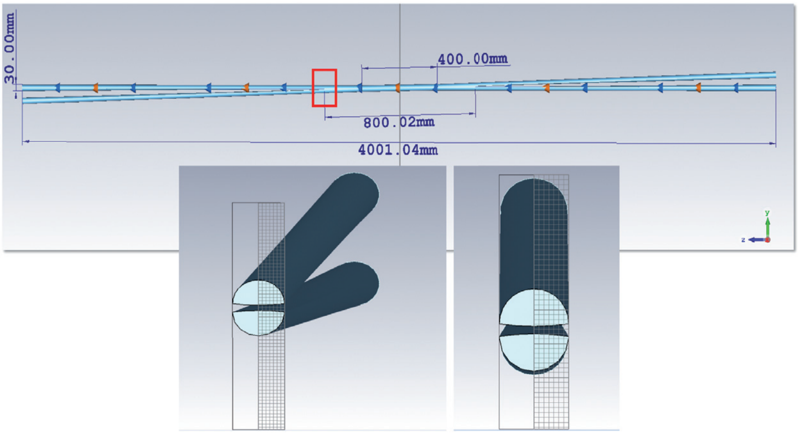

Figure 8.8: Geometry of the IR model 1.

in order to confirm the presence of this mode and to analyse its structure. For these studies, a Gaussian bunch with bunch length $\sigma_z = 2.5$ mm has been considered.

Model 1: squeezed incoming pipes

In this model, the incoming pipes are smoothly squeezed to a half circle shape in order to merge into the central pipe with a constant diameter, as shown in Fig. 8.8. The length of the central beam pipe is 400 mm and the diameter is 30 mm. Figure 8.9 shows the wake potential for a 2.5 mm Gaussian bunch obtained from CST (left side) and the the spectrum obtained as Fourier transform of the wake potential (right side), indicating a trapped mode around 5.8 GHz. CST eigenmode simulations in the frequency region

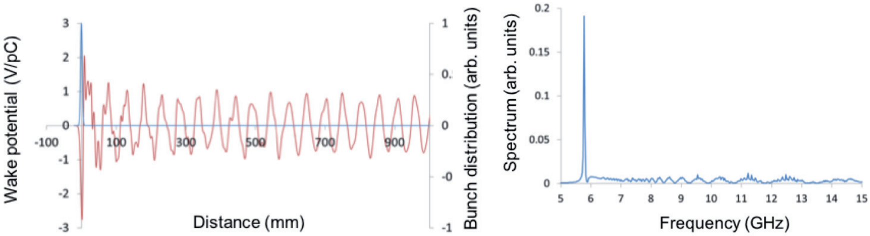

Figure 8.9: Wake potential of a 2.5 mm bunch and spectrum of the excited field in the IR model 1.

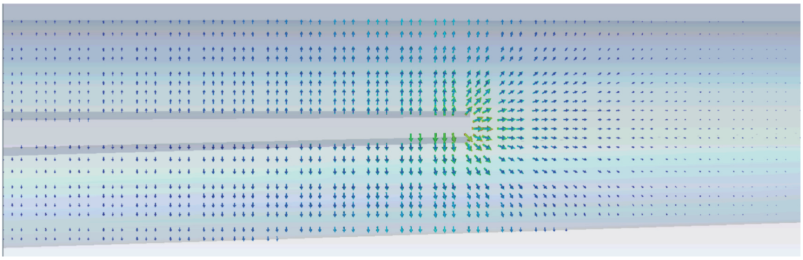

Figure 8.10: Electric field line distribution for the trapped mode in Model 1.

of 5-7 GHz confirmed a resonance mode at 5.774 GHz, with the electric field line distribution shown in Fig. 8.10.

Model 2: small sharp transition

In the second IR model, the incoming pipes near the connection are circular pipes while the central chamber has a 0.82 m long transition to an approximately elliptical or racetrack shape at both sides. The CST model is shown in Fig. 8.11. Wakefield and eigenmode simulations have been performed with the CST code and only one trapped mode has been found at the frequency of 5.67 GHz, with a structure very similar to the previous one. The spectrum is shown in the lower right plot of Fig. 8.11.

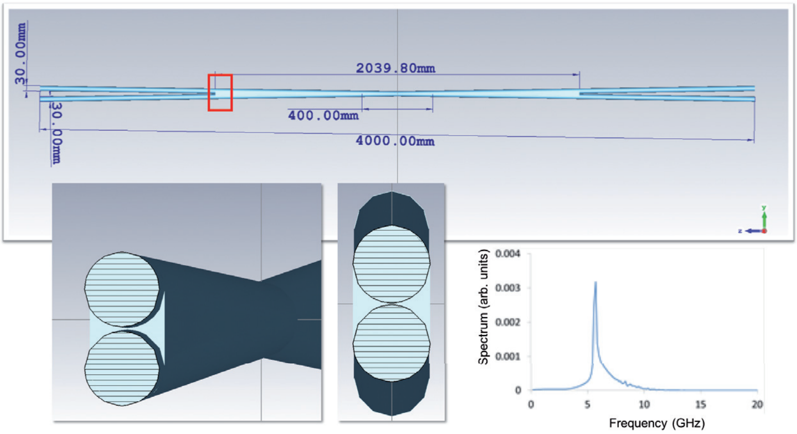

Figure 8.11: Geometry of the IR Model 2 and spectrum of the excited fields.

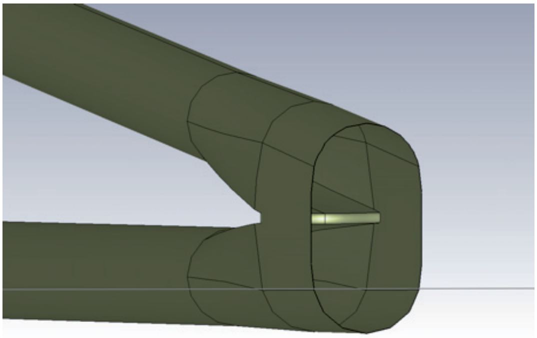

Figure 8.12: Inside and outside view of the transition in the IR model 3.

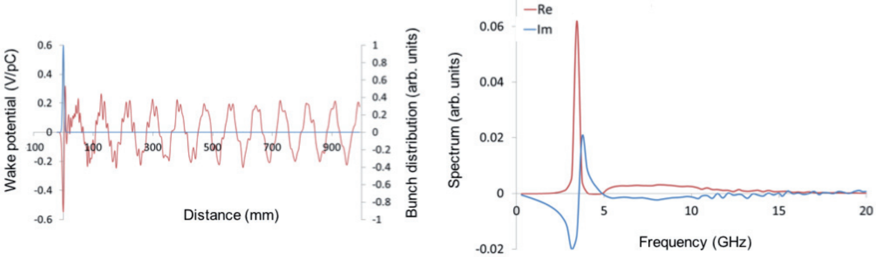

Figure 8.13: Wake potential of a 2.5 mm bunch and spectrum of the excited field in the IR model 3.

Model 3: smooth geometry

The very smooth geometry of Model 3, built in CATIA [124] and then imported in CST as a CAD file, is shown in Fig. 8.12. The calculated wake potential of a 2.5 mm bunch and the corresponding spectrum are shown in Fig. 8.13. The frequency and the amplitude of the trapped mode in model 3 are two times and four times lower, respectively, than the values found for the trapped mode of model 1, showing a lower impedance compared to the impedance of model 1. The electric field line distribution of the trapped mode obtained from CST is shown in Fig. 8.14.

8.3.4 *HOM absorber concept*

The last design has a smooth geometry of the IR vacuum chamber, characterized by only one trapped mode and a smaller HOMs impedance compared

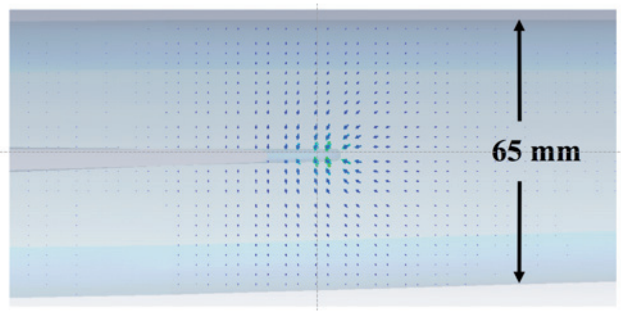

Figure 8.14: Electric field line distribution for the trapped mode in Model 3.

to the other designs. However, the power of this mode can be very dangerous in the IR, requiring the design of HOMs absorbers. Since the electric field lines of the mode in the two incoming pipes are perpendicular to the beam trajectory, longitudinal slots can be machined in the top and bottom walls of the pipes (see Fig. 8.15). This allows the mode field to easily propagate through these slots and be absorbed by a water-cooled absorber installed above and below the slots. A sketch of the IR with the geometry of Model 3 together with HOMs absorbers is shown in Fig. 8.15. This represents a good starting point, nevertheless more studies are needed for a further optimization.

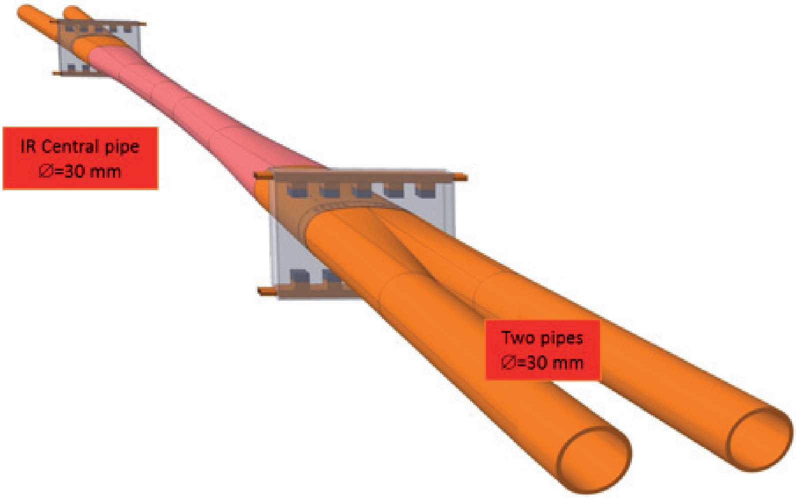

Figure 8.15: IR smooth geometry with HOM absorbers.

9

CONCLUSIONS

The European Strategy for Particle Physics requested an ambitious post-LHC accelerator project to ensure a worldwide particle physics programme after LHC. In the framework of the Future Circular Collider study, the high luminosity electron-positron collider FCC-ee will allow very precise measurements of all known heavy particles. The research activity presented in this Ph.D. thesis analyzed some important limitations for the operation of this machine, i.e. electron cloud and collective effects, particularly critical on the Z resonance due to the low energy and the high beam current.

Electron cloud build up simulations have been performed for the main elements of the machine, in both the arcs and the IR. Multipacting thresholds and heat load have been evaluated for each component for different bunch spacings of 2.5, 5, 15 ns, indicating that with a low SEY coating (SEY$\leq$1.2) the 15 ns beam is the preferable option to suppress the EC build up in the IR and to have a lower heat load in the arcs. This coating is also needed to cope with the EC induced single bunch head tail instability, whose electron density threshold on the Z resonance is quite low (about $2.29 \cdot 10^{10}/m^3$). These results have been achieved thanks to the development of simulation tools in the PyECLOUD code that extended its validity range. In particular, a multigrid solver has been implemented in the PyPIC library of PyECLOUD to refine the resolution around the beam location, thus improving the code accuracy and computational time.

An impedance model was also developed, through the characterization and optimization of the impedance of some important machine components. This model was crucial for a better understanding of single bunch and multi bunch instabilities, thus allowing to identify adeguate mitigation techniques for ensuring beam stability during operation.

Special attention has been given to the RW impedance associated with a layer of NEG coating of the vacuum chamber required for EC mitigation. The analytical and numerical studies presented in Chapter 5 showed that for FCC-ee the RW beam coupling impedance plays a crucial role affecting both the parameters choice and some design solutions of the 100 km collider. In particular, a vacuum chamber with a round cross section has been preferred to an elliptic pipe in order to avoid the strong betatron tune shift with beam current due to quadrupolar RW wakefields. The work presented in this thesis demonstrated analytically and numerically that for the FCC-ee beam parameters on the Z resonance the RW impedance mainly depends on the thickness of NEG coating and only marginally on its conductivity. It followed that the RW contribution to the impedance budget can be reduced by decreasing the thickness of this layer. In order to operate at nominal bunch intensity below the single bunch microwave instability threshold, a film with thickness below 200 nm is recommended. The TMCI instability threshold due to the RW is less critical, but still dangerous, being a factor of about 2.6 higher than the nominal bunch intensity.

The power loss due to the RW impedance is also not negligible, representing about 7% of the total losses due to SR. Moreover, the interaction of the beam with the vacuum chamber resistive walls results in a synchrotron tune reduction and a large incoherent synchrotron tune spread. Both these effects can influence the beam-beam performance shifting the collider working point and affecting the incoherent beam-beam resonances. The transverse coupled bunch instability driven by the RW impedance is very fast with a rise time of a few revolution turns, thus requiring a robust and novel feedback system to suppress the instability.

An extensive measurement campaign was performed at CERN to characterize NEG thin films at different thicknesses and to analyse their performance in terms of activation and SEY. The minimum effective thickness for NEG activation was examined using XPS. The reduced activation performance is due to elevated concentrations of oxygen especially in the thinner films. The thinnest sample of 30 nm was able to digest O and C, however after four short activation cycles of 4 hours it was unable to activate effectively and this led to a high maximum SEY of 1.5. Longer activation cycles of 24 hours extended the effective lifetime of the 30 nm film, leading to better activation and a lower SEY of 1.21 after the fourth cycle. Numerical simulations and experimental results indicated that a film thickness between 100 nm and 200 nm balancing the limitations of activation and impedance is a good candidate for coating thickness. Further experimental investigation is recommended for SEY, PSD and pumping speed with a larger number of activation cycles.

Besides the RW, the geometric impedance of important machine components has been evaluated, showing that the contribution of these elements is up to 5 times smaller than that of RW. The MI threshold is around $2.5 \cdot 10^{11}$, about a factor 1.5 higher than the nominal bunch intensity. Operation with BS, i.e. operation with colliding beams, will increase the instability thresholds in both planes, due to a larger bunch length and higher energy spread.

Impedance studies in the IR estimated a total power loss of about 1 kW due to RW and a power loss of about 3.8 W per bunch due to SR masks. CST simulations in both time and frequency domain were performed to study HOMs in the IR, showing an unavoidable trapped mode around the connection of the two beam pipes. A smooth geometry of the IR vacuum chamber has been designed, characterized by a low impedance and the presence of one trapped mode. Dedicated water-cooled HOMs absorbers with longitudinal slots have been conceived. However, further studies are needed for their optimization.

Several journal papers [125–127] and proceedings [34, 90, 117, 128–135] have been extracted from this Ph.D. thesis work.

These studies have also been published in the FCC Conceptual Design Report [9].

BIBLIOGRAPHY

[1] O. Brüning, P. Collier, P. Lebrun, S. Myers, R. Ostojic, J. Poole, and P. Proudlock, "LHC Design Report, volume 1: the LHC Main Ring," Tech. Rep. CERN-2004-003-V-1, CERN, Geneva, Switzerland, 2004.

[2] G. Aad, T. Abajyan, B. Abbott, J. Abdallah, S. A. Khalek, A. Abdelalim, O. Abdinov, R. Aben, B. Abi, M. Abolins, *et al.*, "Observation of a new particle in the search for the Standard Model Higgs boson with the ATLAS detector at the LHC," *Physics Letters B*, vol. 716, no. 1, pp. 1–29, 2012.

[3] S. Chatrchyan, V. Khachatryan, A. Sirunyan, A. Tumasyan, W. Adam, T. Bergauer, M. Dragicevic, J. Erö, C. Fabjan, M. Friedl, *et al.*, "Observation of a new boson with mass near 125 GeV in pp collisions at $\sqrt{s} = 7$ and 8 TeV," *Journal of High Energy Physics*, vol. 2013, no. 6, p. 81, 2013.

[4] `http://hilumilhc.web.cern.ch/`.

[5] G. Apollinari, I. Béjar Alonso, O. Brüning, M. Lamont, and L. Rossi, "High-Luminosity Large Hadron Collider (HL-LHC): Preliminary Design Report," Tech. Rep. CERN-2015-005, CERN, Geneva, Switzerland, 2015.

[6] `https://fcc.web.cern.ch`.

[7] M. Benedikt and F. Zimmermann, "Towards future circular colliders," *Journal of the Korean Physical Society*, vol. 69, no. 6, pp. 893–902, 2016.

[8] M. Benedikt, J. Wenninger, D. Schulte, and F. Zimmermann, "Challenges for highest energy circular colliders," in *Proceedings of IPAC'14, Dresden, Germany*, pp. 1–6, 2014.

[9] M. Benedikt *et al.*, "Future Circular Collider Study Volume 2: The Lepton Collider (FCC-ee) Conceptual Design Report," Tech. Rep.

CERN-ACC-2018-0057, CERN, Geneva, Switzerland, 2018. Submitted for publication to Eur. Phys. J. ST.

[10] A. Blondel and F. Zimmermann, "A High Luminosity e^+e^- Collider in the LHC tunnel to study the Higgs Boson," *arXiv preprint arXiv:1112.2518*, 2011.

[11] T. Behnke, J. E. Brau, B. Foster, J. Fuster, M. Harrison, J. M. Paterson, M. Peskin, M. Stanitzki, N. Walker, and H. Yamamoto, "The International Linear Collider Technical Design Report-Volume 1: Executive Summary," Tech. Rep. CERN-ATS-2013-037, CERN, Geneva, Switzerland, 2013.

[12] L. Evans and S. Michizono, "The International Linear Collider Machine Staging Report 2017," Tech. Rep. CERN-ACC-2017-0097, CERN, Geneva, Switzerland, 2017.

[13] M. Aicheler, P. Burrows, M. Draper, T. Garvey, P. Lebrun, K. Peach, N. Phinney, H. Schmickler, D. Schulte, and N. Toge, "A Multi-TeV linear collider based on CLIC technology: CLIC Conceptual Design Report," Tech. Rep. CERN-2012-007, CERN, Geneva, Switzerland, 2012.

[14] M. Boland, U. Felzmann, P. Giansiracusa, T. Lucas, R. Rassool, C. Balazs, T. Charles, K. Afanaciev, I. Emeliantchik, *et al.*, "Updated baseline for a staged Compact Linear Collider," Tech. Rep. CERN-2016-004, CERN, Geneva, Switzerland, 2016.

[15] A. Blondel, M. Zanetti, M. Koratzinos, and F. Zimmermann, "LEP3: A high luminosity e^+e^- collider in the LHC tunnel to study the Higgs boson," Tech. Rep. CERN-ATS-2012-235, CERN, Geneva, Switzerland, 2012.

[16] J. Gao, "CEPC-SPPC accelerator status towards CDR," *International Journal of Modern Physics A*, vol. 32, no. 34, p. 1746003, 2017.

[17] K. Oide, M. Aiba, S. Aumon, M. Benedikt, A. Blondel, A. Bogomyagkov, M. Boscolo, H. Burkhardt, Y. Cai, A. Doblhammer, *et al.*, "Design of beam optics for the future circular collider e^+e^- collider

rings," *Physical Review Accelerators and Beams*, vol. 19, no. 11, p. 111005, 2016.

[18] A. Bogomyagkov, E. Levichev, and D. Shatilov, "Beam-beam effects investigation and parameters optimization for a circular e+ e- collider at very high energies," *Physical Review Special Topics-Accelerators and Beams*, vol. 17, no. 4, p. 041004, 2014.

[19] Y. Papaphilippou, F. Zimmermann, L. Rinolfi, M. Aiba, D. Shwartz, and K. Oide, "Design Guidelines for the Injector Complex of the FCC-ee," in *Proceedings of IPAC'16, Busan, Korea*, pp. 3488–3491, 2016.

[20] S. Ogur, K. Oide, D. Shatilov, F. Zimmermann, and Y. Papaphilippou, "Bunch Schedules for the FCC-ee Pre-injector," in *Proceedings of IPAC'18, Vancouver, BC, Canada*, pp. 79–82, 2018.

[21] S. Ogur *et al.*, "Overall Injection Strategy for FCC-ee," in *Proceedings of eeFACT2018, Hong Kong, China*. to be published.

[22] O. Etisken, Y. Papaphilippou, and A. Ciftci, "Pre-Booster Ring Considerations for the FCC e^+e^- Injector," in *Proceedings of IPAC'18, Vancouver, BC, Canada*, pp. 83–86, 2018.

[23] B. Härer, B. Holzer, T. Tydecks, and Y. Papaphilippou, "Status of the FCC-ee Top-Up Booster Synchrotron," in *Proceedings of IPAC'18, Vancouver, BC, Canada*, pp. 250–252, 2018.

[24] D. Shatilov, "FCC-ee parameter optimization," *ICFA Beam Dyn. Newslett.*, vol. 72, pp. 30–41, 2017.

[25] L. Palumbo, V. Vaccaro, and M. Zobov, "Wake fields and impedance," Tech. Rep. LNF-94-041-P, CERN, Geneva, Switzerland, 1994.

[26] P. B. Wilson and J. E. Griffin, "High energy electron linacs; application to storage ring RF systems and linear colliders," in *AIP Conference Proceedings*, vol. 87, pp. 450–555, 1982.

[27] A. W. Chao, *Physics of collective beam instabilities in high energy accelerators*. Wiley, 1993.

[28] A. Hofmann, “Beam Instabilities,” in *CERN Accelerator School: 5th Advanced Accelerator Physics Course, Rhodes, Greece*, pp. 307–330, 1993.

[29] S. Heifets, “Broadband impedance of the B factory,” in *Proceedings of the 1993 Particle Accelerator Conference: Volume 5*, pp. 3459–3461, 1993.

[30] K. L. Bane, “The calculated longitudinal impedance of the SLC damping rings,” in *Proceedings of 1st EPAC Conference, Rome, Italy*, pp. 637–639, 1988.

[31] K. L. F. Bane, “Bunch lengthening in the SLC damping rings,” Tech. Rep. SLAC-PUB-5177, SLAC, Stanford, CA, 1990.

[32] W. Fischer, M. Blaskiewicz, J. Brennan, H. Huang, H.-C. Hseuh, V. Ptitsyn, T. Roser, P. Thieberger, D. Trbojevic, J. Wei, *et al.*, “Electron cloud observations and cures in the relativistic heavy ion collider,” *Physical Review Special Topics-Accelerators and Beams*, vol. 11, no. 4, p. 041002, 2008.

[33] H. Fukuma, “Electron cloud observations and predictions at KEKB, PEP-II and SuperB Factories,” in *Proceedings of ECLOUD’12, La Biodola, Isola d’Elba*, pp. 27–30, 2013.

[34] G. Rumolo, G. Iadarola, F. Zimmermann, E. Belli, P. Dijkstal, L. Mether, M. Schenk, H. Bartosik, K. Li, and A. Romano, “Electron Cloud Effects at the LHC and LHC Injectors,” in *Proceedings of IPAC’17, Copenhagen, Denmark*, pp. 30–36, 2017.

[35] M. Zobov, D. Alesini, A. Drago, A. Gallo, S. Guiducci, C. Milardi, A. Stella, S. De Santis, T. Demma, and P. Raimondi, “Operating experience with electron cloud clearing electrodes at DAΦNE,” *arXiv preprint arXiv:1306.5944*, 2013.

[36] G. Peach, “Ionization of atoms and positive ions by electron and proton impact,” *Journal of Physics B: Atomic and Molecular Physics*, vol. 4, no. 12, p. 1670, 1971.

[37] M. Sands, “The Physics of Electron Storage Rings: An Introduction,” *Conf. Proc.*, vol. C6906161, pp. 257–411, 1969.

[38] G. Iadarola, *Electron cloud studies for CERN particle accelerators and simulation code development*. PhD thesis, CERN-THESIS-2014-047, CERN, Geneva, Switzerland, 2014.

[39] R. Cimino, I. Collins, M. Furman, M. Pivi, F. Ruggiero, G. Rumolo, and F. Zimmermann, "Can low-energy electrons affect high-energy physics accelerators?," *Physical Review Letters*, vol. 93, no. 1, p. 014801, 2004.

[40] `https://github.com/PyCOMPLETE/PyECLOUD`.

[41] G. Rumolo and F. Zimmermann, "Practical user guide for ECLOUD," Tech. Rep. CERN-SL-Note-2002-016-AP, CERN, Geneva, Switzerland, 2002.

[42] G. Iadarola and G. Rumolo, "PyECLOUD and build-up simulations at CERN," *arXiv preprint arXiv:1309.6773*, 2013.

[43] E. Belli *et al.*, "Multigrid solver in PyPIC." Presentation at the Electron Cloud Meeting 32, 2 Sep. 2016. `https://indico.cern.ch/event/547910/`.

[44] J.-L. Vay, P. Colella, P. McCorquodale, B. Van Straalen, A. Friedman, and D. Grote, "Mesh refinement for particle-in-cell plasma simulations: Applications to and benefits for heavy ion fusion," *Laser and Particle Beams*, vol. 20, no. 4, pp. 569–575, 2002.

[45] A. Friedman, R. H. Cohen, D. P. Grote, S. M. Lund, W. M. Sharp, J.-L. Vay, I. Haber, and R. A. Kishek, "Computational methods in the warp code framework for kinetic simulations of particle beams and plasmas," *IEEE Transactions on Plasma Science*, vol. 42, no. 5, pp. 1321–1334, 2014.

[46] M. Bassetti and G. A. Erskine, "Closed expression for the electrical field of a two-dimensional Gaussian charge," Tech. Rep. CERN-ISR-TH-80-06. ISR-TH-80-06, CERN, Geneva, Switzerland, 1980.

[47] K. Oide, "Status of optics." Presentation at the FCC Week 2017, Berlin, Germany, 31 May 2017. `https://indico.cern.ch/event/556692/contributions/2590161/`.

[48] R. Kersevan, "FCC-ee beam vacuum concept: the beam pipe of FCC-ee." Presentation at the FCC Week 2018, Amsterdam, Netherlands, 10 Apr. 2018. `https://indico.cern.ch/event/656491/contributions/2947258/`.

[49] Y. Suetsugu, K.-i. Kanazawa, K. Shibata, T. Ishibashi, H. Hisamatsu, M. Shirai, and S. Terui, "Design and construction of the SuperKEKB vacuum system," *Journal of Vacuum Science & Technology A: Vacuum, Surfaces, and Films*, vol. 30, no. 3, p. 031602, 2012.

[50] I. Karpov, R. Calaga, and E. Chapochnikova, "HOM power in FCC-ee cavities," *Physical Review Accelerators and Beams*, vol. 21, p. 071001, 2018.

[51] V. Baglin, I. Collins, and O. Gröbner, "Photoelectron yield and photon reflectivity from candidate LHC vacuum chamber materials with implications to the vacuum chamber design," in *Proceedings of EPAC'98, Stockholm, Sweden*, p. 2169, 1998.

[52] V. Baglin, I. Collins, O. Gröbner, C. Grünhagel, B. Henrist, N. Hilleret, and B. Jenninger, "Measurements at EPA of vacuum and electron-cloud related effects," *Chamonix 2001, LEP performance*, vol. 5, pp. 10–10, 2001.

[53] N. Mahne, V. Baglin, I. Collins, A. Giglia, L. Pasquali, M. Pedio, S. Nannarone, and R. Cimino, "Photon reflectivity distributions from the LHC beam screen and their implications on the arc beam vacuum system," *Applied surface science*, vol. 235, no. 1-2, pp. 221–226, 2004.

[54] R. Cimino, V. Baglin, and I. Collins, "VUV synchrotron radiation studies of candidate LHC vacuum chamber materials," *Vacuum*, vol. 53, no. 1-2, pp. 273–276, 1999.

[55] H. Fukuma and L. Wang, "Simulation study of the electron cloud instability in SuperKEKB," in *Proceedings of the 2005 Particle Accelerator Conference*, pp. 868–870, 2005.

[56] G. Rumolo, F. Ruggiero, and F. Zimmermann, "Simulation of the electron-cloud build up and its consequences on heat load, beam

stability, and diagnostics," *Physical Review Special Topics-Accelerators and Beams*, vol. 4, no. 1, p. 012801, 2001.

[57] K. Ohmi, F. Zimmermann, and E. Perevedentsev, "Wake-field and fast head-tail instability caused by an electron cloud," *Physical Review E*, vol. 65, no. 1, p. 016502, 2001.

[58] K. Ohmi and D. Zhou, "Study of electron cloud effects in SuperKEKB," in *Proceedings of IPAC'14, Dresden, Germany*, pp. 1597–1599, 2014.

[59] V. K. Neil and A. M. Sessler, "Longitudinal resistive instabilities of intense coasting beams in particle accelerators," *Review of Scientific Instruments*, vol. 36, no. 4, pp. 429–436, 1965.

[60] L. J. Laslett, V. K. Neil, and A. M. Sessler, "Transverse resistive instabilities of intense coasting beams in particle accelerators," *Review of Scientific Instruments*, vol. 36, no. 4, pp. 436–448, 1965.

[61] N. Nakamura, "Effects of longitudinal and transverse resistive-wall wakefields on ERLs," in *Proceedings of ERL09, Ithaca, New York, USA*, p. 85, 2009.

[62] M. Migliorati and M. Zobov, "Impedance and instabilities in lepton colliders." Presentation at International Workshop on Impedances and Beam Instabilities in Particle Accelerators, Benevento, Italy, 22 Sep 2017. `https://agenda.infn.it/getFile.py/access?contribId=101&sessionId=15&resId=0&materialId=slides&confId=12603`.

[63] A. Chao, B. Chen, and K. Oide, "A weak microwave instability with potential well distortion and radial mode coupling," in *Proceedings of the 1995 Particle Accelerator Conference*, vol. 5, pp. 3040–3042, 1995.

[64] D. Boussard, "Observation of microwave longitudinal instabilities in the CPS," Tech. Rep. CERN-LabII-RF-INT-75-2, CERN, Geneva, Switzerland, Apr 1975.

[65] F. J. Sacherer, "Transverse bunched beam instabilities - theory," in *9th International Conference on High-energy Accelerators, SLAC, Stanford, CA, USA,*, vol. 5, pp. 347–351, 1974.

[66] F. Sacherer and B. Zotter, "Transverse instabilities of relativistic particle beams in accelerators and storage rings," Tech. Rep. CERN-77-13, CERN, Geneva, Switzerland, 1977.

[67] M. Zobov, A. Gallo, A. Ghigo, F. Marcellini, M. Migliorati, F. Sannibale, and M. Serio, "Transverse mode coupling instability in the DAΦNE Accumulator Ring," Tech. Rep. DAΦNE TECHNICAL NOTE No. G-50, INFN - LNF, Accelerator Division, Frascati, Italy, 1998.

[68] K. Yokoya, "Resistive wall impedance of beam pipes of general cross section," *Part. Accel.*, vol. 41, pp. 221–248. 30 p, Feb 1993.

[69] T. Günzel, "Transverse coupling impedance of the storage ring at the european synchrotron radiation facility," *Physical Review Special Topics-Accelerators and Beams*, vol. 9, no. 11, p. 114402, 2006.

[70] A. Chao, S. Heifets, and B. Zotter, "Tune shifts of bunch trains due to resistive vacuum chambers without circular symmetry," *Physical Review Special Topics-Accelerators and Beams*, vol. 5, no. 11, p. 111001, 2002.

[71] A. Blednykh, G. Bassi, Y. Hidaka, V. Smaluk, and G. Stupakov, "Low-frequency quadrupole impedance of undulators and wigglers," *Physical Review Accelerators and Beams*, vol. 19, no. 10, p. 104401, 2016.

[72] N. Wang and Q. Qin, "Resistive-wall impedance of two-layer tube," *Physical Review Special Topics-Accelerators and Beams*, vol. 10, no. 11, p. 111003, 2007.

[73] `https://github.com/amorimd/CloneIW2D`.

[74] N. Mounet, *The LHC transverse coupled-bunch instability*. PhD thesis, CERN-THESIS-2012-055, CERN, Geneva, Switzerland, 2012.

[75] L. Vos, "The Impedance of Multi-layer Vacuum Chambers," Tech. Rep. CERN-AB-2003-093-ABP, CERN, Geneva, Switzerland, 2003.

[76] E. Koukovini Platia, *High Frequency Effects of Impedances and Coatings in the CLIC Damping Rings*. PhD thesis, CERN-THESIS-2015-152 CERN, Geneva, Switzerland, 2015.

[77] `https://github.com/PyCOMPLETE/PyHEADTAIL`.

[78] K. Li, H. Bartosik, G. Iadarola, A. Oeftiger, A. Passarelli, A. Romano, G. Rumolo, M. Schenk, and S. Hegglin, "Code development for collective effects," in *Proceedings of HB2016, Malmö, Sweden*, pp. 362–367, 2016.

[79] M. Migliorati, S. Persichelli, H. Damerau, S. Gilardoni, S. Hancock, and L. Palumbo, "Beam-wall interaction in the CERN Proton Synchrotron for the LHC upgrade," *Physical Review Special Topics-Accelerators and Beams*, vol. 16, no. 3, p. 031001, 2013.

[80] M. Migliorati and L. Palumbo, "Multibunch and multiparticle simulation code with an alternative approach to wakefield effects," *Physical Review Special Topics-Accelerators and Beams*, vol. 18, no. 3, p. 031001, 2015.

[81] `https://blond.web.cern.ch/`.

[82] R. Boni, A. Drago, A. Gallo, A. Ghigo, F. Marcellini, M. Migliorati, F. Sannibale, M. Serio, A. Stella, G. Vignola, *et al.*, "DAΦNE accumulator ring coupling impedance measurements," *Nuclear Instruments and Methods in Physics Research Section A: Accelerators, Spectrometers, Detectors and Associated Equipment*, vol. 418, no. 2-3, pp. 241–248, 1998.

[83] D. Quartullo, M. Migliorati, J. Repond, *et al.*, "Comparison of different methods to calculate induced voltage in longitudinal beam dynamics codes," in *Proceedings of IPAC'17, Copenhagen, Denmark*, pp. 4465–4468, 2017.

[84] H. Timko, D. Quartullo, A. Lasheen, and J. Esteban Müller, "Benchmarking the beam longitudinal dynamics code BLonD," in *Proceedings of IPAC'16, Busan, Korea*, pp. 3094–3097, 2016.

[85] H. Bartosik, *Beam dynamics and optics studies for the LHC injectors upgrade*. PhD thesis, CERN-THESIS-2013-257, CERN, Geneva, Switzerland, 2013.

[86] P. C. Pinto, S. Calatroni, P. Chiggiato, H. Neupert, W. Vollenberg, E. Shaposhnikova, M. Taborelli, and C. Y. Vallgren, "Thin film coatings

for suppressing electron multipacting in particle accelerators," in *Proceedings of 2011 Particle Accelerator Conference, New York, NY, USA*, 2011.

[87] P. C. Pinto, "History and potential of Non Evaporable Getter (NEG) technology." Presentation at Workshop on Advanced Materials and Surfaces, CERN, Geneva, Switzerland, 19 Nov 2013. `https://indico.cern.ch/event/229108/contributions/1539894/`.

[88] P. C. Pinto, "FCC-ee beam vacuum concept: the beam pipe of FCC-ee." Presentation at the FCC Week 2018 , Amsterdam, Netherlands, 10 Apr 2018. `https://indico.cern.ch/event/656491/contributions/2947258/`.

[89] R. Kersevan, "private communication."

[90] E. Belli, M. Migliorati, S. Persichelli, and M. Zobov, "Single beam collective effects in FCC-ee due to beam coupling impedance," *arXiv preprint arXiv:1609.03495*, 2016.

[91] N. Biancacci and M. Migliorati, "Wakefield approximations." Presentation at the Impedance meeting, CERN, Geneva, Switzerland, 23 Feb 2018. `https://indico.cern.ch/event/438866/contributions/1085121/`.

[92] J. Haissinski, "Exact longitudinal equilibrium distribution of stored electrons in the presence of self-fields," *Il Nuovo Cimento B (1971-1996)*, vol. 18, no. 1, pp. 72–82, 1973.

[93] K. Ohmi, N. Kuroo, K. Oide, D. Zhou, and F. Zimmermann, "Coherent beam-beam instability in collisions with a large crossing angle," *Physical review letters*, vol. 119, no. 13, p. 134801, 2017.

[94] `https://twiki.cern.ch/twiki/bin/view/ABPComputing/DELPHI`.

[95] S. White, X. Buffat, N. Mounet, and T. Pieloni, "Transverse mode coupling instability of colliding beams," *Physical Review Special Topics-Accelerators and Beams*, vol. 17, no. 4, p. 041002, 2014.

[96] K.-Y. Ng, *Physics of intensity dependent beam instabilities*. World Scientific, 2006.

[97] A. Drago, M. Serio, D. Teytelman, C. Milardi, C. Biscari, J. Fox, A. Gallo, A. Ghigo, M. Zobov, A. Stella, *et al.*, "High Current Multibunch Operation at DAΦNE," in *Proceedings of Particle Accelerator Conference, Chicago, IL*, pp. 3543–3545, 2001.

[98] A. Drago, "Feedback Systems for FCC-ee," *arXiv preprint arXiv:1704.06162*, 2017.

[99] C. Benvenuti, "Molecular surface pumping: the getter pumps," Tech. Rep. CERN-OPEN-2000-265, CERN, Geneva, Switzerland, 1999.

[100] P. Chiggiato and P. C. Pinto, "Ti–Zr–V non-evaporable getter films: From development to large scale production for the Large Hadron Collider," *Thin Solid Films*, vol. 515, no. 2, pp. 382–388, 2006.

[101] `http://en-dep.web.cern.ch/en-dep/Groups/MME/MM/SEM.htm`.

[102] C. Wagner, W. Riggs, L. Davis, J. Moulder, and G. Muilenberg, *Handbook of X-ray Photoelectron Spectroscopy*. Perkin-Elmer Corporation, Physical Electronics Division, 1992.

[103] T. Sinkovits, "Is NEG coating structure relevant for gas pumping?." Presentation at TE-VSC Seminar, CERN, Geneva, Switzerland, 27 Jun 2017. `https://indico.cern.ch/event/628547/contributions/2538607/`.

[104] H. Bruining, *Physics and Applications of Secondary Electron Emission*. Pergamon Press, London, 1954.

[105] C. Scheuerlein, *The influence of an air exposure on the secondary electron yield of copper*. PhD thesis, CERN-THESIS-2002-022, CERN, Geneva, Switzerland, 2002.

[106] R. Calaga, A. Butterworth, O. Brunner, and E. Jensen, "SRF for future circular colliders," in *Proceedings of SRF2015, Whistler, BC, Canada*, pp. 1474–1480, 2015.

[107] A. Butterworth, "Cavity design and beam-cavity interaction challenges." Presentation at the FCC Week 2017, Berlin, Germany, 30 May 2017. `https://indico.cern.ch/event/556692/contributions/2484361/`.

[108] S. G. Zadeh, "Cavity design approaches and HOM damping for FCC-ee." Presentation at the FCC Week 2017, Berlin, Germany, 30 May 2017. `https://indico.cern.ch/event/556692/contributions/2484333/`.

[109] `http://abci.kek.jp/`.

[110] S. Heifets and S. Kheifets, "Coupling impedance in modern accelerators," *Reviews of Modern Physics*, vol. 63, no. 3, p. 631, 1991.

[111] R. Kersevan, "FCC-ee Vacuum Effects and Simulations." Presentation at the FCC Week 2016, Rome, Italy, 14 Apr 2016. `https://indico.cern.ch/event/438866/contributions/1085121/`.

[112] `https://www.cst.com`.

[113] S. DeBarger, M. Sullivan, C. Ng, U. Wienands, T. Porter, S. Metcalfe, and J. Seeman, "The PEP-II movable collimators," Tech. Rep. SLAC-PUB-11752, SLAC, Stanford, CA, 2001.

[114] T. Ishibashi *et al.*, "Low impedance movable collimators for SuperKEKB," in *Proceedings of IPAC'17, Copenhagen, Denmark*, pp. 14–19, 2017.

[115] F. Marcellini, M. Serio, A. Stella, and M. Zobov, "DAPHNE broadband button electrodes," *Nucl. Instrum. Meth.*, vol. A402, pp. 27–35, 1998.

[116] A. Rodrigues *et al.*, "Sirius Status Report," in *Proceedings of IPAC'16, Busan, Korea*, pp. 2811–2814, 2016.

[117] E. Belli, M. Migliorati, B. Spataro, S. Persichelli, A. Novokhatski, G. Castorina, and M. Zobov, "Coupling impedances and collective effects for FCC-ee," in *Proceedings of IPAC'17, Copenhagen, Denmark*, pp. 3734–3737, 2017.

[118] Y. Suetsugu, M. Shirai, and K. Shibata, "Possibility of comb-type rf shield structure for high-current accelerators," *Physical Review Special Topics-Accelerators and Beams*, vol. 6, no. 10, p. 103201, 2003.

[119] M. Sullivan, "MDI: synchrotron radiation protection." Presentation at the FCC Week 2017, Berlin, Germany, 31 May 2017. `https://indico.cern.ch/event/556692/contributions/2590394/`.

[120] A. W. Chao, K. H. Mess, M. Tigner, and F. Zimmermann, *Handbook of accelerator physics and engineering*. World Scientific, 1999.

[121] A. Novokhatski, J. Seeman, and M. Sullivan, "Analysis of the wake field effects in the PEP-II storage rings with extremely high currents," *Nuclear Instruments and Methods in Physics Research Section A: Accelerators, Spectrometers, Detectors and Associated Equipment*, vol. 735, pp. 349–365, 2014.

[122] A. Novokhatski, J. Seeman, M. Sullivan, and U. Wienands, "Electromagnetic wave excitation, propagation, and absorption in high current storage rings," *IEEE Transactions on Nuclear Science*, vol. 63, pp. 812–817, April 2016.

[123] A. Novokhatski, "The Computer Code NOVO for the Calculation of Wake Potentials of the Very Short Ultra-relativistic Bunches," Tech. Rep. SLAC-PUB-11556, SLAC, Stanford, CA, 2005.

[124] `http://www.catia.com.pl/`.

[125] M. Migliorati, E. Belli, and M. Zobov, "Impact of the resistive wall impedance on beam dynamics in the future circular e^+e^- collider," *Phys. Rev. Accel. Beams*, vol. 21, p. 041001, Apr 2018.

[126] A. Novokhatski, M. Sullivan, E. Belli, M. Gil Costa, and R. Kersevan, "Unavoidable trapped mode in the interaction region of colliding beams," *Phys. Rev. Accel. Beams*, vol. 20, no. 11, p. 111005. 10 p, 2017.

[127] E. Belli *et al.*, "Electron cloud buildup and impedance effects on beam dynamics in the Future Circular e^+e^- Collider and experimental characterization of thin TiZrV vacuum chamber coatings," *Phys. Rev. Accel. Beams*, vol. 21, p. 111002. 10 p, 2018.

[128] G. Rumolo, K. S. B. Li, L. M. Mether, E. Belli, G. Iadarola, M. Schenk, H. Bartosik, and A. Romano, "Electron cloud in the CERN accelerator complex," in *Proceedings of HB2016, Malmö, Sweden*, pp. 266–271, 2016.

[129] E. Belli, P. Costa Pinto, M. Migliorati, G. Rumolo, T. Sinkovits, and M. Taborelli, "Electron Cloud Studies in FCC-ee," in *Proceedings of IPAC'18, Vancouver, BC Canada*, pp. 374–377, 2018.

[130] E. Belli, G. Castorina, M. Migliorati, G. Rumolo, B. Spataro, and M. Zobov, "Single Bunch Instabilities in FCC-ee," in *Proceedings of IPAC'18, Vancouver, BC Canada*, pp. 3336–3339, 2018.

[131] E. Belli, G. Castorina, M. Migliorati, S. Persichelli, G. Rumolo, B. Spataro, and M. Zobov, "Some Critical Collective Effects for the FCC-ee Collider," *ICFA Beam Dyn. Newslett.*, vol. 72, pp. 61–69, 2017.

[132] E. Belli, M. Migliorati, and G. Rumolo, "Electron Cloud and Collective Effects in the Interaction Region of FCC-ee," in *Proceedings of eeFACT2016, Daresbury, United Kingdom*, pp. 130–135, 2016.

[133] M. Migliorati, E. Belli, G. Castorina, S. Persichelli, B. Spataro, and M. Zobov, "Collective effects issues for FCC-ee," in *Proceedings of eeFACT2016, Daresbury, United Kingdom*, pp. 100–107, 2016.

[134] G. Iadarola, E. Belli, K. Li, L. Mether, A. Romano, and G. Rumolo, "Evolution of Python Tools for the Simulation of Electron Cloud Effects," in *Proceedings of IPAC'17, Copenhagen, Denmark*, pp. 3803–3806, 2017.

[135] M. Zobov, E. Belli, G. Castorina, M. Migliorati, S. Persichelli, G. Rumolo, and B. Spataro, "Study of Collective Effects in the FCC-ee Collider," *arXiv preprint arXiv:1805.08466*, 2018.

ACKNOWLEDGMENTS

My first deepest thanks goes to my university supervisor Mauro Migliorati, not only for giving me the opportunity to join the FCC project and to start this research activity, but also for placing his trust and confidence in my abilities. During the last three years, I traveled a lot and partecipated to many conferences where I met people from all around the world, continuously testing and improving myself. It was really a wonderful and constructive experience, personally and professionally. I would also like to thank my CERN supervisor Giovanni Rumolo for giving me the opportunity to work at CERN, my section leader Elias Metral for the possibility to join the HSC section and all the "electron cloud" team for the help and the advices.
A special thanks goes to Frank Zimmermann, Oide Katsunobu and the FCC-ee team for all the valuable discussions and for sharing their knowdledge and time. Thanks to Mauro Taborelli, Pedro Costa Pinto, Theo Sinkovits, Holger Neupert and Valentine Petit for their important support to all the experimental studies presented in this thesis.
Thanks to all my friends, near by and far away.
And the last and most important thanks to my family and Daniele, for their endless love and continuous support.